Evaporative cooling and Bose-Einstein Condensation of Rb-87 in a moving-coil TOP trap geometry

A Thesis Presented

by

Daniel Guenther Greif

to

The Graduate School

in Partial Fulfillment of the

Requirements

for the Degree of

Master of Arts

in

Physics

Stony Brook University

December 2007

Stony Brook University

The Graduate School

Daniel Guenther Greif

We, the thesis committee for the above candidate for the Master of Arts degree, hereby recommend acceptance of the thesis.

Dominik Schneble, Thesis Advisor
Assistant Professor, Department of Physics and Astronomy
Stony Brook University

Harold Metcalf
Distinguished Teaching Professor, Department of Physics and Astronomy
Stony Brook University

Thomas Bergeman
Adjunct Professor, Department of Physics and Astronomy
Stony Brook University

This thesis is accepted by the Graduate School.

Lawrence Martin
Dean of the Graduate School

Abstract of the Thesis

Evaporative cooling and Bose-Einstein Condensation of Rb-87 in a moving-coil TOP trap geometry

by

Daniel Guenther Greif

Master of Arts

in

Physics

Stony Brook University

2007

This thesis discusses evaporative cooling and Bose-Einstein Condensation of Rb-87 in the $|1,-1\rangle$ ground state. Quadrupole coils mounted on a mechanical transporter are used to move the laser-cooled atoms on a 2-dim. path into a glass cell to perform RF evaporative cooling in a TOP trap. This trap is formed by the moving coil quadrupole field in conjunction with a rotating bias field. Evaporative cooling simulations are carried out to provide a guideline for the optimization in the experiment.
Typical condensate sizes are $\sim 1 \times 10^6$ atoms with a critical temperature of 150nK. Our data agrees well with the theoretical predictions of the phase transition and anisotropic expansion. The condensate atom number is found to be very stable, while the position stability is very promising for condensation in a dipole trap and future experiments in optical lattices.

To my family and friends

Contents

List of Figures

List of Tables

Acknowledgements

It is now only one week to my return back home to Germany. The last year has been very interesting and exciting in many ways. I had the luck to join the group at a time, when Bose-Einstein Condensation was close. Making a condensate for the first time is definitely one of the coolest experiences in my life. Coming from a theoretical background, doing experimental physics was a completely new experience for me. I would like to express my gratitude first to Dominik Schneble, who gave me the fortunate opportunity to work in his lab one year ago and made this experience unforgettable. He is a very patient person, who spends as much time as possible in the lab to help the students. Dominik is a relaxed person and manages to turn frustration in the lab into curiosity and excitement, which makes him a great person to work with. I would like to express my gratitude for proof-reading of my thesis and all the useful corrections.

I would also like to thank the whole group: Rebekah Schiller was always a source of good mood and brightness in the often very dark lab room, showed me how to align optics and brought distraction by solving crosswords with me - although I could only rarely make a contribution. Daniel Pertot spent a lot of time helping me to set up the RF electronics. Without him I woulds still have no clue what the RF box is doing. I had a great time spending numerous nights in the lab with him, although we could never really agree on a good radio station. His calm and gentle personality make Daniel a great person to work with and his sodering skills are unchallenged. My thanks also go to Stephan Albert, with whom I had a great road trip to Canada and who got me interested in ultracold atomic physics. He showed and explained me the basics of our apparatus. Azure Hansen helped to set up the RF shield and constantly offered her helping hand to everybody in the lab. Yancey Sechrest helped performing the TOP trap frequency measurement and is a very relaxed and easy-going person - and a very good soccer player. I wish them both good luck for their graduate studies.

Dominik Schneble, Thomas Bergeman and Harold Metcalf, who were in my committee, gave me very constructive feedback on my thesis. My gratitude

also goes to the people in the administration, in particular Pat Peiliker, Sarah Lutterbie and Maria Hofer, who are always very friendly and caring about the many administrative problems graduate students have. I would also like to thank Laszlo Mihaly and Peter Koch (Stony Brook) and Fakher Assaad (Würzburg) for giving me the opportunity to participate at the exchange program and to join the physics graduate school in Stony Brook.
My time in Stony Brook would not have been the same if I had not met so many wonderful people, with whom I had a great time and will miss a lot. Thank you for the many rides, invitation to parties and wonderful discussions. I am grateful to Claire, who gave me a place to stay in the last few months and Jennifer, who I am very happy to have met and has become a special person for me. I would also like to thank my friends in Germany, who kept in touch with me over the last year and always showed me their support. At this point I would like to mention Daniel, Florian, Jürgen, Barbara and Anne-Katharina. I wish them the best for their future and hope to spend many more years together with them. Cooking a turkey last Christmas together with Thai, Volker, Alexander and Elena will always be a great memory. I also wish Sebastian the very best with his family and Carsten good luck for his graduation in Würzburg.
Special thanks go to my father Jakob, my mother Anna and my brother Thomas, who constantly support me and believe in me. They are a wonderful source of encouragement and I am very grateful and happy to have such a family. This thesis is dedicated to you.
This work was supported by the German government and the Research Foundation of the State University of New York.

Chapter 1

Introduction

The history of Bose-Einstein Condensation (BEC) reaches back to the year 1924, when the Indian physicist S.N. Bose wrote an article [1] deriving Planck's black body radiation spectrum from the indistinguishability of particles, a fundamental concept of quantum mechanics. A. Einstein, who translated the article and published it, applied this idea to an ideal gas of non-interacting bosonic particles [2–4] and predicted that the system undergoes a phase transition at temperatures below a critical temperature into a state, in which a macroscopic number of atoms is in the ground state. This macroscopic occupation of the lowest energy state is referred to as Bose-Einstein Condensation.

It is remarkable that this phase-transition does not rely on interaction effects of particles, as is the case for transitions into solid, liquid or gaseous forms for instance. It is purely a result of quantum statistics and the fundamental difference between fermions (half-integer spin) and bosons (integer spin): while it is forbidden for fermions to occupy the same ground state (Pauli-principle) owing to the anti-symmetry of the wave function, bosons can occupy the same ground state and are characterized by symmetric wave functions. In an ensemble of many particles of the same species, this leads to two occupation statistics - the Bose-Einstein distribution for bosons and the Fermi-Dirac distribution for fermions. Bose-Einstein condensation is a direct consequence of the bosonic distribution statistics.

Considering the wave nature of particles, a more intuitive interpretation of condensation is possible: a gas of atoms can be considered classical, if the average spacing between the particles is much larger than the thermal de Broglie wavelength $\lambda_{dB} \propto 1/\sqrt{T}$. However, at very low temperatures ($\sim$ 100nK for dilute atomic gases at densities of $\sim 10^{14}\text{cm}^{-3}$), this wavelength exceeds the inter-particle spacing, resulting in an overlap of the wave functions, and the many-particle state can be described by a single macroscopic wave function.

This model gives a condition on the phase-space density $n\lambda_{dB}^3$ (particles per unit volume of phase space), where n is the average particle density:

$$n\lambda_{dB}^3 \sim 1 \tag{1.1}$$

Pushing a system to the quantum regime in the experiment is thus possible for high densities or for very low temperatures. This posed a big challenge to the physics community for a long time. The main reason was that cryogenic cooling limited the temperatures to $\sim$ 1mK, so that the densities had to be increased, which comes at the cost of increased interactions (e.g. van der Waals interaction). After the discovery of the strongly interacting superfluid He-4 in 1937, F. London proposed that this could be interpreted as a Bose-Einstein Condensate [5]. It was also found that the phenomenon of superconductivity, which was discovered in 1957, was also a realization of Bose-Einstein Condensation - in this case of coupled electron pairs, called Cooper pairs (BCS theory).
However, physicists still sought to achieve BEC in weakly interacting systems (in which the scattering length is much smaller than the inter-particle distances) to bring the ultimate proof that condensation is only a result of quantum statistics. Promising candidates were dilute atomic gases in a metastable state: the idea is to bring a gas of weakly interacting bosonic atoms to densities where the gaseous state becomes metastable (three-body collisions) with lifetimes long enough for experiments ($\sim$ 1s). This limits the densities to typically 10^{14}cm^{-3}, which makes ultra-low temperatures of 100 nK necessary - more than 3 orders of magnitude colder than the temperatures achievable with cryostats.

The situation changed suddenly with the invention of laser cooling in the 1980s [6], which earned S. Chu, C. Cohen-Tannoudji and W.D. Phillips the Nobel-Prize in 1997. This made efficient trapping and cooling of $\sim 10^{10}$ atoms at $10-100\mu$K possible. In most cases the atoms have very simple level-structures, such as alkali atoms for example. One very prominent implementation of laser cooling and trapping is the magneto-optical trap (MOT), which can capture and cool a cloud of atoms at the same time using optical forces. The setup basically consists of a magnetic field created by two anti-Helmholtz coils and six counter-propagating laser beams resonant with a closed atomic transition. In spite of this huge leap in phase-space density from 10^{-18} (thermal gas at room temperature) to 10^{-6} (MOT), the phase space density was still not high enough for condensation due to photon reabsorption. The final breakthrough came with the idea of evaporative cooling of the "hot" atoms in a magnetic trap, first proposed by Hess [7]: by removing the "hottest" atoms from the

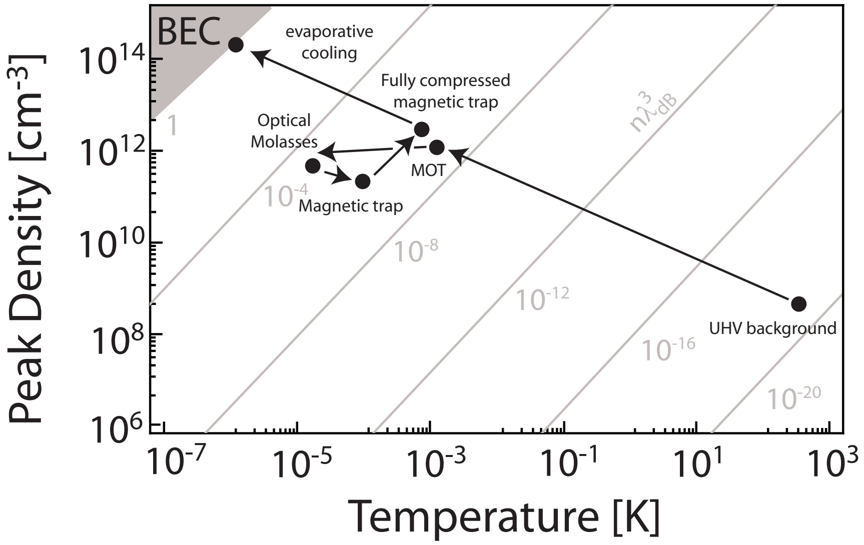

Figure 1.1: Roadmap to Bose-Einstein Condensation in our experiment. The gray lines are region of particle density n and tempereraturе T with constant phase-space density $n\lambda^3_{dB}$. Starting from a Rb background pressure in an UHV at room temperature, the atom cloud undergoes a tremendous increase of 18 orders of magnitude in phase-space density. The major job is done by laser cooling (MOT and Optical Molasses), while the magnetic trap and subsequent compression are necessary to form a conservative trapping potential for evaporative cooling. In our setup, condensation occurs at a critical temperature of 150nK leading to almost pure condensates of typically 1.0×10^6 atoms at densities of $1...2 \times 10^{14}\mathrm{cm}^{-3}$

cloud, the average energy per atom is decreased and hence the ensemble temperature lowered. An overview of the different sequence steps and the scaling of the relevant parameters for our setup is given in Fig. 1.1.
The first Bose-Einstein Condensates were realized independently by three groups in 1995 for the elements Rb-87, Li-7 and Na-23 [8–11], which earned E. A. Cornell, W. Ketterle and C. E. Wieman the Nobel-Prize in 2001. Today, BEC has been achieved with many more elements: H, Rb-85, K-41, metastable He-4, Cs-113, Yb-174 and Cr-52 [12–19].

The successful demonstration of Bose-Einstein Condensation in dilute atomic gases in 1995 had a huge impact on the physics community.
Today, approximately 70 groups world-wide are currently doing research with ultracold atomic gases. Among the many interesting experiments with degenerate bosonic gases are for example the study of excitations and propagation

of sound [20, 21], observation of interference between two condensates [22], realization of an atom laser [23, 24], four-wave mixing and Bragg spectroscopy of condensates [25, 26], superfluidity and vortices [27, 28] or the quantum phase transition from a superfluid to a Mott Insulator [29]. One of the many fascinating experiments with ultracold fermionic quantum gases are molecular condensation of atom pairs [30–32], the study of the BEC-BCS crossover [33, 34] or Fermi gases with unequal spin populations [35, 36]. Thus, applications are not only restricted to atomic physics - ultracold atomic physics has become an interdisciplinary field ranging from many body theory (quantum simulators), precision measurements, ultracold collision physics, solid-state physics, condensed matter model systems or even fundamental studies of quantum information/computation.

This thesis is divided into three main parts: the first chapter introduces our Rb-87 BEC apparatus with a focus on the RF evaporation setup and the TOP trap formed by the quadrupole coils of the mechanical transporter and a rotating bias field. The second chapter explains RF evaporative cooling in the dressed state picture and discusses a model for evaporative cooling simulations. This model provided a guideline for the experimental optimization protocol for condensation, which is also explained in this section. The last chapter shows the data of our first BEC. In addition, the condensate is characterized by comparing the data to the predictions of the phase transition and anisotropic expansion. Finally, the reproducibility in atom number and position of the condensate in the magnetic TOP trap is determined to estimate the prospects for condensation in an optical dipole trap and optical lattice experiments.

Chapter 2

Experimental setup

General features of our BEC machine for dilute atomic gases are an ultra-high vacuum with a bosonic atomic species, laser light for laser cooling and magnetic fields for trapping. Magnetic fields can also be used to transport atoms, which is useful if the vacuum is divided into two pressure regions to provide large MOT atom numbers and good lifetimes for evaporative cooling. Since many system parameters, such as laser detuning and power, shutters, magnetic fields or RF frequencies, have to be precisely controlled in time to achieve a BEC, a sequence generator on the computer is necessary, which controls several analog and digital output channels connected to the elements in the experiment via an A/D card. Atom number and temperature of the atom cloud are obtained by imaging the cloud onto a CCD chip. Fluorescence and absorption imaging are destructive techniques, while phase-contrast imaging is non-destructive.

In this chapter the experimental setup of our Rb-87 BEC apparatus is discussed. The first and second section explain the laser and vacuum system. The magnetic TOP trap, which is formed by the quadrupole coils of the transporter in conjunction with a rotating bias field, is discussed in the third section. Details of the RF coils for evaporative cooling in the TOP trap are explained in the fourth section, whereas the last part deals with the imaging setup and extraction of cloud parameters.

2.1 Optical setup

2.1.1 Rb-87 level scheme

The basic idea of laser cooling and trapping is to use the atom-light interaction between a cloud of atoms and a laser to create a conservative and/or cooling force on the atoms. The fundamental physical process is absorption and either spontaneous or stimulated emission of photons. Therefore, a laser beam near the resonance of an optical transition of an atomic level structure is required. A dissipative force can be created by many cycles of directional absorption from one or more laser beams and subsequent spontaneous emission in random directions. The transition therefore has to be closed, i.e. loss processes into other energy levels must not occur. All laser cooling schemes have this very important requirement of a "closed cycling transition" in common.

Since Rb-87 is an alkali atom, the level scheme is very simple due to the single valence electron. The ground state $5^2S_{1/2}$ splits into two hyperfine states F=1 and F=2, because the nuclear spin of Rb-87 is 3/2. Fine splitting of the excited state leads to the two possible states $5^2P_{1/2}$ (D_1-line) and $5^2P_{3/2}$ (D_2-line). $5^2P_{3/2}$, which is relevant for our experiments, splits into the F=0, F=1, F=2 and F=3 hyperfine states. An overview of the level scheme is given in Fig. 2.1. Details of Rb-87 properties can be found in [37].

The transition $5^2S_{1/2}, F = 2 \rightarrow 5^2P_{3/2}, F' = 3$ is a good candidate for the cycling transition, because $F' = F + 1$ as required by the MOT and spontaneous decay is only possible into the F=2 ground state. Unfortunately, this transition is not entirely closed, as atoms can also be excited into the $5^2P_{3/2}, F' = 2$ state, which happens roughly every ten-thousand cycles. Under this condition, the atom can decay into the F=1 ground state ($\Delta F = 0, 1, -1$). A second laser is therefore necessary, which is resonant with the $5^2S_{1/2}, F = 1 \rightarrow 5^2P_{3/2}, F' = 2$ transition to pump the atom back into the $5^2P_{3/2}, F' = 2$ state, where it can decay spontaneously into the F=2 ground state again. For imaging an F=1 or F=2 ground state atom cloud, either the cycling or repump beam can be used. Since closed transitions are also desirable for imaging, an additional depump beam resonant to the $5^2S_{1/2}, F = 2 \rightarrow 5^2P_{3/2}, F' = 2$ transition can be used for repump imaging to depump the F=2 ground state atoms into F=1 ground state atoms.

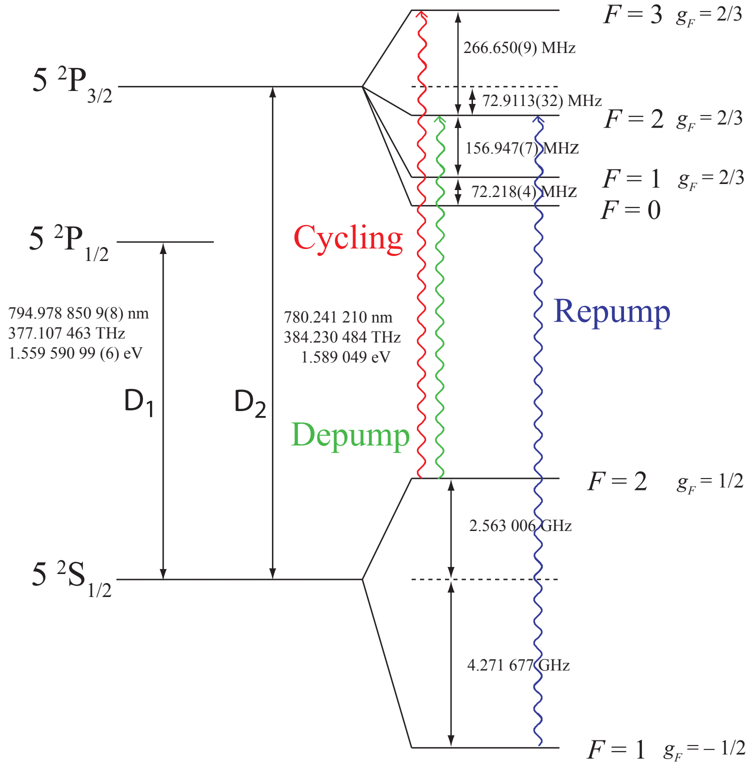

Figure 2.1: Fine- and hyperfine splitting of the ground and first excited state of Rb-87. The marked transitions of the D_2-line are used for laser cooling and imaging of the atom cloud. The magnetic sub states are not shown here.

2.1.2 Laser system

For the cycling transition an external cavity diode laser is used with a tapered amplifier chip (Sacher Tiger TEC 300-780, 1000mW). Since the hyperfine levels of the Rb-87 ground state are several GHz apart, an additional laser system is necessary for the repump transition. A second external cavity diode laser is used for this (Toptica DL100, 120mW). In both cases the external cavity is formed by a grating mounted on a piezo in Littrow configuration and the surface of the laser diode. The parameters temperature (slow timescales), diode current and piezo voltage (faster timescales) control the wavelength.
A small fraction of the laser output is used to perform spectroscopy on a Rb cell. The method in our setup is Doppler-free polarization saturation spectroscopy [38], where the real part of the refractive index at the resonance of the transition is measured and converted into a voltage by photo diodes. The voltage signal is then compared to a set voltage to extract an error signal,

which is used to stabilize the laser frequency with a PID controller through the piezo voltage (active feedback loop). This way, the cycling laser is stable within ~ 10MHz (limited by 60Hz noise from the lock box), while the frequency stability of the repump laser is approximately 1MHz. In both cases the noise is in the 1-100kHz range (the line width of the Rb-87 D_2 line is about $2\pi \times 6$MHz). A schematic view of the laser setup is given in Fig. 2.2.

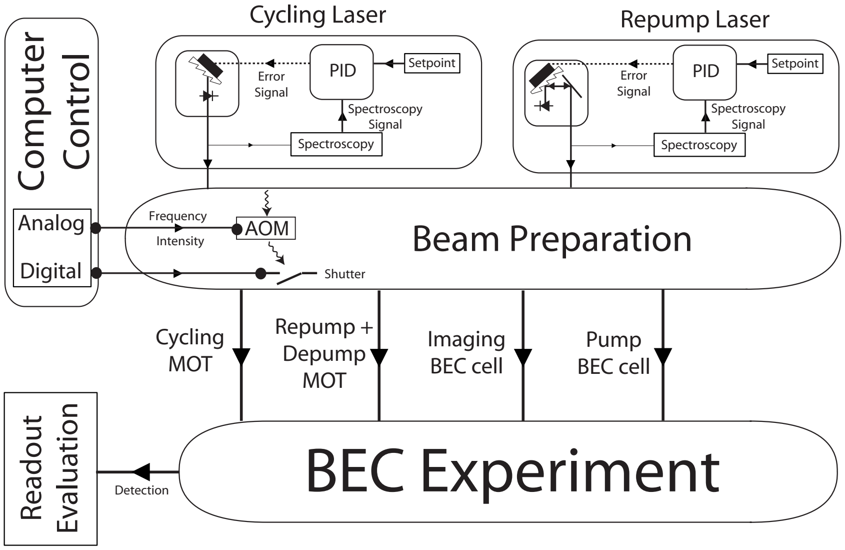

Figure 2.2: Scheme of optical setup. Both diode lasers are stabilized by an active feedback loop controlling the grating mounted on the piezo. The beam preparation section produces four main beams for the experiment, which are controllable in frequency and intensity from the computer via analog and digital channels.

The necessary laser wavelengths for the experiment are obtained by controlling frequency and intensity of the two laser systems with acousto-optical modulators (AOM). A double-pass AOM setup is used to avoid beam shifts when changing the laser frequency. The cycling laser beam is split into three parts: MOT, imaging and depump beam. The MOT light is detuned by typically $\sim 3.5\Gamma$ (controlled by an AOM), while both the imaging ($F = 2 \rightarrow F' = 3$) and depump beam ($F = 2 \rightarrow F' = 2$) are on resonance. The repump laser system has one output beam, which is also frequency-controlled by an AOM.

The entire laser setup is covered in boxes with shutters for the lasers to prevent stray light from hitting the experiment. In essence, four main beam lines run to the experiment:

- MOT beam: detuned cycling laser beam (250mW behind fiber)
- MOT cell pump: resonant repump (50mW) and depump (6mW) laser beam
- BEC cell imaging beam: resonant cycling or repump laser beam (250μW behind fiber)
- BEC cell pump: resonant repump (50mW with flip mirror) and depump (3mW) laser beam

To decouple the optics for the experiment from the laser system, single-mode fibers are used (not the case for the pump beams). This way, beam drifts are minimized and the beam profiles can be improved, which is important for efficient laser cooling. The six MOT beams each carry about 40mW with beam diameters of about 4-5cm, so that the total intensity of all beams is well above the saturation intensity $I_s \sim 4\text{mW/cm}^2$ of the cycling transition. A sketch of the light production setup is shown in Fig. 2.3.

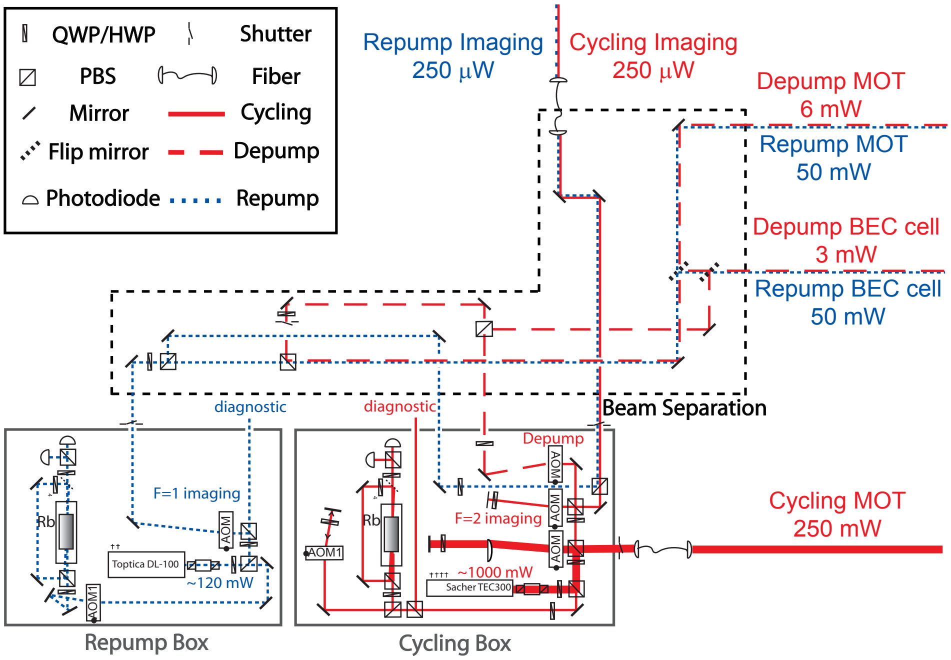

Figure 2.3: Setup of optical system (not to scale). Both diode lasers are frequency stabilized using polarization saturation spectroscopy with a feedback loop to the external grating. The light from both lasers is modified with AOMs. Four main beam lines run to the experiment.

2.2 Vacuum apparatus and quadrupole trap

The vacuum system is split into two different parts: the MOT chamber, where the atom cloud is laser cooled, and the BEC cell, to which the pre-cooled atom cloud is transported for evaporative cooling and condensation. This separation allows for long lifetimes in the BEC cell (~ 130s) and high MOT loading rates R $\propto \rho_{Rb}$ (vapor cell MOT) at the same time. Ultra-high vacua are necessary to reduce the background pressure of other elements, which knock out atoms from the MOT and reduce its steady-state atom number.
The MOT chamber is connected to a Rb oven, which can be opened manually and controlled in temperature. An ion pump provides the necessary UHV with partial-pressures of 10^{-8}-10^{-9} torr for Rb and $\sim\ 10^{-10}$ torr of other elements. The MOT chamber is made of Pyrex glass and has a cylindrical shape with an outer diameter of 5.7cm oriented in x-direction (lab coordinates). The six MOT beams (cycling MOT laser) are along the vertical z-axis and in the x-y plane, but rotated by 45° towards the two axes. This allows optical access from all directions, while the curved surface prevents etaloning of the MOT beams. The helicity of all MOT beams is left-handed (in separate reference frames), which is not significantly distorted by the curved surface of the MOT cell, since the chamber diameter is much larger than the MOT size. The repump/depump beam enters along the y-axis.
The BEC cell is a cuboid made of quartz with a width of 1.0 cm and a height of 2.0 cm (excluding the wall thickness of 1 mm). It is connected via a round glass tube to the "square chamber", which is part of the higher vacuum region. An ion pump (75 l/s) and a titanium sublimation pump provides pressures in the 10^{-12} torr range for long trap lifetimes. The two vacuum parts are connected by a thin tube of 1.0 cm diameter (differential pumping tube), which is large enough that the atom cloud just fits through. A valve offers the possibility to fully separate the two vacua from each other.

The magnetic trap is formed by a pair of coils in anti-Helmholtz configuration with the symmetry axis in the vertical z-direction. In the center of this geometry the magnetic field shows a linear behavior. Due to Maxwell's equation $\vec{\nabla} \cdot \vec{B}_{QP} = 0$, the axial field gradient b is twice the radial gradient.

$$\vec{B}_{QP}(x, y, z) = \frac{b}{2} \begin{pmatrix} -x \\ -y \\ 2z \end{pmatrix} \tag{2.1}$$

The potential for the atoms is induced by the coupling between the atomic magnetic moment and magnetic bias field, which results in a contribution to the interaction Hamiltonian $\mathcal{H}_I = \hat{\vec{\mu}} \cdot \vec{B}_{QP}$. For low enough magnetic fields ($<<$ 1 T), the total atomic angular momentum $\vec{F}$ including hyperfine splitting is still a good quantum number. Assuming the atomic spin can follow the magnetic axis adiabatically[1], the trap is linear in all directions (g_F is the g-factor of $\vec{F}$):

$$V(x, y, z) = g_F m_F \mu_B \frac{b}{2} \sqrt{x^2 + y^2 + 4z^2} \tag{2.2}$$

The coils are made of hollow copper tubes for water cooling and are connected to a power supply, which can supply maximum coil currents of 450 A corresponding to an axial field gradient of ~ 400 G/cm with a stability of $< 10^{-3}$. The coils are mounted on a holder of aluminum on a translation stage, which can move horizontally in the x-y plane. After the laser cooling sequences, the entire holder moves along a 2-dim. path to the BEC cell and carries the atom cloud along. The stage provides acceleration of up to 0.5g, so that the magnetically trapped atom cloud only spends 250ms in the MOT chamber ($\tau \sim$ 2s). The 2-dim. path allows further optical access along the x-axis and prevents hot atoms from the MOT chamber to spill into the BEC cell. The quadrupole coils are used in three different ways: magnetic field for MOT, transport of atoms and magnetic trap for evaporation. A picture of the real setup is shown in Fig. 2.4a) and an overview of the setup is given in Fig. 2.4b). Details of the vacuum and laser system design are discussed in [39], and of the magnetic transport in [40].

2.3 TOP trap

The quadrupole coils mounted on the holder of the transporter allow the atoms to be transferred into the BEC cell, so that the evaporative cooling can be carried out in the quadrupole trap. A major problem in this case are Majorana losses [41], which can occur near the trap center: if the absolute magnetic field seen by an atom passing near the trap center is so low that the Larmor frequency is on the timescale of the relative change of the magnetic field direction, the atomic spin can flip from a trapped to an untrapped state. As discussed in Chapter 3.3.2, this Majorana loss rate increases with decreasing temperature, so that for very low temperatures efficient evaporation is no longer possible and Bose-Einstein condensation is prevented, cf. Chapter 3.2.2.

---

[1] This condition is satisfied if the Larmor-frequency is much smaller than the rate of change of the magnetic field: $\omega_L << \frac{1}{B} |\frac{\mathrm{d}}{\mathrm{dt}} B|$

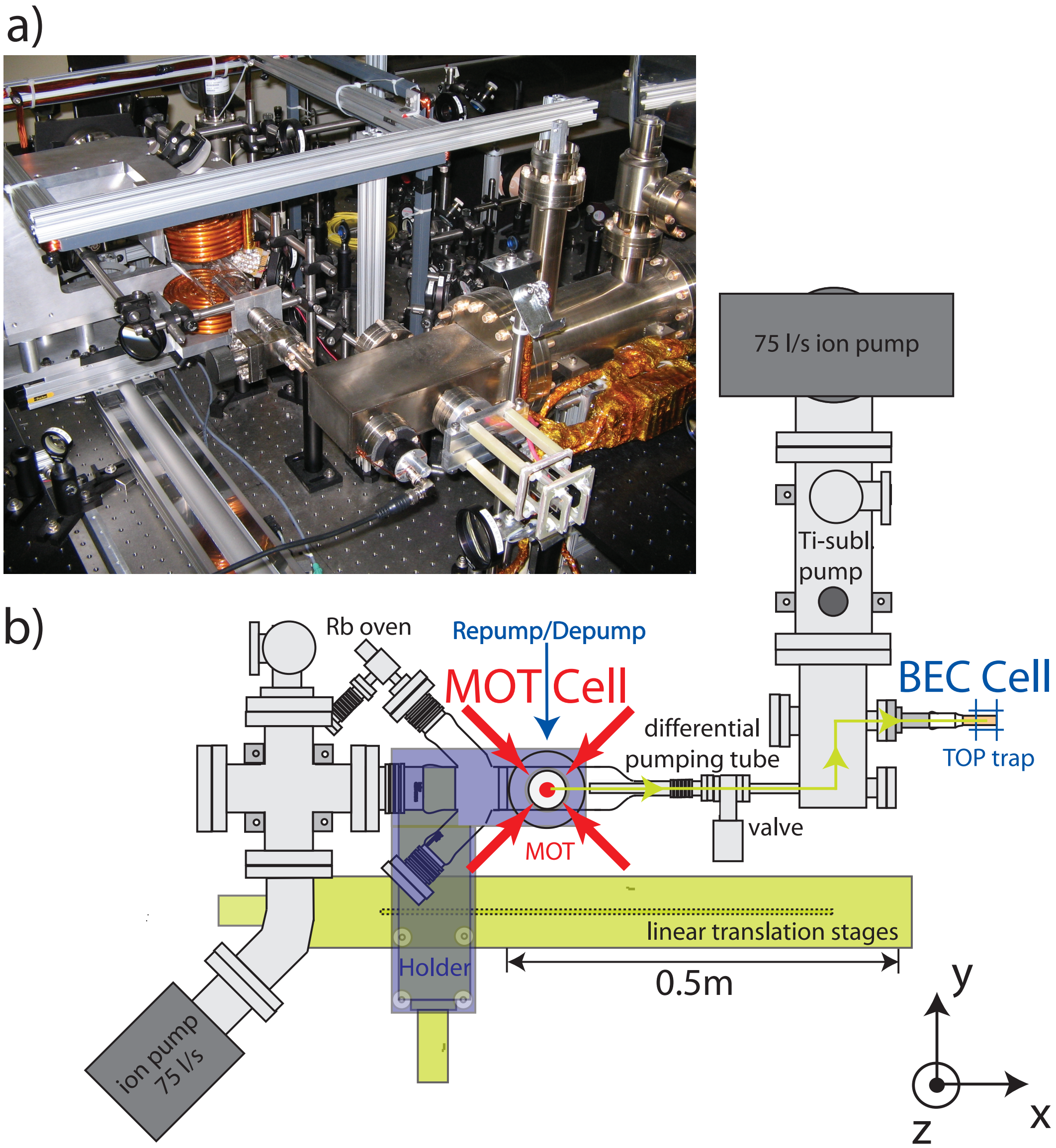

Figure 2.4: BEC apparatus. a) Picture of system. The quadrupole coils mounted on the holder on the two perpendicular translation stages are visible. The laser cooled atoms are transported along a 2-dim. path from the MOT cell through the differential pumping tube to the BEC cell for evaporative cooling in the TOP trap. The MOT cell pressure is about 10^{-8} torr for high MOT loading rates, while the BEC cell pressure is below 10^{-11} torr for lifetimes of ~ 130 s. b) Schematic view from above (along z axis). The MOT consists of six counter-propagating cycling laser beams with an additional repump/depump beam and the quadrupole coils on the holder. These coils are also used to transport the atoms to the BEC cell and are part of the TOP trap.

There are several ways to circumvent this problem. For example, the atom cloud can be loaded into a different type of magnetic trap with a non-zero field at the minimum so that the Larmor frequency does not become too small (Ioffe-Pritchard trap [42]). Alternatively, an optical trap can be used, which also has the advantage that not only atoms of a certain magnetic sublevel are trapped [43]. Instead of using a different trap, the "Majorana hole" in the quadrupole trap can be "plugged" with a blue detuned laser beam that repels the atoms from the center [11]. The method chosen for our experiment is the Time-Orbiting Potential (TOP) trap, first demonstrated by Cornell et al., [41]. The basic idea is to rotate the Majorana hole around the trap center by applying a rotating magnetic bias field B_{TOP}. Hence, the troublesome part of the quadrupole trap keeps hiding from the atoms, while they are still being trapped.

2.3.1 Theory

In a TOP trap the rotation frequency ω_{TOP} needs to be much higher than the trap frequencies ω_{trap} so that the atoms cannot follow the shifted trap minimum. In addition, ω_{TOP} has to be much smaller than the Larmor frequency ω_{larmor}, so that the spin can follow the rotating field and the atoms see an averaged potential.

$$\omega_{trap} << \omega_{TOP} << \omega_{larmor}$$

The instantaneous potential is formed by the usual interaction energy of the atomic magnetic moment μ and total magnetic field $|\vec{B}_{QP}(\vec{r}) + \vec{B}_{TOP}(t)|$. Assuming that the stiff quadrupole axis with a field gradient b is in the z direction, while the rotating bias-field is in the x-y plane, the potential is:

$$V(\vec{r},t) = \mu\sqrt{\left(\tfrac{b}{2}x + B_{TOP}\cos(\omega_{TOP}t)\right)^2 + \left(\tfrac{b}{2}y + B_{TOP}\sin(\omega_{TOP}t)\right)^2 + (bz)^2}$$

$$\vec{B}_{TOP}(t) = B_{TOP}\begin{pmatrix} \cos(\omega_{TOP}t) \\ -\sin(\omega_{TOP}t) \\ 0 \end{pmatrix} \tag{2.3}$$

Time-averaging over a full period of a bias field rotation then gives the average potential $\bar{V}(r,z)$ seen by the atoms. Near the trap center the potential can be approximated by a harmonic potential, which can be seen by taking a Taylor approximation for small distances. Neglecting the influence of gravity, this leaves [44]:

$$\bar{V}(r,z) \approx \mu B_{TOP} + \frac{1}{2}m\omega_{rad}^2 r^2 + \frac{1}{2}m\omega_{ax}^2 z^2, \quad \omega_{ax} = \sqrt{\frac{\mu b^2}{mB_{TOP}}} = \sqrt{8}\omega_{rad} \tag{2.4}$$

The aspect-ratio ω_{ax}/ω_{rad} between the shallow and the stiff direction is thus $\sqrt{8}$. The geometry is rotationally symmetric around the z-axis.

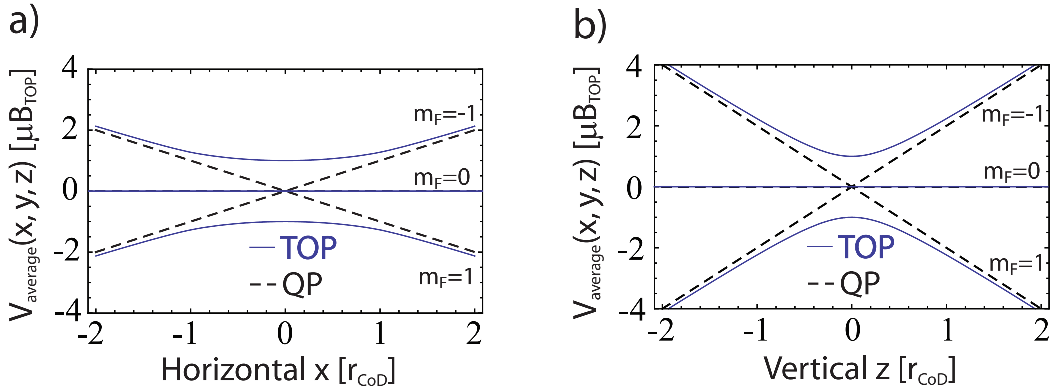

Figure 2.5: Illustration of average potential $V_{average}$ along different axes in TOP- and quadrupole trap for Rb-87 atoms in the F=1 ground state. The natural unit for the potential is μB_{TOP}, while r_{CoD} sets the length scale. This allows to omit the dependencies on trap-specific parameters. The harmonic approximation breaks down at r_{CoD}. Neglecting gravity, the aspect ratio is $\sqrt{8}$.

The average trapping potential along the x- and z-axis is illustrated in Fig. 2.5 for Rb-87 atoms in the F=1 ground state, both with and without the TOP trap. In the center the potential has an energy offset of $E_{off} = \mu B_{TOP}$. The Majorana hole rotates in the x-y plane at a certain distance r_{CoD} to the symmetry axis (z-direction). Since atoms are lost if they cross this boundary, this circle is referred to as "circle of death" (CoD). This is also a typical distance where the harmonic approximation for small distances to the trap is no longer valid and the potential approaches the quadrupole potential. If the bias field decreases, both the trap bottom and CoD radius decrease, while the trap-frequencies increase (trap stiffening).

$$E_{off} = \mu B_{TOP}, \qquad r_{CoD} = \frac{B_{TOP}}{b/2} \tag{2.5}$$

The effect of gravity can be included by adding mgz to the instantaneous potential from Eq. 2.3. A Taylor expansion around the new equilibrium position z_0, which is shifted downwards a little due to the "gravitational sag", yields to lowest order a harmonic potential with slightly changed trap frequencies depending on a parameter $\nu = mg/\mu b$. This also leads to a shift of the trap aspect-ratio. The details of the calculation are carried out in [44].

$$\bar{V}(r,z) \approx \mu B_{TOP}[\sqrt{1-\nu^2}+\frac{1}{4}\sqrt{1-\nu^2}(1+\nu^2)\left(\frac{r}{r_{CoD}}\right)^2+2(1-\nu^2)^{3/2}\left(\frac{z-z_0}{r_{CoD}}\right)^2]$$

$$\omega_{ax}/\omega_{rad} = \sqrt{8}\sqrt{\frac{1-\nu^2}{1+\nu^2}}, \qquad z_0 = -\frac{r_{CoD}\nu}{2(1-\nu^2)} \tag{2.6}$$

In our case b$\sim$ 350G/cm, so that $\nu \sim 0.1$. The trap aspect-ratio changes by only 1%, so that the effect of gravity is very small from that aspect. But the shift of the equilibrium position is approximately 5% of r_{CoD}, which is about 10 condensate diameters for $B_{TOP} = 18\ G$.

2.3.2 Trap desgin

The TOP trap is formed by the quadrupole coils from the transporter and a rotating bias field. The rotating bias field is produced by two perpendicular coil pairs each in Helmholtz configuration in the x-y plane (lab coordinates), through which an ac current is driven 90° out of phase. In addition to that, several specifications have to be fulfilled:

- Large and tunable bias field, so that the initial cloud fits into CoD and trap can be stiffened during evaporation
- Very uniform field ($\sim 10^{-4}$) on the length scale of the expected condensate and translation stage position reproducibility for stable trap bottom (RF-knife very close to trap bottom at onset of condensate)
- Reasonably uniform field over initial cloud size ($\sim 10^{-2}$) for clean trap potential
- Coil current stabilization ($\leq 10^{-3}$) for stable trap bottom
- Adiabaticity condition: $\omega_{trap} << \omega_{TOP} << \omega_{larmor}$
- Optical access to BEC cell not blocked by coils

For axial field gradients of ~ 100 G/cm typical TOP trap frequencies are $(10 \times 2\pi)$ Hz, while the Larmor frequencies are usually around $(1 \times 2\pi)$ MHz. The bias field rotation frequency is chosen to be $\omega_{TOP} = 10 \times 2\pi$ kHz.

The geometry of each coil pair is such that they fit in between the quadrupole coils of the translation stage, are in Helmholtz configuration and in the shadows of the edges of the BEC cell. The exact geometry is shown in Fig. 2.6a), while a picture of the real setup is given in Fig. 2.6b). Copper wires with 500 μm diameter (AWG 24) are used to form the rectangular coils - hollow copper tubes would be very bulky and take away a lot of space around the BEC cell. To ensure large enough bias fields at reasonable currents of a few A, the coils have 20/25 turns. That way, a current of ~ 8 A creates a 60 G bias field, which corresponds to a CoD radius of 3 mm. The coils are glued to coil holders made of glass fiber, which is very stiff and is not electrically conducting (eddy currents).

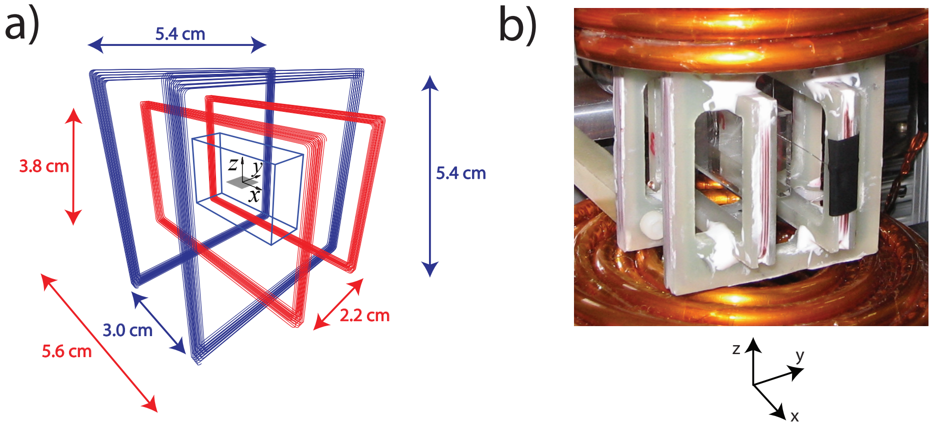

Figure 2.6: Design of TOP coils. The rotating bias field is created by two pairs of rectangular coils in Helmholtz configuration in the x-y plane of the lab coordinates. The symmetry axis of the quadrupole trap is in z-direction. a) Schematic view with all measures. The geometry is chosen such that the magnetic field curvature of each coil pair vanishes in the center and the coils are in the shadow of the BEC cell edges [45] b) Setup in the experiment. The TOP coils are mounted on a fiber glass holder, which is connected to the vacuum chamber via 4 posts. The setup just fits in between the quadrupole coils from the transporter.

Simulations of the magnetic field at the center of the BEC cell show that on a length scale of 100 μm the field is uniform to $\sim 10^{-5}$, while this reduces to $\sim 10^{-4}$ for 1 mm [45]. This could be roughly confirmed experimentally. The simulated bias field calibration is ~ 7.5 G/A, which matches Hall probe measurements. Since only passive air cooling is available, serious heating occurs, if too high currents flow through the coils for too long. For example, after 30 s of 8 A, the wire temperature increases from room temperature to 65 °C. Since the evaporation timescale is expected to be around 30-60 s, the current

should not be higher than 8 A - although the bias field is ramped down during evaporation. The maximum bias field for our TOP trap is 60 G.
Matching capacitors in series with the coils minimize the impedance at 10 kHz down to the ohmic resistance of the coils (impedance matching). A 800W audio amplifier provides the necessary currents. In addition, active current stabilization is necessary to compensate for the rise in resistance with increasing coil temperature. The current stabilization quality is found to be at least 10^{-3}. The timescale for switching the TOP on and off is $\sim$ 1...2ms. The bias field is controlled by the computer (analog channel).

2.4 RF evaporation coil

2.4.1 Coil design

Our setup allows to perform evaporative cooling in both the harmonic TOP and linear quadrupole trap. The process inducing the evaporation of the hottest atoms in the BEC cell is RF-forced evaporation. The basic idea is that a magnetic RF field induces spin-flips from trapped to untrapped magnetic sub states on an evaporation shell around the trap center. This shell is given by the resonance condition between the Zeeman splitting energy and the RF photon energy $h\nu_{RF}$. Evaporative cooling can then be performed by ramping down the RF frequency. The higher the magnetic RF field amplitude, the more probable the spin-flip transition is and the cleaner the evaporation shell. But for very cold clouds the RF power has to be reduced due to power broadening. A detailed discussion of the involved mechanisms is carried out in Chapter 3.2.1. In this section only the design and characterization of the RF-coil are explained. In principle, the experimental setup has to fulfil a few specifications:

- Large oscillating magnetic field tunable in amplitude and frequency - typically in the 1-100 MHz range
- Amplitude only weakly dependent on frequency (no resonances)
- Optical access to BEC cell not decreased
- Magnetic field spatially uniform for well defined evaporation shell

As shown in Fig. 3.4, maximum RF amplitudes of 100 mG are definitely sufficient. The requirement of a uniform amplitude-frequency spectrum is of particular importance, because resonances can cause the evaporation to be very inefficient when ramping the RF-frequency over these resonances.

The RF field is created by a RF-coil, which is mounted directly in the square beneath the BEC cell formed by the coil holders of the TOP coils, so that the optical access is not affected (3.0cm × 2.2cm). The orientation of the magnetic RF field amplitude is in the z-direction of the lab coordinates, so that the trap symmetry is conserved and the size of the evaporation hole is minimized, cf. Fig. 3.5. A Helmholtz-geometry is not chosen in order to reduce the amount of wires close to the BEC cell.
Fields in the range of 100 mG require coil currents on the order of ~ 500 mA for coils of this size. Under this condition, only ~ 100 mW are directly dissipated by the coils. Thermal heating is thus negligible, so that active cooling is not necessary. Therefore, thin copper wires with 1.1 mm diameter (AWG 18) are chosen. Simulations show that for an ac voltage source of constant amplitude the magnetic field at the center of a (round) coil is maximized, if the coil turn number and the enclosed area are minimized. A picture of the one-turn RF coil mounted in between the TOP coil holders directly beneath the BEC cell is shown in Fig. 2.7a).

The initial cloud before evaporation in the BEC cell has a diameter of about 4 mm, which corresponds to about 400 μK in the quadrupole trap with 350 G/cm axial field gradient. Calculation results of the expected field profile in the near-field regime (distance to coil: $\sim$ cm, RF-wavelengths $\sim$ m) are shown in Fig. 2.7b)+c): concerning the horizontal directions, the magnetic field in the z-direction is uniform to within a few percent. In contrast the profile in the axial direction shows a strong gradient resulting in a modulation of $\pm 20\%$. This does not play a role in the beginning of the evaporation, because the magnetic field amplitude is so high that the evaporation shell can still be considered "sharp". For very cold clouds, where the RF power needs to be reduced (power broadening), the relative variation of the field amplitude in the axial direction will have reduced to a few percent due to the small cloud size.

2.4.2 RF electronics

The RF signal is created by a function generator (FG Agilent 33250A, 80MHz) connected to a class-A 40 dB 10 W RF amplifier (Delta RF, LA-10-1-512-40) to compensate for the high RF coil impedance for frequencies in the MHz range and to create large enough currents. This amplifier has an input/output impedance of 50 Ω, so that at a maximum input voltage of 400 mV the average output power is still below 10 W for a 50 Ω resistor connected to the output. For protection, attenuators convert the FG maximum output

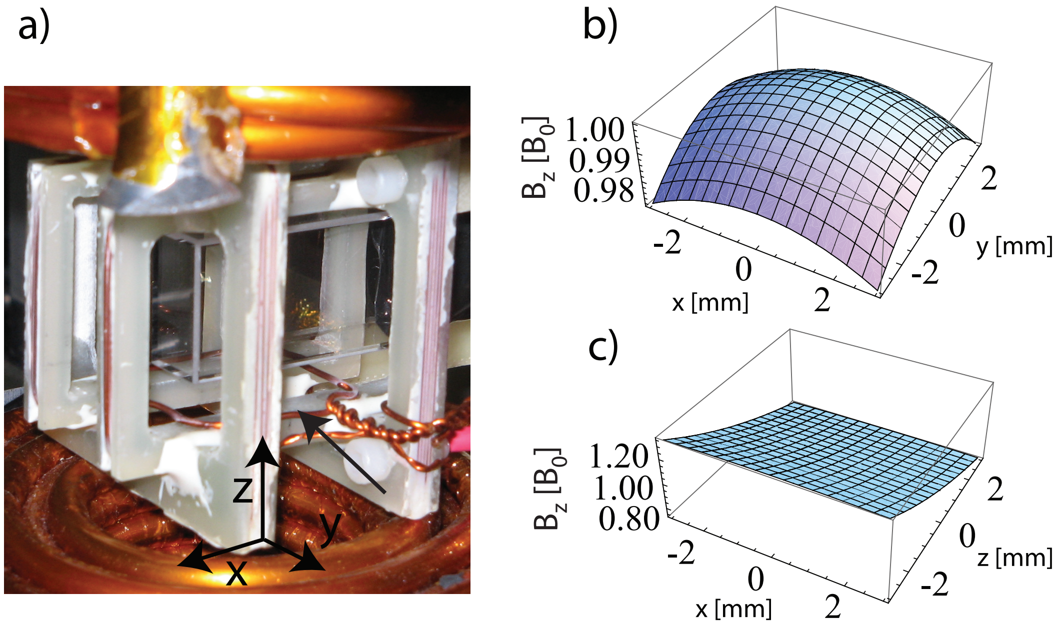

Figure 2.7: Design of RF coil for evaporative cooling (arrow). a) Picture of RF coil mounted directly beneath the BEC cell in between the TOP coil holders. The orientation of the magnetic field at the location of the atom cloud is in z-direction. b)+c) Simulations of the spatial field amplitude profile in z-direction in units of the amplitude at the trap center. The calculation is based on the RF coil geometry used for the experiment.

voltage of 10 V to 400 mV. The amplifier itself is mounted on a heat sink, since class-A amplifiers dissipate a significant amount of the maximum output power. An additional fan provides the necessary air circulation.
The function generator is connected via GPIB to the computer, from which both frequency and amplitude can be controlled. Typical update times are $\sim$100-200 ms. To have precise control over the RF, a digital switch is included with a reaction timescale of about 100 ns. This allows the RF-knife to be precisely turned on/off at the critical point where the BEC sets in. To prevent ground loops, an additional opto-coupler is installed. A schematic overview of the setup is given in Fig. 2.8.

The amplifier output to the RF coil is governed by four main factors, which cause the RF coil current amplitude not to be uniform over frequency:

- The RF amplifier has a variation of 1-2 dB amplification in the frequency range of 1-80 MHz

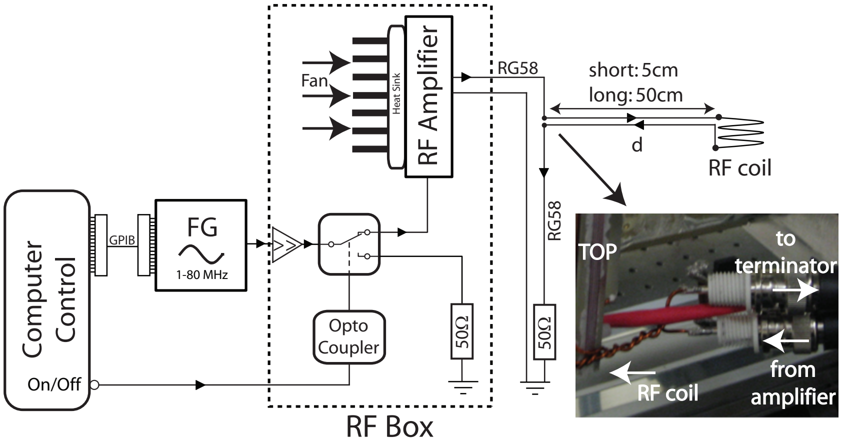

Figure 2.8: Schematic design of RF electronics to create RF fields. The main part is in the RF box. A BNC cable (RG58) connects the RF amplifier output to the RF coil and 50 Ω power terminator (75 W). Large distances d of around 50 cm between connector and RF coil cause significant resonances in the B-field amplitude spectrum of the RF coil. The inset shows a picture of the connector used in the experiment, so that the distance d is kept as short as possible (~ 5 cm).

- The total output impedance is a function of frequency
- Reflections in the cable from the RF Box to the RF coil cause frequency dependent resonances of the coil voltage drop (RF wavelengths ~ 1 m)
- Capacitive/inductive coupling to the environment (other coils, optical table, cables) around the RF coil creates additional resonances

These effects typically cause B-field modulations of 1-2 orders of magnitude for frequencies of 1-80 MHz.

To protect the amplifier a 50 Ω high power terminator (75 W) is connected in series with the RF coil so that the total impedance is about 50 Ω and dominated by the ohmic resistance (in particular important for low frequencies, where the reactance is much smaller than 50 Ω). A BNC cable (RG58) is used to connect the amplifier to the RF coil. The coil ends are connected to the center conductor of the cable, creating a difference in path length between the ground and center wire connected to the terminator, cf. Fig. 2.8, which is the main cause for resonances. Therefore, the terminator cannot cancel the cable resonances, if the connection between the RF coil and BNC-cable is too long. A measurement of the magnetic field spectrum shows an order of magnitude improvement of the resonance behavior between a long (50 cm) and a short (5

cm) connection, cf. Fig. 2.9a).
The remaining resonances due to capacitive/inductive coupling to the environment are reduced by "shortening out" the contacts, as explained in [46]: all elements, to which the RF couples, are connected to each other and directly grounded at only one point to avoid loops. The distances are kept as short as possible to avoid resonances in the RF shield. The efficiency of the shields are observed by measuring the induction voltage from a pickup coil at different points in the lab. The major shielded elements are:

- BNC cables/connectors from RF box to RF coil
- Audio cable from TOP box to TOP coils
- Quadrupole coil holder and power cables

In most cases aluminum foil was wrapped around the objects with duct tape for isolation. This way, the RF resonances in the lab could be suppressed significantly.

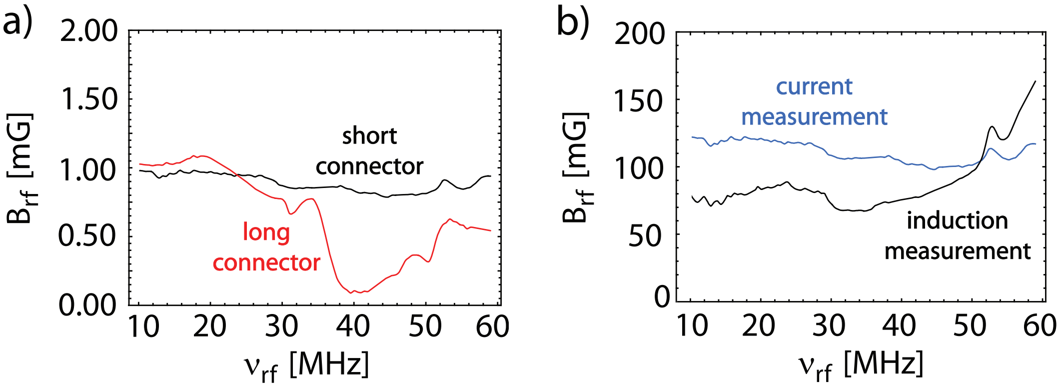

Figure 2.9: Magnetic field amplitude B_{rf} at BEC cell center as a function of the RF frequency. a) Comparison between short (~ 5 cm) and long connector (~ 50 cm) setup. The amplifier output was set to 1% of the maximum output. The long connector data shows a resonance between 40-50 MHz, where the field drops to 10%, while the field spectrum is very uniform for the short connector version. The magnetic field was determined by measuring the current through the RF coil b) Measurement of B_{rf} (short connector) at maximum amplifier power. Two different methods are chosen to cross-check - they agree at least within a factor of 2.

The magnetic field B_{rf} at the center of the BEC cell as a function of RF frequency ν_{rf} at full amplifier output power is determined by observing the induced voltage of a pickup coil mounted above the RF coil (x-y plane). To cross-check this measurement, the current through the terminator is measured, and the magnetic field created by this current through the RF coil is calculated. The results for the short coil connector - as used in the BEC experiment - are shown in Fig. 2.9b).

The amplitude spectrum at full amplifier power is roughly uniform at around 100 mG with a systematic error of[2] $\sim 50\%$. Possible reasons for deviations are resonances due to coupling to the environment, since the RF shields were not yet installed when the data was taken. In addition, the determination of the coil current is not accurate due to remaining cable resonances in the RF coil circuit. However, resonances causing field drops of 1-2 orders of magnitude are clearly not present.

2.5 Imaging of atom clouds

2.5.1 Setup

Atom number and temperature of the atom cloud are obtained by imaging the cloud onto a CCD chip (PI PIXIS 1024B, pixel size $(13\mu\text{m})^2$, 1024×1024 pixels), which counts the number of arriving photons at every pixel with a quantum efficiency of $\sim 70\%$. One possibility for the cloud observation is fluorescence imaging, where a certain solid angle of spontaneously emitted light from the atoms is captured and guided into the camera. The emission is induced by laser light resonant with a closed optical transition above the saturation intensity I_s ($\sim 4\text{mW/cm}^2$ for the Rb-87 cycling transition), so that the decay rate of the excited atom is well defined. Due to the high recoils in this regime, the atom cloud has to be excited from all six spatial directions. This type of imaging is available in the MOT cell, where the six MOT beams can be used to drive the cycling transition, while the repumper is still on to make the transition closed. The details of the atom number and temperature extraction with this method are explained in [40].

One of the disadvantages of this procedure is its sensitivity to reflections by the glass of the MOT cell or the differential pumping tube. This reduces the signal-to-noise ratio and hence limits the minimum atom number detectable to typically 10^8 in our setup. An alternative method is absorption imaging, where "darkness" instead of "brightness" is measured. More precisely, a laser beam resonant with an optical transition is shone along an axis on the atom

---

[2] The data shown here is for a different coil position and geometry than used in the experiment - significant changes in amplitude are however not expected.

cloud and the relative intensity absorption is measured by imaging the shadow of the cloud onto the CCD chip. If the absorption cross section is known, the atom number can be calculated, while the temperature can be extracted from either the initial cloud profile or its expansion behavior. Quantitative details can be found in the next section. One advantage is that absorption of the imaging beam due to other objects are normalized out, because the images with and without the atom cloud are compared for the quantitative analysis. Moreover, the evaluation is independent of the beam intensities in the regime below saturation. This method is used to characterize the atom clouds in the BEC cell.

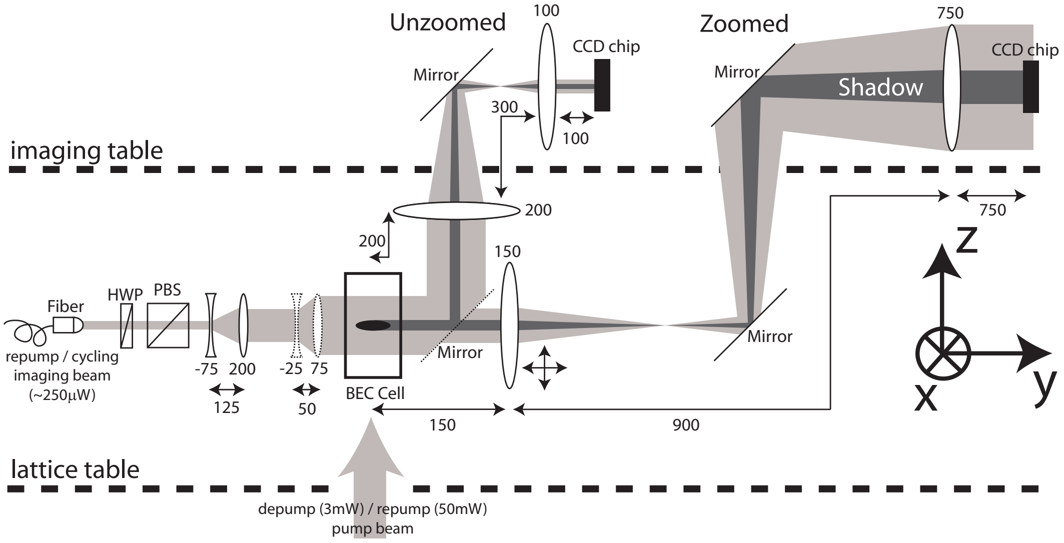

Figure 2.10: Schematic view of imaging setup (not to scale, some mirrors are not shown). Either the cycling or repump beam can be used as imaging beam. The first telescope behind the fiber increases the beam size for the zoomed imaging, while the additional expander (dotted) is necessary for the unzoomed imaging, because a larger area in the x-z plane of the atom cloud is observed. The axial symmetry axis of the atom cloud is in the vertical z-direction, so that the anisotropy is observable when imaging along the y-axis. Switching between the zoomed and unzoomed imaging requires the dotted optical elements to be inserted and the camera to be repositioned. The repump/depump beam is necessary to close the optical transition.

A schematic view of the setup is shown in Fig. 2.10. The imaging axis is along the y-axis (lab coordinates), so that the cloud anisotropy is observable. Since the cloud diameter decreases by about a factor of 100 during evaporative cooling, two different optical pathways are possible: the unzoomed imaging (dashed elements inserted) has a demagnification of ~ 2 to observe

the initial cloud before evaporative cooling, while the zoomed imaging has a magnification of 5, so that the condensate extends over roughly 10 pixels in one dimension on the CCD chip. The resolution in the zoomed case approximately corresponds to the diffraction limit ($\sim 2-3\ \mu$m). Position holders for the optical elements allow quick switching between the two possible beam paths (dashed elements in Fig. 2.10). Most optical imaging elements behind the BEC cell are mounted on the imaging table above to increase free space for future lattice optics. The objective lens is mounted on two perpendicular translation stages to focus on the cloud and to correct for the effect of gravity causing the cloud to fall out of the field of view of the CCD chip for "times of flight" (TOFs) larger than 20 ms. The atom clouds cannot be observed while the magnetic trap is still on, because the Zeeman-effect shifts the atoms out of resonance. After 0.5 ms the quadrupole coil current has decreased to almost zero, but still exhibits minor oscillations for another 1.5 ms. Since the TOP trap is already off after 1 ms, the imaging beam is turned on 2 ms after switching off the magnetic traps.
The imaging setup allows to observe both F=1 and F=2 Rb-87 atom clouds. Either the F=2 (cycling transition) or F=1 (repump transition) imaging beam can be used. For the imaging transitions to be effectively closed, cycling imaging requires an additional repump beam, as in the case of laser cooling in the MOT cell, while a depump is necessary for F=1 repump imaging. This is accomplished by a second beam along the vertical z-axis providing either repump or depump light at intensities around 1 mW/cm^2. All data for this thesis was obtained by repump imaging of F=1 atom clouds without the depump light.

2.5.2 Extraction of cloud parameters

For every absorption image, the number of counts at every pixel of the CCD chip is returned in form of a matrix $I(\tilde{x}, \tilde{z})$. The entries of this matrix then correspond to the laser intensity at this point in relative units. If the length calibration of the imaging setup is known, this matrix can be converted into the real coordinates of the atom cloud, noted by $I(x, z)$. To obtain the density distribution of the atom cloud, three pictures are taken: the first one is with the atom cloud and imaging beam turned on ($I_{atoms}(x, z)$), while the second one is a reference picture without atoms ($I_{ref}(x, z)$). The last picture is a background picture ($I_{bkg}(x, z)$) without the atom cloud and imaging beam, which is used to subtract the background noise from the CCD chip as well as residual stray light. The transmission $T(x, z)$ of the imaging light is then given by:

$$T(x,z) = \frac{I_{atoms}(x,z) - I_{bkg}(x,z)}{I_{ref}(x,z) - I_{bkg}(x,z)} \tag{2.7}$$

For imaging beam intensities I much smaller than the saturation intensity I_s and laser line widths much narrower than the optical transition line width, the on resonance absorption cross section σ becomes constant. Under this condition, the absorption is given by [6]:

$$I(x,z) = Ie^{-\sigma n_{2D}(x,z)}, \qquad n_{2D}(x,z) = \int_{-\infty}^{\infty} n(x,y,z)dy \tag{2.8}$$

Here $n_{2D}(x,z)$ is the 2-dim. column density and $n(x,y,z)$ is the actual atom cloud density. Introducing the optical density $OD(x,z)$, the 2-dim. column density can then be determined from the three images:

$$n_{2D}(x,z) = \frac{OD(x,z)}{\sigma}, \quad OD(x,z) = -\mathrm{Log}\left(\frac{I_{atoms}(x,z) - I_{bkg}(x,z)}{I_{ref}(x,z) - I_{bkg}(x,z)}\right) \tag{2.9}$$

In essence, the total atom number N is proportional to the integrated optical density on the CCD chip. The proportionality factor (atom number calibration cal_{atnum}) is then a function of the cross section σ and length calibration.

$$N = \mathrm{cal}_{atnum} \int_{-\infty}^{\infty}\int_{-\infty}^{\infty} OD(\tilde{x},\tilde{z})d\tilde{x}d\tilde{z} \tag{2.10}$$

Since the imaging transition is not closed for F=1 repump imaging, the introduction of an effective cross section would be necessary in this case. As an alternative, the atom number can be determined by fluorescence imaging in the MOT cell before and after transport and compared with the integrated optical density from absorption imaging of the same atom cloud in the BEC cell. The resulting atom number calibration has a systematic error of $\sim 20\%$, because it is not clear if the transport losses are one- or two-way.

To determine the temperature, the initial atom cloud profile right after release from the magnetic trap can be extracted from the images. The 1-dim. column densities can be obtained by integration of the 3-dim. profiles. This yields for the quadrupole/TOP trap:

$$
\begin{aligned}
n_{3D,QP}(x,y,z) &\propto e^{-\frac{\mu b\sqrt{x^2+y^2+4z^2}}{2k_BT_x}} && (2.11)\\
n_{3D,TOP}(x,y,z) &\propto e^{-\frac{m\omega_x^2x^2}{2k_BT_x}}e^{-\frac{m\omega_y^2y^2}{2k_BT_y}}e^{-\frac{m\omega_z^2z^2}{2k_BT_z}} && (2.12)\\
n_{1D,QP}(x) &\propto \int_{-\infty}^{\infty}\int_{-\infty}^{\infty} e^{-\frac{\mu b\sqrt{x^2+y^2+4z^2}}{2k_BT_x}}dydz && (2.13)\\
n_{1D,TOP}(x) &\propto e^{-\frac{m\omega_x^2x^2}{2k_BT_x}} = e^{-\frac{x^2}{2\sigma^2}} && (2.14)
\end{aligned}
$$

In this case, μ is the projection of the magnetic moment along the magnetic field axis, while b is the axial field gradient of the quadrupole trap. A fit according to Eq. 2.14 or 2.13 to the integrated optical density $OD(x,z)$ then gives the temperature. In most cases, the two temperatures T_x and T_z from the x- and z-axis fit are the same within 5%.
Alternatively, the expansion of the cloud can be observed directly. For the harmonic trap, the cloud profile stays Gaussian for all times - with the only difference that the width has increased [40]:

$$\sigma_x(t) = \sqrt{\sigma_{x,0}^2 + \frac{k_BT}{m}t^2}, \qquad \sigma_{x,0} = \sqrt{\frac{k_BT}{m\omega_x^2}} \tag{2.15}$$

The main idea is to observe the 1-dim. column density for different TOFs and fit a Gaussian curve to each one. This gives the cloud widths at different times, to which Eq. 2.15 can be fitted to obtain the temperature. Typically, five different TOFs are sufficient to give robust results. Simulations show that the expansion behavior of an atom cloud initially in the quadrupole trap can also be approximately described this way with an error of $< 10\%$.
The temperatures determined from both methods agree well within 10%. Since the first method requires fewer images and is therefore much faster, this approach is chosen when optimizing the BEC machine.

From the atom number N and temperature T, the maximum density n and phase-space density PSD in the center of the trap can be calculated. In the case of the harmonic TOP trap, the cloud volume can be obtained from the Gaussian widths σ_x and σ_z of the 1-dim. column densities obtained by the fits:

$$n_{TOP} = \frac{\sqrt{8}N}{\pi^{3/2}\sigma_x^2\sigma_z}, \qquad PSD_{TOP} = \frac{h^3 n_{TOP}}{(2\pi m k_B T)^{3/2}}$$

In the case of the quadrupole trap, the temperature from the fit can be used:

$$n_{QP} = N\left[\int_{-\infty}^{\infty}\int_{-\infty}^{\infty}\int_{-\infty}^{\infty} e^{-\frac{\mu b\sqrt{x^2+y^2+4z^2}}{2k_BT_x}}dxdydz\right]^{-1}, \quad PSD_{QP} = \frac{h^3 n_{QP}}{(2\pi m k_B T)^{3/2}}$$

2.5.3 Imaging parameters

Imaging laser intensity and exposure time are governed by several competing effects:

- Intensities above saturation ($I > I_s$) cause intensity dependent cross sections and blow away the cloud
- Signal-to-noise ratio improves with increasing intensity I and/or exposure time
- Exposure times greater than 150 μs cause the condensate to wash out along the vertical axis at large TOFs due to gravity

Intensities of about 500μW/cm^2 are used in the experiment, which is still well below the saturation intensity, while the detection time is set to 150μs [3]. The signal-to-noise ratio is optimum if the camera is almost saturated, i.e. the counts/pixel are slightly below the maximum count value of 64,000 for an absorption image. While this is the case for the unzoomed imaging, the maximum count for the zoomed imaging is reduced to only ~ 3000, because one pixel now corresponds to a much smaller area in the imaging plane of the atom cloud.

Apart from these imaging parameters, a few more points have to be considered:

- Frequency: To increase the signal-to-noise ratio, zero detuning is chosen to increase the absorption. Under this condition, the cross section - and hence the predicted atom number - can be frequency sensitive (transition line width $\sim$ 6MHz). Since the jitter of the cycling laser is on the order of 10-20MHz, many images of the same cloud are necessary for F=2 imaging to give a reliable atom number. In contrast, the line width of $\sim$ 1MHz of the repump laser is sufficient to give reliable atom numbers within 10%, as measured in Chapter 4.6.2.

---

[3] For the unzoomed imaging this corresponds to an output power of $\sim 250\mu$W behind the imaging fiber, which reduces to about $\sim 25\mu$W for the zoomed version (no beam expander before BEC cell, cf. Fig. 2.10).

- Polarization: The cross section also depends on the imaging laser polarization and the population of the levels. The incident light is π polarized in z-direction (labcoordinates) and the quantization axis is provided by a bias field of a few G in the same direction.

- Focusing: If the atom cloud is out of focus, blurring will wash out the profile. If the laser frequency is not exactly on resonance, diffraction patterns (e.g. Poisson spot) will occur due to the dispersive relation of the real part of the refractive index. The optimum objective lens position was found by minimizing the cloud size for a condensate without TOF. However, for TOFs smaller than 10ms, interference fringes around the condensate are still present.

The length calibration cal_{length} of the imaging (conversion of pixel size to length) can be obtained by observing the vertical condensate position z(t) on the CCD chip for different times of flight and fitting the function:

$$z(t) = z_0 - \frac{1}{2\mathrm{cal}_{length}} g t_{TOF}^2 \tag{2.16}$$

The center of the atom cloud for each image can be estimated by fitting a Gaussian distribution to the 1-dim. column density $n_{1D}(z)$. Fig. 2.11 shows the data for the zoomed imaging, which gives $cal_{length} = (2.6 \pm 0.01)\mu\mathrm{m/pixel}$. The error stems from the fit.

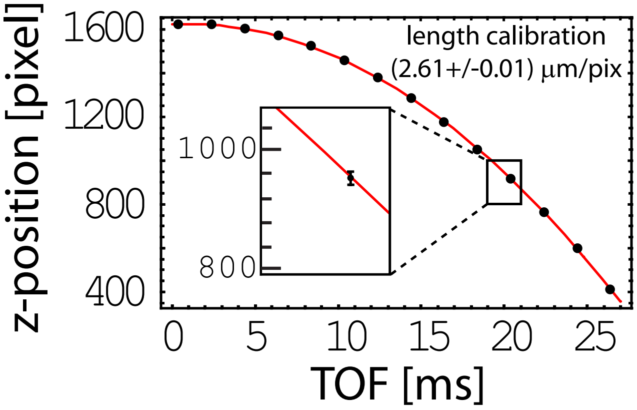

Figure 2.11: Length calibration for the zoomed imaging obtained from free falling BEC. By fitting a parabola according to Eq. 2.16, the length calibration can be extracted. The inset shows the very small size of the statistical error bars.

Chapter 3

Achieving Bose-Einstein Condensation

Optimization of both the laser cooling and evaporative cooling sequences are important for successful creation of a Bose-Einstein Condensate. Rapid production of large condensates thus benefits from theoretical modeling of the various steps to guide the experimental sequence, as the overall optimization of a BEC machine is a priori a high dimensional nonlinear problem.

In the first part of this chapter the sequence details of the laser cooling processes MOT, compressed MOT (CMOT), Optical Molasses and hyperfine state preparation are briefly sketched as well as the magnetic transport of the atom cloud into the BEC cell. The second part introduces the theory of RF-forced evaporative cooling (static and dynamic case) and provides a guideline for the optimization protocol by evaporation simulations. Experimental results of the new cloud production sequence and optimized evaporation are presented in the third and last part of this chapter.

All sequence values given are rough values and always require tuning on a weekly-monthly basis. This is mostly due to drifts of the mirrors or changing background environment in the MOT cell. Reoptimization of the optical sequences is thus required, while the dark part is very stable and requires no tuning. Usually tweaking of the Molasses parameters is enough to achieve the desired atom numbers and temperatures in the BEC cell.

3.1 Laser cooling and magnetic transport

The physics behind all the different laser cooling sequence steps are not discussed here and are assumed to be known. General explanations of the involved mechanisms can be found in [6, 47–49]. The details and influence of system parameters in a MOT are discussed in [50–55] and for the Optical Molasses and Sub-Doppler cooling mechanism in [56, 57]. Different magnetic traps are explained in [58].

The laser cooling sequence illustrated here is a slightly modified version of the original one developed by S. Albert [40]. The primary optimization guideline was first atom number and then temperature. The sequence produces atom clouds of 1.5×10^9 Rb-87 atoms in the F=1 hyperfine state in the BEC cell at temperatures of $\sim$ 700μK in the fully compressed trap.

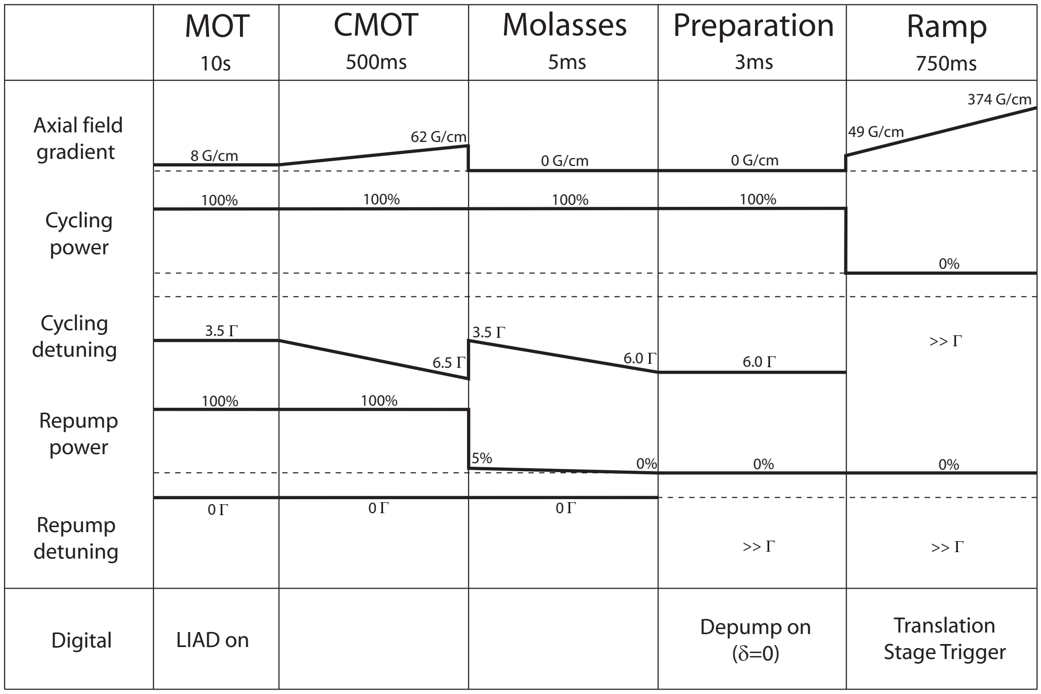

Figure 3.1: Illustration of the sequence for an N optimized F=1 atom cloud production in the BEC cell. This sequence is a slightly modified version of the original one developed in [40]. All given values are rough values and require tuning on a monthly basis. The repump beam is detuned far off resonance to prevent leaking repump light in the preparation step. The absolute values for the beam intensities are given in Chapter 2.1.2.

Concerning optimization, high atom numbers at very low temperatures in the magnetic trap are desirable, as they enhance the evaporation efficiency and thus the condensate size and production time. Consequently, the laser cooling sequences create high atom number clouds while keeping it very dense and small. The exact sequence settings are listed in Fig. 3.1, while the cloud parameters are illustrated in Fig. 3.2.

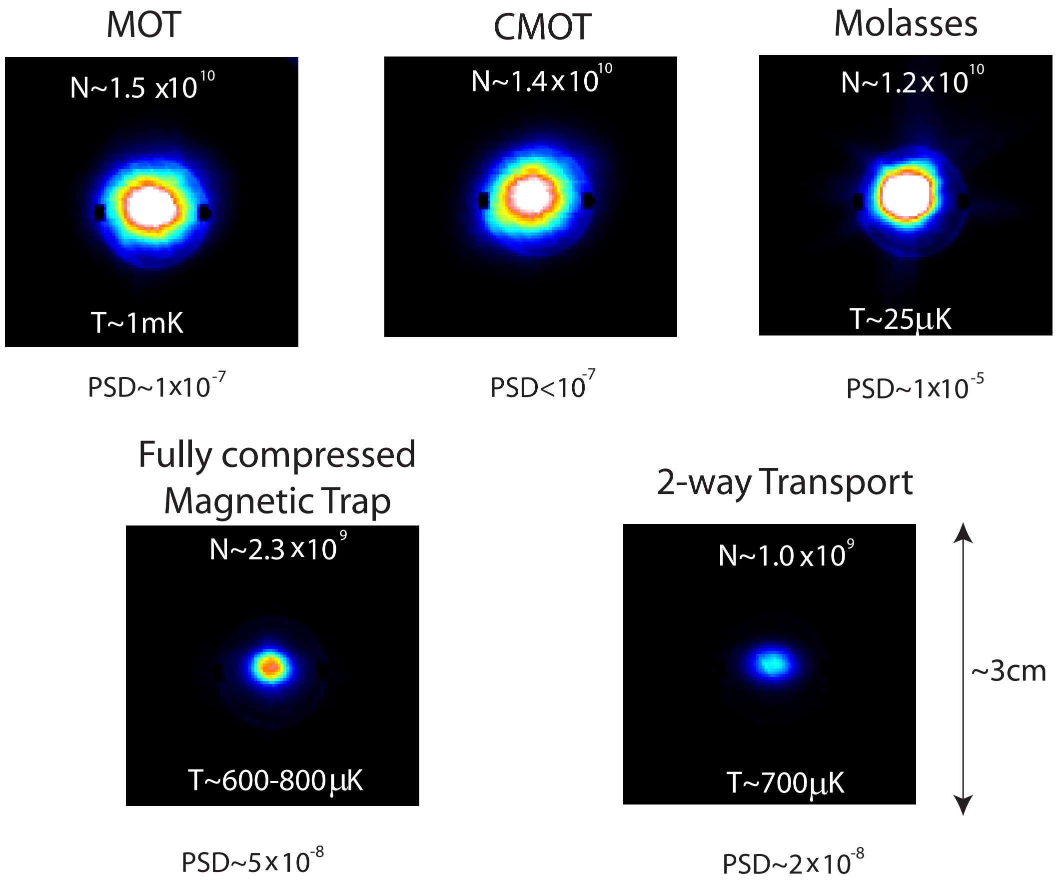

Figure 3.2: Atom clouds after different stages of N-optimized F=1 atom cloud production in the MOT cell. All clouds have a TOF of 2ms and the atom number was determined by fluorescence imaging. The temperature after the CMOT is too hot to be determined. The shift of the molasses compared to the tube visible as a ring suggests a slight misalignment of the magnetic trap center and cycling beams center. The atom cloud is round before transport and thus not thermalized, while showing the expected elliptical shape after transport ($\sim$ 3s). The huge temperature increase in the fully compressed trap is due to an already very high temperature after magnetic catch of $\sim 150\mu$K.

- MOT: A very low field gradient with a moderate red detuning is chosen to increase the capture range and loading rate from the background vapor. Typically 1.5×10^{10} atoms are caught at ~ 1 mK, so that the magneto-optical trap is in the density limited regime of photon-reabsorption. The decreased lifetime due to the high Rb background density can be improved by using light induced atomic desorption (LIAD), which removes adsorbed atoms from the glass of the MOT cell and causes a temporary pressure increase during the MOT loading phase [59].

- CMOT: For the compressed MOT stage the field gradient is ramped up in 500 ms to reduce the cloud size by overcoming the repulsive photon-reabsorption force. The time scale is short enough to use the transient behavior of the steady state MOT atom number. The detuning is also ramped so that the atoms do not spill out of the trap. Losses in atom number are negligible, while serious heating occurs (several mK).

- Optical Molasses: The small but hot atom cloud is "frozen out" by switching off the magnetic trap and ramping the detuning in 5 ms. In addition, the repump detuning is also ramped to increase the density. Only very few atoms are lost during this procedure, so that typically 10^{10} atoms at around 25 μK are available in a mixture of magnetic substates. The temperature is limited by the Sub-Doppler cooling mechanism [1]. The efficiency depends critically on the alignment of the beams in respect to the trap center while being very robust towards variations of the cloud parameters.

- Hyperfine preparation: Two ground states are available for Rb-87 (F=1, F=2) with the trappable states are $|1,-1\rangle$ or $|2,1\rangle$ and $|2,2\rangle$. For F=1 atoms, both the depump beam and the cycling beam (full power) are turned on while the repump beam is blocked away. The cycling detuning is the final ramp value of the previous sequence, so that a dark optical molasses is still present. Approximately 3×10^9 $|1,-1\rangle$ atoms are then trappable. A preparation sequence is not necessary for F=2 atoms, as the repump beam is still on during the Optical Molasses. Since a single clean magnetic substate is desirable for the evaporation to prevent hyperfine spin changing collisions reducing the trap lifetime, F=1 atoms are produced. Several groups report comparable successes in creating F=1 and F=2 Rb-87 condensates [61–63].

---

[1] For not too large detunings the Sub-Doppler temperature follows $T_{SubD} \propto \frac{I_{cycl}}{\delta}$ [60].

- Magnetic transport into BEC cell: The F=1 atoms are caught at a sufficiently high field gradient to prevent spilling due to gravity so that most of the trappable atoms are caught - typically 2.3×10^9. Due to the trap asymmetry the cloud is initially not thermalized. This part is followed by an adiabatic ramp of the quadrupole trap up to 353G/cm in 750ms, which causes adiabatic heating from 150μK to $\sim 700\mu$K [2]. To minimize the time spent in the bad background environment, the translation stage starts moving out of the MOT cell with a maximum acceleration of $450\frac{cm}{s^2}$ simultaneously with the ramp of the field gradient. Heating due to the stage acceleration could not be observed. The two-way transport efficiency is $\sim 50\%$, leaving typical one way transport qualities of 75%.

The evaporation starting condition in the BEC cell is roughly $1 - 1.5 \times 10^9$ atoms at around 700μK with a phase space density of 2×10^{-8}, cf. Fig. 3.2.

3.2 Evaporative cooling simulations

After laser cooling and transport of the atom cloud into the BEC cell, evaporative cooling in the compressed magnetic trap further increases the phase space density (PSD) to the phase transition. It is not a priori clear what the best initial cloud parameters in the BEC cell are for large condensates, because the system is described by two parameters (atom number N and temperature T). Ideally, N should be maximum and T minimum, so that the initial phase-space density is large and the collision rate is high. In fact, there is a trade off between these two values: for rather hot clouds the evaporation is not very efficient and many orders of magnitude of phase space density have to be overcome for condensation - but the final BEC atom number scales with the initial atom number before evaporation, which can be large under this condition. On the other hand, the evaporation quality is better for rather cold clouds and the initial phase-space density is closer to the phase transition. However, since one starts out with fewer atoms, it is still possible that the final condensate is smaller. The purpose of this chapter is to address questions regarding the evaporation optimization in the BEC cell by evaporation simulations to extract a guideline for the experiment. In particular, the goals are:

- Compare the evaporation in the quadrupole and TOP trap

---

[2] Since the Molasses temperature is much lower than 150μK, the final temperature in the BEC cell is mainly determined by the size of the cloud after the CMOT stage.

- Determine characteristic profiles of evaporation trajectories
- Extract the typical scaling of N and PSD during evaporation
- Compare the different BEC atom numbers for different initial (N,T) values

The focus of the first part of this chapter is to examine the physical process leading to the evaporation of the hot atoms and to compare the possible implementations. In the second part, the evaporation dynamics are discussed by applying a simple single-step model. In the third part, this model is used to perform simulations for our trap.

3.2.1 Stationary evaporation

The main idea of evaporative cooling is very simple and can be found in many examples in every-day life: if a liquid is very much hotter than its environment, a physical process will take place to compensate for this imbalance. The hottest molecules in the Boltzmann distribution of the liquid will escape, whereas the colder molecules cannot overcome the energy barrier of leaving the surface. Therefore, the average energy per particle leaving the hot liquid is higher than the actual average energy of the particles in the liquid. Consequently, the average energy per particle is lowered and the temperature drops. The bottom line is that the system tries to adjust to the temperature difference by evaporative cooling.

This idea equally applies to a cloud of trapped atoms: the hottest atoms are selectively removed from the trap, while the cold atoms remain unchanged, so that the temperature decreases. Most experimental implementations use a spatially-selective process for evaporation of the hottest atoms, [7, 64–69].

The idea to use evaporative cooling for further increase of the phase-space density was suggested by Hess in 1986, [7]. The most common method is radiative evaporation, which was first proposed by Pritchard in 1989 [70] and later shown experimentally [71, 72]. The basic idea is that atoms are resonantly driven from a trapped to an untrapped state by an EM-field. If the conservative atom cloud trap is formed by the Zeeman shift (magnetic trapping), a spatially selective removal of the atoms can be achieved using a RF-field resonant with transitions between different magnetic substates. This method is very convenient: the trapping potential can remain unchanged and the evaporation surface is a clean shell around the trap center with easily adjustable parameters.

(A) RF-forced evaporation in the dressed state picture

The physics behind the RF-induced transitions in a magnetic trap can be understood in the dressed state picture of the atom and EM-field. Without coupling, the atom and EM-fields decouple and the eigenenergies of the Hamiltonian are an infinite ladder of manifolds separated by $h\nu_{rf}$, where ν_{rf} is the RF frequency of the oscillating magnetic field. For a F=1 atom, each energy manifold consists of three states: $m_F = 1, 0$ (untrapped, $|e>$) and $m_F = -1$ (trapped, $|g>$), where the g_F-factor is -1/2. In this case, many crossings in the energy spectrum versus magnetic field occur Fig. 3.3a).
The EM bias field oscillating at ν_{rf} creates coupling between the two systems with an interaction energy of $\hbar\Omega_R =< e|\hat{\vec{\mu}}_{atom} \cdot \vec{B}_{rf}|g>$. Coupling of the atom to the electric field is negligible, as transitions are dipole forbidden between magnetic sublevels. The magnetic interaction results in off-diagonal elements in the coupled atom-light Hamiltonian, so that the eigenergies are shifted [47]. These shifts are large where the RF-photon energy $h\nu_{rf}$ is resonant with two different Zeeman-levels in the magnetic trap, i.e. at the crossings in the energy spectrum. A brief calculation shows that the shifts cause avoided-crossings between these levels [6], cf. Fig. 3.3b). Note that this situation is analogous to optical transitions, for which the coupling $\hbar\Omega_R = \vec{p}_{atom} \cdot \vec{E}_{rf}$ creates the off-diagonal terms stemming from the induced atomic polarization $\vec{p}_{atom}$.
The atomic motion introduces non-adiabaticity into the problem, which can be addressed in the Landau-Zener formalism [73, 74]. At a single avoided crossing, the atom can be in three different states a,b and c. As the atom moves, the Zeeman-splitting changes and thus the eigenergies of the uncoupled Hamiltonian, while the off-diagonal elements remain the same. Assuming a linear atomic motion, the uncoupled eigenenergies also change linearly far away from the resonance. This is exactly the case of the Landau-Zener formalism. With the atom velocity v_{atom} and magnetic field gradient b, the 3x3 Hamiltonian then reads [75]:

$$i\hbar\frac{d}{dt}\begin{pmatrix} a \\ b \\ c \end{pmatrix} = \begin{pmatrix} \gamma t & -\frac{\hbar\Omega_R}{2\sqrt{2}} & 0 \\ -\frac{\hbar\Omega_R}{2\sqrt{2}} & 0 & -\frac{\hbar\Omega_R}{2\sqrt{2}} \\ 0 & -\frac{\hbar\Omega_R}{2\sqrt{2}} & -\gamma t \end{pmatrix}\begin{pmatrix} a \\ b \\ c \end{pmatrix} \tag{3.1}$$

$$\gamma = \mu_B m_F g_F b v_{atom} \quad , \quad |\hbar\Omega_R|^2 = \frac{1}{4} m_F^2 g_F^2 \mu_B^2 B_{rf}^2 [F(F+1) - m_F(m_F-1)]$$

For $t \rightarrow -\infty$ the atom is in the trapped $m_F = -1$ state. At $t \rightarrow \infty$ the atom is in general in a superposition of all three states. An analytical expression for the transition probability P_{trans} into the two untrapped states can be found

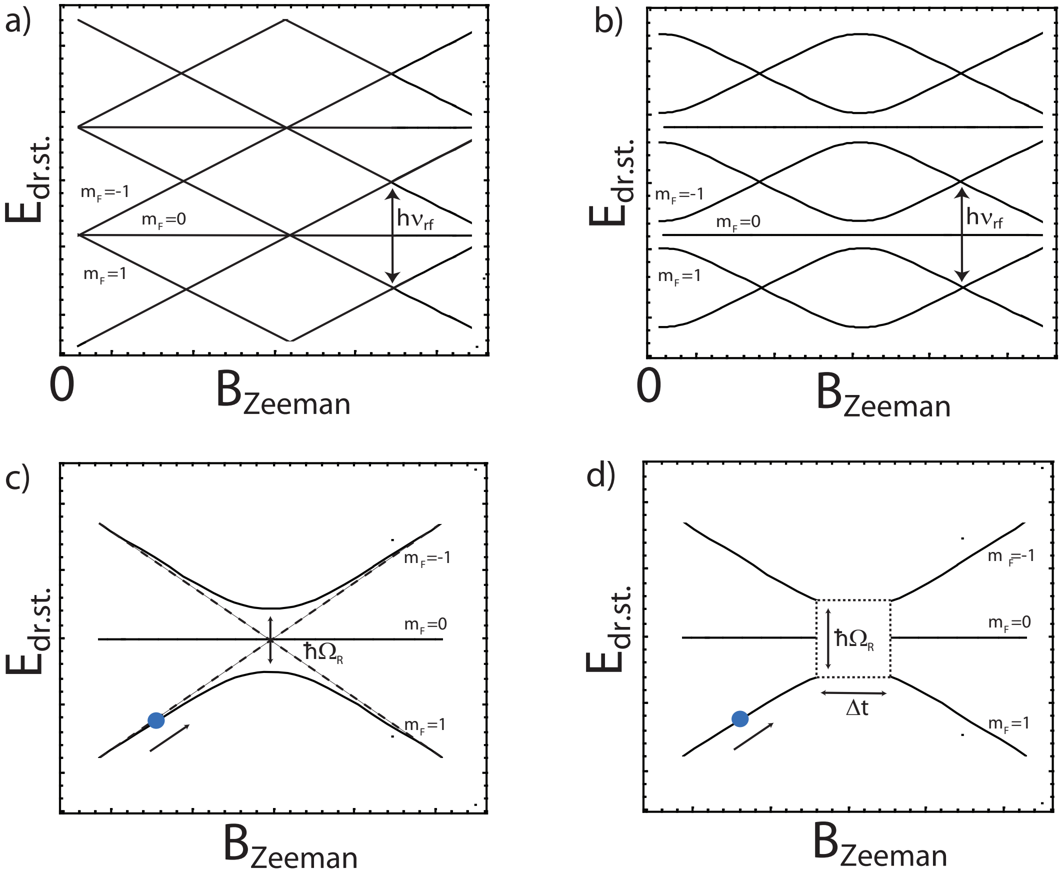

Figure 3.3: Landau-Zener transitions in the RF domain: a) Landau Zener ladder without coupling between rotating RF field and magnetic substates. The energy manifolds are separated by $h\nu_{rf}$. b) Effect of the coupling RF field. Light shifts in the dressed state picture cause avoided crossings where angular momentum is conserved. c) zoom to relevant avoided crossings during RF evaporation. Slow atom movement corresponds to adiabatic transition into the untrapped states, while fast equals the non-adiabatic process and thus finite probability in the trapped state. d) replacement of interaction region by black box using Heisenberg uncertainty principle. If the energy uncertainty is larger than the energy spacing, tunneling into the untrapped state can occur.

by a generalization of confluent hypergeometric functions [73–77]:

$$P_{trans} = 1 - e^{-\frac{\pi}{4}\frac{\hbar|\Omega_R|^2}{\gamma}} \tag{3.2}$$

If the trapped atom is very slow, it follows the avoided-crossing adiabatically and therefore ends up in an untrapped (bare) state. The non-adiabaticity of a fast atom results in a mixing, so that the transition probability is reduced, cf. Fig. 3.3c). Additional insight is gained by using the Heisenberg uncertainty principle: the energy separation at the avoided crossing is given by $\hbar|\Omega_R|$. The physics at the avoided crossing can then be replaced by a black box through which the atoms passes in the time $\hbar|\Omega_R|/\gamma$. The corresponding energy uncertainty is $\gamma/|\Omega_R|$. If the atom is so fast that this energy uncertainty is larger than the avoided crossing energy gap, the atom can tunnel between the dressed states. The atom is then still in the trapped (bare) state and evaporation has not occurred. A significant change in the transition probability is thus expected for $\gamma\sim \hbar|\Omega_R|^2$ and the behavior should be an exponential function of $\frac{\hbar|\Omega_R|^2}{\gamma}$.

(B) Boundaries on RF power

In the magnetic trap only those atoms with sufficiently high energy can reach the regions where the RF-field is resonant (evaporation shell). Hence, the cold atoms remain trapped, while the hottest atoms evaporate - if the Landau-Zener transition probability is large enough so that a clean and sharp evaporation shell is formed around the center of the trap. With Eq. 3.1 and 3.2 and the thermal velocity $v = \sqrt{8k_BT/m}$, this basically sets a lower limit to the RF magnetic field amplitude for the transition probability not to drop considerably[3]:

$$B_{rf}^2 > \frac{\hbar b}{\pi g_F \mu_B\left[F(F+1) - m_F(m_F-1)\right]}\sqrt{\frac{8k_BT}{m}} \tag{3.3}$$

At a typical initial temperature of 400μK and a RF field of 100mG, the transition probability is very close to 1 ($\sim 1 - 1\times10^{-11}$), so that the evaporation surface can be considered very clean[4]. The surface radius itself is determined by the RF frequency. However, the edge of the "RF-knife" is not exactly "sharp": as in the optical regime, the transition is power broadened, which translates into a spatial width Δx of the evaporation surface. This width can

---

[3] For atomic trajectories perpendicular to the equipotential surfaces.

[4] This is also true including realistic atomic trajectories.

be estimated by the spatial width of the avoided-crossing in the dressed-state energy ladder:

$$\Delta x \sim \frac{\hbar\Omega_R}{\mu_B m_F g_F b} \tag{3.4}$$

At the beginning of the evaporation, the width is negligible compared to the radius of the evaporation shell. But at the end of the evaporation the RF-power needs to be reduced, so that the linewidth remains much smaller than the evaporation surface radius and the edge of the RF-knife is still sharp. An estimate of the upper and lower boundaries using Eqs. 3.3 and 3.4 is shown in Fig. 3.4.

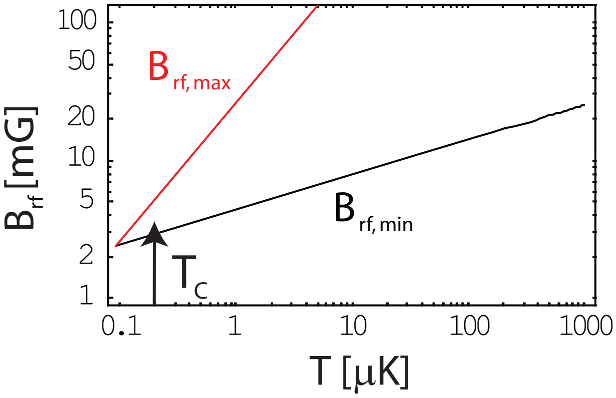

Figure 3.4: Estimate for the constraints on the RF power during evaporation. The upper limit stems from the power broadening of the transition, while the lower boundary originates in the finite transition probability into an untrapped state. The critical temperature from the experiment (cf. Chapter 4.4) is still above the point where the boundaries meet.

(C) Geometry of the evaporation shell

Size and shape of the evaporation shell are determined by the resonance condition between Zeeman-splitting and the RF-field. For the quadrupole trap this results in an ellipsoid around the center, cf. Fig. 3.5a)+b):

$$B_{ax} m_F \mu_B g_F \sqrt{1-(\vec{e}_r\cdot\vec{e}_z)^2}\sqrt{\frac{x^2}{2}+\frac{y^2}{2}+z^2} = h\nu_{rf}, \qquad \vec{e}_r = \frac{\vec{r}}{|\vec{r}|}$$

The dotproduct arises because only the RF amplitude perpendicular to the quantization axis of the magnetic trap field contributes. This leads to holes in

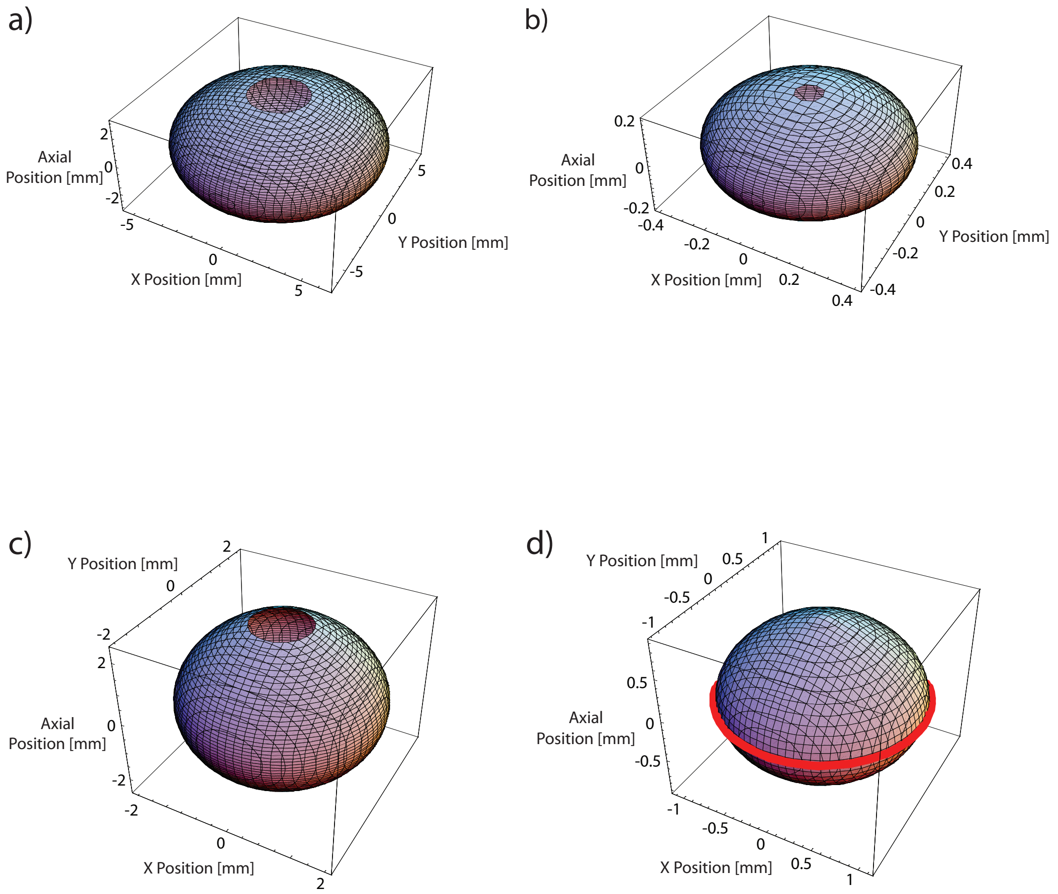

Figure 3.5: RF evaporation surfaces for different traps and parameters. Only the perpendicular RF amplitude to the Zeeman-field can contribute to the transitions leading to the formation of holes around the axial axis. a) quadrupole trap ($B_{ax} = 350$G/cm) with RF at 80MHz and 100mG. The hole is rather large as the atoms are still hot. b) quadrupole trap with RF at 5MHz and 100mG, the situation at the end of the pre-evaporation, cf. Chapter 3.3.2. The hole has shrunk as the atoms are much colder. c) 60G TOP trap with RF at 80MHz and 35mG. The shell is deformed due to the bias field and does not correspond to the equipotential surface any more. d) realistic situation in the experiment with 18G TOP trap and RF at 26MHz and 100mG, cf. Chapter 3.3.2. The red ring corresponds to the trajectory of the rotating magnetic field zero ("circle of death" or CoD).

the evaporation surfaces, cf. Fig. 3.5.

The situation is a little more complicated for the TOP trap due to the presence of the additional rotating bias field. However, the time scale of the atomic motion and thus the crossing of the Landau-Zener transition is much slower than the rotation of the bias field, which is in turn much slower than the Larmor frequency. Therefore, non-adiabaticity due to changing magnetic fields can be excluded. It is hence sufficient to estimate the size of the shell by taking the maximum magnetic field amplitude seen by the atom. Due to the elevated trap bottom, cf. Eq. 2.5, the RF photon energy has to be at least higher than μB_{TOP} so that the evaporation occurs from the outside to the inside when reducing the RF frequency. This leads to a flat football-like evaporation surface, cf. Fig. 3.5c):

$$|B_{QP}(x,y,z) + B_{TOP}(x,y,z)|_{max} m_F \mu g_F \sqrt{1 - (\vec{e}_{x,y,z} \cdot \vec{e}_z)^2} = h\nu_{rf} \tag{3.5}$$

The biggest advantage of RF evaporation is that the evaporation is easily tunable and the trap geometry remains unchanged. An alternative scheme is the "circle of death" evaporation, where atoms are removed by the rotating Majorana hole around the trap center [44]. This procedure is less efficient than the RF scheme, as the evaporation surface is a 1-dimensional ring, whereas the RF-evaporation is on a 2-dimensional shell, cf. Fig. 3.5d).

3.2.2 Evaporation dynamics

It is not sufficient to consider a stationary shell for evaporation, because the RF frequency is ramped down in the experiment to evaporate the atoms efficiently. A model for evaporation therefore needs to capture the dynamics of the ramp-down. The basic assumptions and methods are discussed in this section.

Considerable work on the simulation and optimization of evaporative cooling has already been done by a large number of groups [78–83]. The main problem is that the system is not strictly in thermodynamic equilibrium during the evaporation. The most accurate way would be to consider the phase-space density function directly including the effects of many body losses (background, spin-changing and inelastic three body collisions) and the changing evaporation shell in three dimensions. This can be done by random sampling of the phase space (Monte-Carlo method) [78, 79] or direct particle trajectory simulations [80]. A simplification is to consider a truncated Bose-

Einstein distribution at all times for the density function. This leads to set of coupled differential equations which can be solved in a self-consistent way by a step-wise cutting treatment. The advantage of this method is that three-body losses at the onset of condensation can be taken into account [81–83].
It is in general very tedious to deal with the phase-space density function directly, which can be circumvented by assuming ergodic mixing of the gas. The distribution is then only a function of the total energy and not just the potential energy. In the classical regime, this results again in a set of coupled partial differential equations, which can either be integrated directly or solved by a truncated Boltzmann distribution in a quasi-thermodynamic equilibrium [84, 85]. These models usually do not include three-body losses and energy dependent scattering cross sections, nor the quantum mechanics at the phase transition. But several simulation cross-checks of the classical density function evolution (Boltzmann equation) show that these simplifications are valid at least in the classical regime and match very well with both the experimental results and the Monte-Carlo simulations [84–86].
An even further simplification is the step-wise model, an iterative approach of evaporation and subsequent rethermalization [87, 88]. This model relies purely on the scaling of characteristic parameters, but various loss processes, collision rate enhancement by Feshbach resonances and crossovers to the hydrodynamical regime can still be included via rate constants [89].

(A) Model assumptions and derivation of differential equations

For the simulation of the evaporation dynamics in our setup, a modification of the simple step-wise model is used. The non-equilibrium dynamics are replaced by a repetitive process of cutting the Boltzmann distribution at a cutoff energy, waiting until the gas has rethermalized without forced evaporation and then cutting at a lower energy again. Repeating this procedure many times then yields an interpolation of the changing system parameters during evaporative cooling. This is roughly the case for frequency controlled RF evaporation in both trap types (quadrupole and TOP) as used in our experiment, because the evaporation shell approximately matches the equipotential surface of the trap, so that all atoms above a certain threshold energy are chopped off. In addition, collisions with the background gas introduce a finite lifetime in the trap. The details of the basic assumptions are comparable to those made by Sackett et al. [84]:

- Atom cloud in 3-dim. trapping potential (quadrupole or TOP trap) parametrized by $U(x, y, z) = A_1|x|^{s_1} + A_2|y|^{s_2} + A_3|z|^{s_3}$

- Energy-independent s-wave scattering for elastic collisions $\Gamma_{el} = \bar{n}\sigma_{el}\bar{v}_{th}$, where $\bar{n}$ is the average cloud density, σ_{el} the elastic s-wave collision cross-section for Rb-87 and $\bar{v}_{th}$ the average velocity
- Characterization of system through atom number N and temperature T, background collision rate Γ_{bkg} and "collision ratio" Γ_{el}/Γ_{bkg}
- Ergodic mixing and evaporation on equipotential surfaces of trap
- Piece-wise cutoff at $E_{cut} = \eta k_B T$ followed by rethermalization in τ_{ret} with the truncation parameter η
- Classical statistics (PSD<< 1)
- Incorporation of one-body losses and Majorana losses in quadrupole trap through a temperature dependent loss rate constant
- Neglect two- and three body losses

After a single cut and rethermalization, the atom number and temperature have decreased from N to N' and T to T'. The new atom number is defined by the cutoff integral $\int_0^{\eta k_B T} \rho(E)dE$ of the density function, while the new total energy can be calculated from $\int_0^{\eta k_B T} E\rho(E)dE$. The scaling of the temperature and atom number is then found to be only a function of the truncation parameter η. The scaling of all other relevant system parameters after rethermalization can then also be calculated. The details of the calculation are carried out in [6, 64] and only the main results are quoted.

To determine the rethermalization time after a single cut, it is necessary to evaluate the propagation of a truncated Boltzmann distribution using the Boltzmann equations. This was done by Luiten et al. [85] for different system parameters, and the authors found that after typically 2.7 collisions the distribution is almost in thermodynamic equilibrium. During this time the atom number decreases exponentially due to collisions with the background at a rate Γ_{bkg}. For discrete steps of $\Delta t = \frac{2.7}{\Gamma_{el}}$ this leads to a set of coupled differential

System parameter	Symbol	Scaling X'/X
Atom number	N	ν
Temperature	T	ν^{γ}
Total energy	E=$(\frac{3}{2}+\xi)$Nk_B T	$\nu^{1+\gamma}$
Volume	V$\propto$ T$^{\xi}$	$\nu^{\gamma\xi}$
Density	n=N/V	$\nu^{1-\gamma\xi}$
Phase-space density	PSD$\propto nT^{-3/2}$	$\nu^{1-\gamma(\xi+3/2)}$
Collision rate	$\Gamma_{el} \propto$ nT$^{1/2}$	$\nu^{1-\gamma(\xi-1/2)}$

$$\nu = \frac{\Gamma_{inc}(\xi+3/2,\eta)}{\Gamma(\xi+3/2)} \qquad \gamma = \mathrm{Log}_{\nu}[\frac{\Gamma_{inc}(\xi+5/2,\eta)}{\Gamma_{inc}(\xi+3/2,\eta)(\xi+3/2)}] \qquad \xi = \frac{1}{s_1}+\frac{1}{s_2}+\frac{1}{s_3}$$

$$\Gamma_{inc}(a,\eta) = \int_0^{\eta} x^{a-1}e^{-x}dx \qquad \Gamma(a) = \Gamma_{inc}(a,\infty)$$

Table 3.1: Scaling of the thermodynamic quantities after a single cut and rethermalization as a function of truncation η and trap ξ.

equations under consideration of the scaling from Tab. 3.1[5]:

$$\begin{aligned}
\frac{\dot{N}(t)}{N(t)} &= \frac{\Gamma_{el}(t)}{2.7}[\frac{\Gamma_{inc}(\xi+3/2,\eta(t))}{\Gamma(\xi+3/2)}-1] - \Gamma_{bkg}\frac{\Gamma_{inc}(\xi+3/2,\eta(t))}{\Gamma(\xi+3/2)} \\
\frac{\dot{T}(t)}{T(t)} &= \frac{\Gamma_{el}(t)}{2.7}[\frac{\Gamma_{inc}(\xi+5/2,\eta(t))}{\Gamma_{inc}(\xi+3/2,\eta)\Gamma(\xi+3/2)}-1] \\
\Gamma_{el}(t) &\propto \frac{N(t)}{T(t)^{\xi-1/2}}
\end{aligned} \tag{3.6}$$

(B) Discussion of the differential equations

The scaling of N and T after a cut and rethermalization is only determined by the trap, truncation and collision ratio Γ_{el}/Γ_{bkg}, cf. Eq. 3.6. It is therefore sufficient to characterize the atoms in the trap at any given time during evaporation only by the instantaneous collision ratio and truncation parameter. The relative scaling of all quantities after a single cut and rethermalization can then be expressed as a function of these two values. In that sense, evaporative cooling with arbitrary initial atom numbers, temperatures and evaporation trajectories is fully characterized by the curve (collision ratio$(t), \eta(t))$, where $\eta(t)$ is controlled externally (corresponding to the tunable RF frequency in the experiment). An example is shown in Fig.

---

[5] For a Taylor approximation of small changes in N and T these exact equations match with the approximate ones from [88].

3.6a), where the truncation is held constant/increases over time.

From an experimental point of view, it is relevant to determine regions of collision ratio and η, where either the PSD, density or elastic collision rate are constant during evaporation (”break-even curves”). These implicit functions can be found in the Appendix A.1. The corresponding curves for all three conditions are shown in Fig. 3.6a)+b) for a linear and harmonic trap, which differ considerably from [88], as no Taylor approximation is made. An approximate approach leads to wrong results at very low truncation parameters so that the ”break-even” curves are shifted to the right.

If the evaporation starts above the collision rate curve (highest ”break-even” curve in Fig. 3.6a)+b)), ”run-away evaporation” will occur, i.e. the elastic collision rate will increase making the evaporation very efficient. This is only possible for sufficiently large trap lifetimes. On the other hand, below this threshold the collision rate will decrease and the evaporation time will increase. It is still possible to have increasing densities or PSD in this region, but they will ultimately decrease after sufficiently long time, as indicated by the example trajectory in Fig. 3.6a). The collision ratio break-even curve shows a minimum as a function of η because of two competing effects: for deep truncations (small η) background losses do not play a role any more, since they decrease the total atom number by a very small amount. On the other hand, weak truncations (large η) increase the effect of the background. For the extreme case of starting directly on the collision ratio ”break-even” curve, all right hand sides of Eq. 3.6 become constant for all times and an analytical solution is available showing an exponential behavior with respect to time of all thermodynamic quantities as well as of the cutoff energy $E_{cut}(t)$, Appendix A.1.

(C) Numerical integration and simulation

Obtaining an exact solution requires numerical integration of the differential equations with a step size of $\Delta t = 2.7\tau_{el}$ while taking the background losses into account. The time scale Δt reflects the initial model assumption of repetitive cutting and rethermalization. The external control parameter of the evaporation is the truncation parameter η. The optimum truncation function $\eta(t)$ can be determined by testing all different possible curves and comparing the expected condensate size. A simpler approach was suggested by Hess et al. [7, 64]: instead of global optimization of the evaporation trajectory, a local method is sufficient: at any given time during evaporation, the system has a certain collision ratio with η as the only degree of freedom for the next cut. The best truncation can then be found corresponding to a chosen ”strategy”.

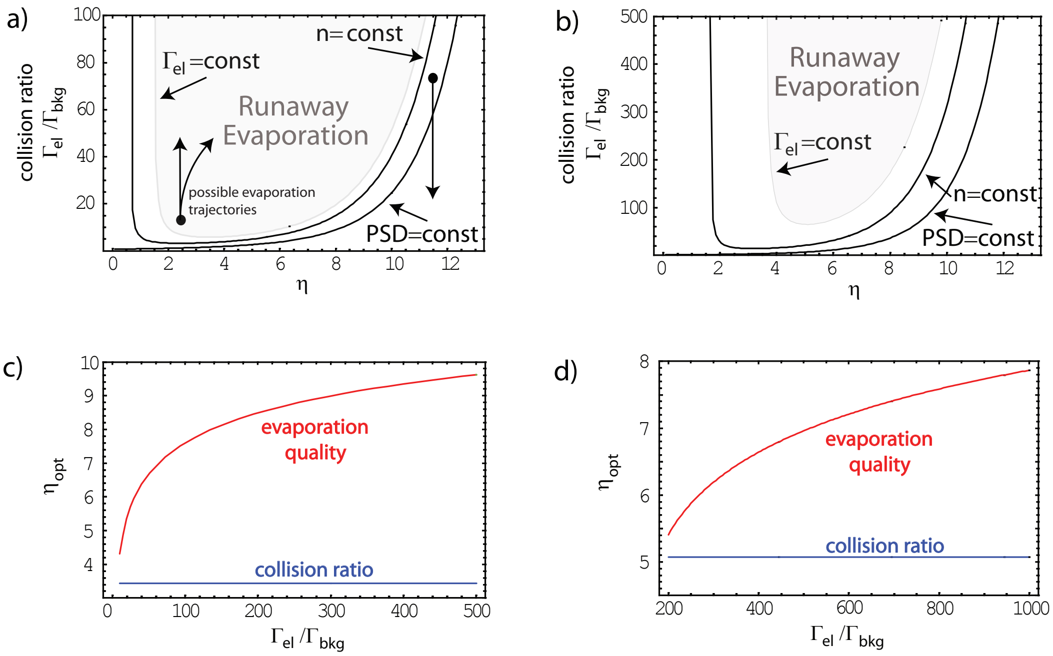

Figure 3.6: a)+b) show the break-even curves for constant Γ_{el}, n and PSD for a linear (a)) and harmonic (b)) trap. The scaling behavior of the thermodynamic parameters is only a function of the trap, the truncation and the collision ratio. The lowest possible collision ratio Γ_{el}/Γ_{bkg} for runaway evaporation is at $\eta\sim 3.5$ for the linear trap and at $\eta\sim 5$ for the harmonic trap. The collision ratio threshold is much lower for a linear trap because the cloud volume decreases much more than in a harmonic trap during cooling. Example trajectories during evaporation are also indicated in a). c)+d) show the optimum η for the two different strategies "Evaporation-Quality" and "Collision-Quality" in the linear (c)) and harmonic (d)) trap. For low collision ratios the best truncation parameter converges to the previously mentioned minimum value for the two different strategies.

- "Evaporation quality" for large BEC: maximize $\frac{\text{Log}[PSD'/PSD]}{-\text{Log}[N'/N]}$
- "Collision quality" for fast BEC: maximize $\frac{\Gamma'_{el}}{\Gamma_{el}}$
- Alternative evaporation time: maximize $\frac{P\dot{S}D}{PSD}$

The "evaporation quality" measures how fast the phase-space density increases as atoms are lost due to the evaporation. This strategy was used for the simulations.

In essence, every strategy yields an optimum η value for each collision ratio in the runaway region, cf. Fig. 3.6c)+d). The collision quality strategy does not show a variation in η for different collision ratios and stays at the minimum of the elastic collision rate break-even curve, while the evaporation quality strategy prefers higher truncations with increasing collision ratio. The reason is that for very high elastic collision rates, rethermalization occurs almost immediately and losses become negligible making it favorable to cut away only the very hottest atoms. These curves are used to perform the integration of Eq. 3.6. The code (Mathematica 6.0) is listed in Appendix A.3. The results are discussed in the next section.

Some extensions of this basic simulation scheme are possible to describe the experimental situation more accurately. For the evaporation in the linear trap, the Majorana losses can be incorporated through a temperature dependence of the trap lifetime in each cutting step. This effect was measured in Chapter 3.3.2 for the trap used in the experiment and compared with the theory. The loading of the atom cloud from the quadrupole to the TOP trap can be predicted by assuming adiabaticity. The details can be found in Appendix A.2.

To increase the evaporation quality, the TOP circle of death can be ramped down simultaneously with the RF evaporation shell radius. Assuming $r_{CoD} = \alpha r_{rf}$ with $r_{CoD} = 2B_{TOP}/b$ and using Eq. 3.5, this gives the condition:

$$r_{rf} = (\frac{h\nu_{cut}}{m_F g_F \mu_B} - B_{TOP})\frac{1}{B_{rad}} \quad \Rightarrow \quad B_{TOP}(\nu_{cut}) = \frac{h}{m_F g_F \mu_B}\nu_{cut}\frac{\alpha}{\alpha+1} \tag{3.7}$$

The trap tightening can be included into the simulation by first performing the cut and the scaling of the parameters and then adiabatically loading the cloud into the stiffer trap. Exact formulas can be found in the Appendix A.2.

One of the main flaws of this step-wise model is that the procedure does not reflect the experimental conditions, since the atom cloud is actually never in equilibrium. But comparisons with Monte-Carlo simulations by Hulet et al. [84] show that both methods match very well. For very fast rethermalization times compared to the total evaporation time scale, the time discretization should be a good approximation. The simulations by Walraven et al. confirm that the assumption of ergodic mixing is valid [85, 90]. In spite of this, deviations might still occur resulting from the assumption of a clean evaporation shell on the equipotential surface of the trap. In addition, the absolute value for the simulated condensate size will not be correct, because three body losses set in at the critical density (n$\sim 10^{14}$cm^{-3}).

3.2.3 Simulation results and experimental guidelines

In this section the evaporative cooling simulation is used to provide a rough guideline for the procedure in the experiment. One of the main problems is whether or not to perform evaporation in the linear trap and if yes, to determine when to switch to the TOP trap so that the condensate is as large as possible. This is a nontrivial problem, because the solution depends on many parameters: initial atom number and temperature of the atoms, the evaporation trajectory of the evaporation in the linear trap or the switch-on value for the TOP bias field. It is thus useful to only study the rough behavior of the system through the simulations and extract the most promising experimental procedure.

(A) TOP loading

To have a guideline of what to expect in the experiment, the evaporation quality ($-\frac{\text{Log}[PSD'/PSD]}{-\text{Log}[N'/N]}$) during evaporation in the quadrupole and different TOP traps (60G, 30G and 10G) is simulated, cf. Fig. 3.7. With decreasing TOP bias field, the evaporation becomes more efficient. This is due to the stiffer harmonic trap increasing the elastic collision rate and thus the collision ratio. Initially, evaporation in the linear trap is most efficient, but for lower temperatures the Majorana losses decrease the lifetime of the cloud, which is modeled through a change in Γ_{bkg}, so that the collision ratio decreases and ultimately drops below the break-even threshold. This causes the crossing of the evaporation quality in the linear and harmonic trap.

The reason why evaporation in the linear case is much better are the scaling laws: for a certain decrease in temperature, the cloud volume shrinks down a lot more than in the harmonic case ($V_{lin} \propto T_{lin}^3$ while $V_{harm} \propto T_{harm}^{3/2}$). The increase of the collision ratio is thus much higher in the linear trap.

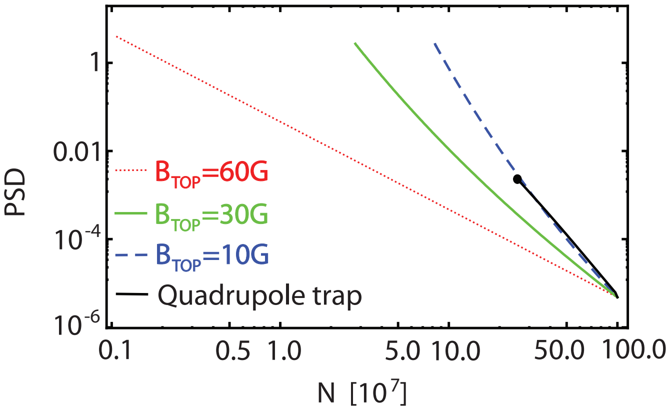

Figure 3.7: Comparison of evaporation quality in linear and harmonic trap. The initial cloud before evaporation has 10^9 atoms at 200μK in the quadrupole trap. Adiabatic loading into the TOP trap is assumed without cloud chopping from the CoD. Majorana losses are taken into account for the quadrupole trap through the measured dependence of the trap lifetime, cf. Chapter 3.3.2. The simulation in the linear quadrupole trap stops at a cloud temperature of T= 30 μK (PSD $\sim 10^{-5}$), because the quadrupole trap lifetimes were only measured at higher temperatures. The evaporation quality corresponds to the slope of the lines.

The loading of the TOP trap is determined by two major effects: evaporation in a very stiff harmonic trap can reach the quality of a linear trap. But for too low bias fields the CoD is much smaller than the size of the cloud, causing considerable chopping. However, while evaporation in the linear trap is superior to shallow TOP traps of large bias fields, this inverts for lower temperatures, because of Majorana losses. Therefore, the optimum strategy is to do some evaporative cooling in the quadrupole trap beyond the point where the cloud just fits into a 60G TOP trap and switch to the TOP trap at some later time with a lower bias field. The procedure for finding this optimum loading point will be discussed in Chapter 3.3.2.

(B) Evaporation trajectories

For typical evaporation trajectories in the experiment, several different possibilities are considered, as illustrated in Fig. 3.8: evaporation in the linear trap and harmonic trap at different bias fields, with and without a simultaneously following CoD. As the behavior of the evaporation trajectory is a function of the initial cloud conditions, a set of typical experimental values is chosen to illustrate the influence.
All trajectories in the quadrupole trap look almost linear with slight curva-

ture downwards. In the break-even situation, cf. Fig. 3.6a), an exponential dependence is expected - but since the initial collision ratio is far away from threshold, the rate constant of the exponential keeps increasing over time causing a straightening. In contrast, the trajectories for TOP evaporation at 60G and 20G are almost pure exponential curves. This is due to the fact that the lowest collision ratio for run-away evaporation is much higher in the harmonic than in the linear trap, cf. Fig. 3.6a)+b). Note that the evaporation time scale in the quadrupole trap is significantly faster ($\sim$ 10s-20s) than in the TOP trap ($\sim$ 60s). Finally, the simulation with a following TOP bias field shows an almost linear behavior again. There are two reasons for this: as the bias field decreases, the trap bottom shifts downwards, which the RF-knife has to follow to maintain the same truncation parameter η. Also, the adiabatic trap stiffening increases the collision ratio, thus making the evaporation more efficient and quicker over time. Therefore, the rate constant of the exponential increases over time and the final curve looks approximately linear.
For evaporation in the linear trap or harmonic trap with a following CoD, a single linear slope seems suitable for the experiment. In the case of the TOP trap at constant bias field, a multi-linear interpolation of maybe two or three different slopes should be appropriate for experimental optimization.

(C) Evaporation quality

The same major cases as before are used to determine typical evaporation qualities in the different trap types, cf. Fig. 3.9. In the quadrupole trap, the evaporation quality is $\sim 3 - 3.5$ for not too long evaporations - a rather high value stemming from the very low collision ratio threshold for runaway evaporation, cf. Fig.3.6a). In the very shallow TOP trap of 60G, this threshold is much higher and the reduced elastic collision rate causes the evaporation quality to drop to ~ 2, while in the much stiffer harmonic trap of 20G values of $\sim 3 - 3.5$ are reached. These numbers reflect again the fact that it is best to start with some evaporation in the quadrupole trap and then load into the TOP trap. Finally, the evaporation in a TOP trap of an initial bias field of 60G and a following CoD shows an evaporation quality of ~ 2. Note that the initial atom numbers are reduced by a factor of 10 compared to the case without the decreasing bias field so that the initial cloud is not even in the runaway regime. Due to the adiabatic trap stiffening, the collision ratio still increases over time and slowly drifts into the runaway regime. If the same starting values are chosen, the evaporation quality in the case of a following CoD would be $\sim 2.5 - 3$. This makes sense, because the value lies in between those of the stationary 60G and 20G case.

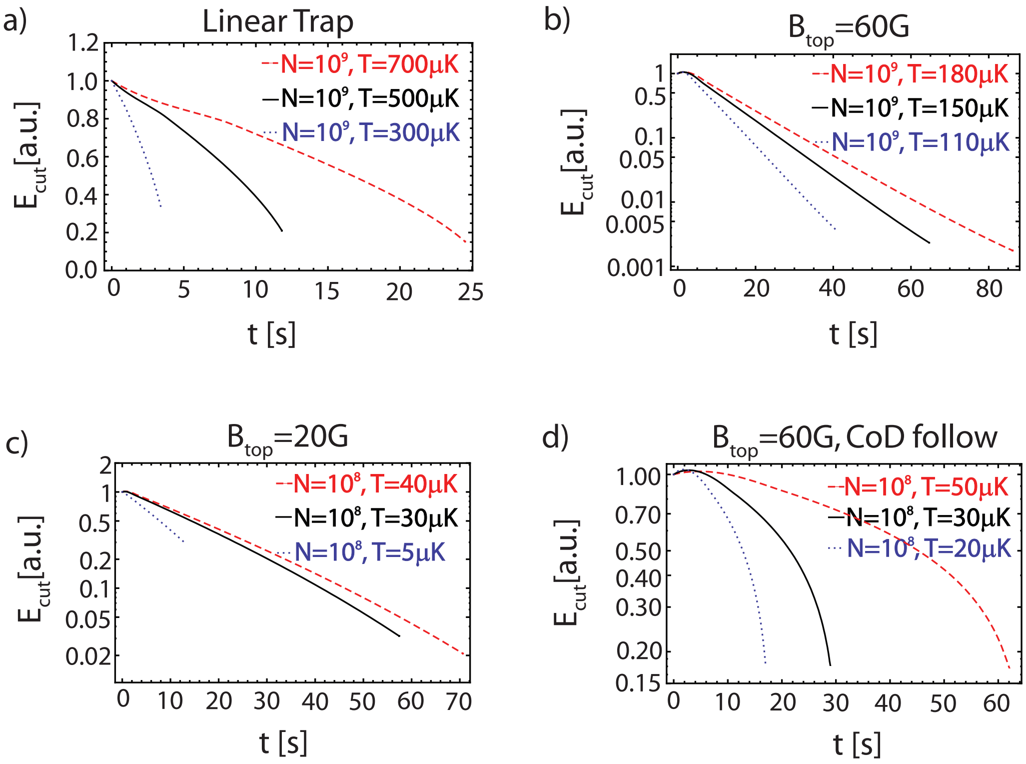

Figure 3.8: Simulation of evaporation trajectories for different traps. To observe the dependence on the initial cloud, multiple temperatures are chosen for each trap according to typical values from the experiment. Note that a) is on a linear scale, while b), c) and d) are on a logarithmic scale. The simulations in all harmonic traps were carried out until the phase transition, while the evaporation in the quadrupole was only done to a temperature of $\sim 5\mu$K, where the Majorana losses are definitely too large to continue. The minimum bias field in d) was 10G. The general trajectory shapes (linear or exponential) do not exhibit a significant dependence on initial cloud parameters.

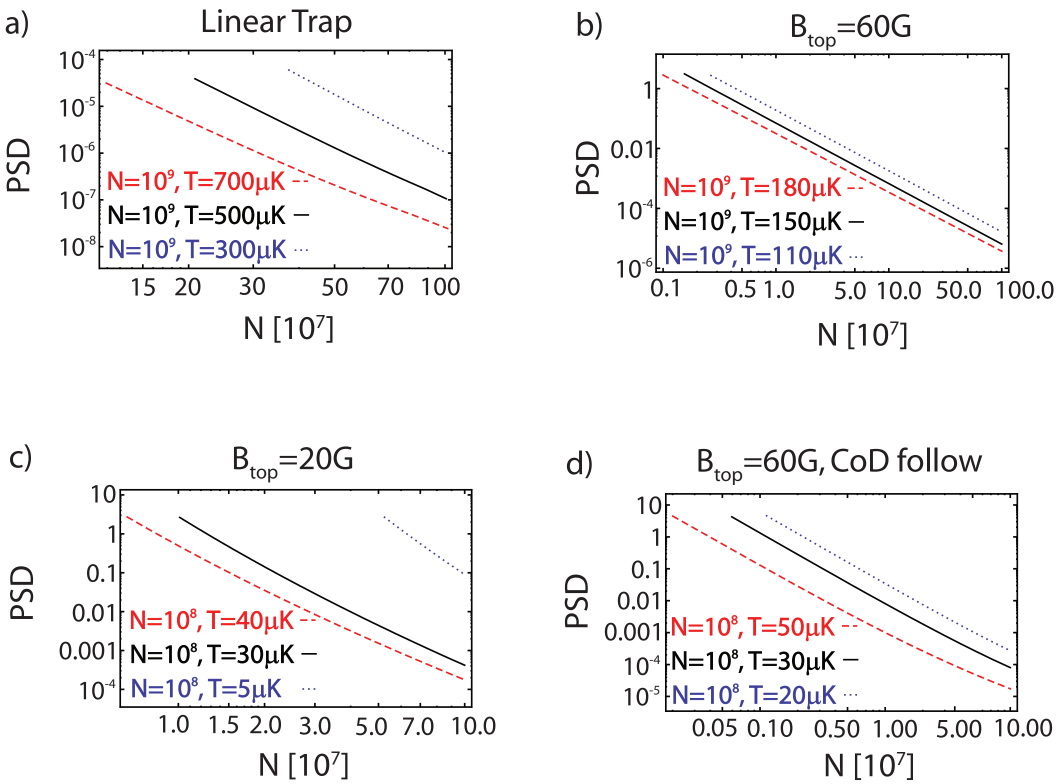

Figure 3.9: Simulation of evaporation quality for different traps. Different temperatures motivated from experimental data are chosen to determine the dependence on the initial trap values (similar to Fig. 3.8). The slopes of the lines correspond to the evaporation quality ($-Log\frac{PSD'}{PSD}/Log\frac{N'}{N}$). They exhibit only a weak dependence on initial cloud values, since they are all nearly parallel for each trap.

(D) Optimum initial (N, T) in BEC cell

The last question to be addressed by simulations are the optimum initial (N, T) values in the BEC cell before evaporation to achieve the largest condensate. This is done by simulating the evaporation for various initial clouds, cf. Fig. 3.10. For each (N, T) pair the evaporation in the quadrupole trap is performed until the temperature is so low that the cloud just fits into the CoD of a 60G bias field TOP trap. (A simulation for the optimum point to load the atom cloud into the TOP trap is omitted for simplicity.) Then the actual evaporation proceeds with a joint CoD/RF ramp until the condensate sets in (PSD~ 1). The TOP loading is assumed to be adiabatic as well as the stiffening of the harmonic trap.

In principle, the BEC machine will have a "working region", which means that atom number and temperature of the initial cloud in the BEC cell are only in a certain area of this 2-dim. parameter space. An example of this working region is shown in Fig. 3.10, where the edge of this area is assumed to be a straight line ($N \propto T$). Obviously, the optimum (N, T) value is then somewhere on this edge. Under this condition, two cases can be identified: if this line is very high in offset, N - rather than T - should be optimized (maximum N). In contrast, for a very low offset, this rule is inverted and it is more promising to start in the lower temperature region with a smaller number of atoms.

The physical explanation is that if the edge is in the upper left area of the parameter space (N, T), the collision ratio is very close to the threshold of run-away evaporation. Hence, the collision ratio does not increase rapidly and the evaporation quality does not increase as the evaporation proceeds. It is therefore better to start out with more atoms, because the evaporation is not much more efficient in the low (N, T) region of the edge of the working region. On the other side, if the edge is in the lower right region of the parameter space (N, T), the collision ratio already starts out far off from threshold causing a rapid increase of the collision ratio and thus an increase of the evaporation quality. It is therefore more useful to start out in the low (N, T) region of the edge to increase this effect, although having lesser atoms initially.

To finally answer the question of what the best point to start out with is, the actual working region of the machine has to be determined experimentally, i.e. what atom numbers and temperatures can be produced in the BEC cell. This will be discussed in the next section.

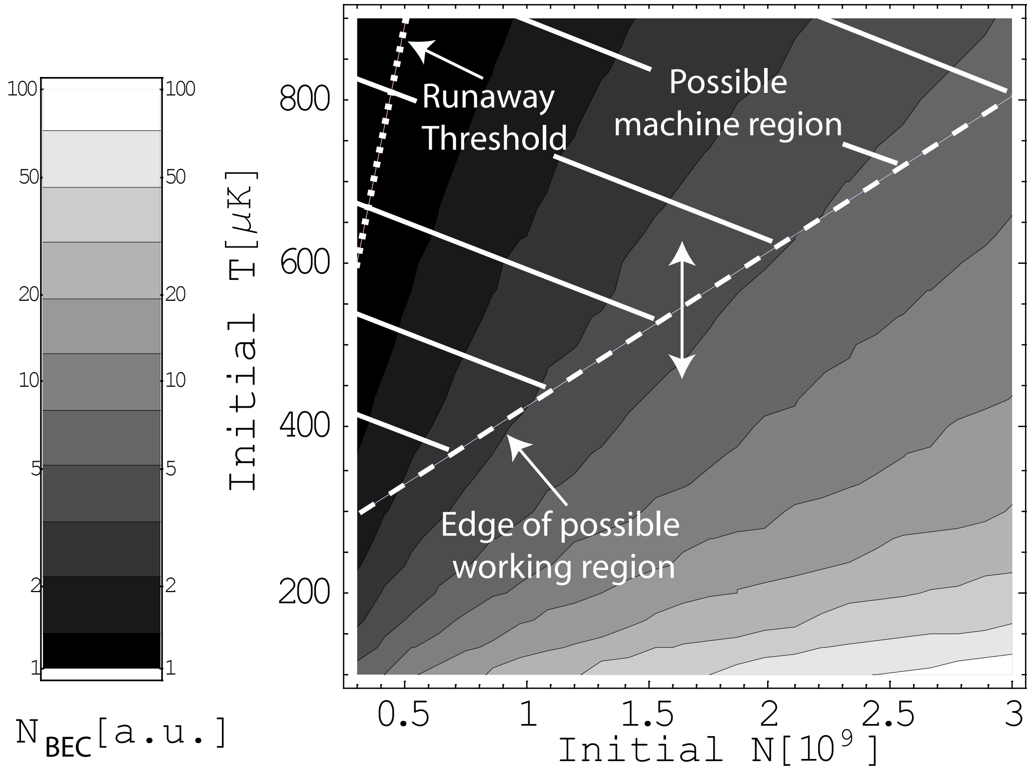

Figure 3.10: Simulation of relative expected BEC atom number for different initial atom numbers and temperatures in the BEC cell before evaporation. A statement of the absolute condensate size from the simulations is inaccurate, because three-body losses are neglected. The whiter the region, the more atoms in the condensate. The marked area shows a possible "working region" of the machine, while the edge is indicated by the dashed line. The dotted line indicates the runaway threshold. As evaporation proceeds, the atom cloud parameters will move on a contour line.

3.3 Optimization of the BEC machine

The main purpose of the evaporation simulations is to provide a guideline for the optimum condensate production in terms of atom number. The experimental optimization protocol is explained in this chapter. In the first section, the experimental determination of the machine working region is discussed to determine the best atom number and temperature to start out with, before evaporative cooling in the BEC cell. In the second section the experimental optimization of the final evaporation sequence is illustrated using both the guidelines from the simulation and experimental data.

3.3.1 Optimization of the atom cloud parameters

Determination of the machine's working region in terms of possible initial (N,T) values in the BEC cell requires all different settings of all parameters for the laser cooling part to be checked. Since there are at least a dozen experimental parameters involved, this seems impossible to accomplish. In addition, it would require the machine to run stable on a very long time scale (several days), which is difficult with our Rb oven.

A simplification is to subdivide the sequence into several temporal steps (MOT loading, compression, cooling, loading into magnetic trap,...). Each block can then be optimized for itself. The parameter space can be reduced this way and the working region can be determined by varying the different blocks. To clarify this idea, consider the following example: since the final temperature in the BEC cell depends on the CMOT size before loading the atoms into the magnetic trap, the (N,T) region can be scanned by varying the cloud diameter. This can be done by changing the atom number of the density-limited CMOT. This general approach was actually first tried in the experiment and was also the guideline for optimizing the sequence described in Chapter 3.1. However, this approach has some disadvantages:

- The optimization time needed in the experiment is very long, because the sequence settings of the different blocks have to be changed in a controlled way and quantitative evaluation of the cloud in the BEC cell is necessary. Hence, the blocks were only optimized according to their temporal order - cross correlations between the blocks are therefore not taken in to account.
- Long-term drifts of the oven on a time scale of several days prevents a straight-forward optimization procedure
- Reoptimization of the laser cooling sequence is necessary after typically one month due to drifts of machine parameters (e.g. MOT mirrors)

The idea for an improved method is to group the various sequence knobs of the laser cooling part not in a temporal order, but into functional groups, among which the correlation is low. From experimental experience it was found that some knobs change the outcome a lot, whereas other knobs are irrelevant to atom number and temperature - they would rather influence other values such as the production time. This results in three different knob categories: rough, intermediate and fine. For optimization, each category is then optimized for itself. An overview of this classification can be found in Tab. 3.2.

Rough	Intermediate	Fine
Rb oven	Molasses detuning ramp	Molasses repump ramp
MOT loading time	Magnetic catch point	Prep. cycling det.
	Molasses duration	CMOT duration
	CMOT field ramp+det.	

Table 3.2: Grouping of sequence parameters for atom cloud production in BEC cell. The distinction stems from experimental experience and is guided by how much the initial atom cloud parameters N and T are changed.

The advantage of this method is that cross correlations between different sequence steps are taken into account, because the sequence is no longer optimized step by step, but treated as a single one. To increase the update time of the iteration, the darkness and size of the atom cloud in the BEC cell are estimated by visual inspection of the raw image, rather than by the evaluation of the data. The optimization time is therefore much lower and the influence of long term drifts can be omitted. Also, if any drifts occur, a reoptimization can be done very quickly.

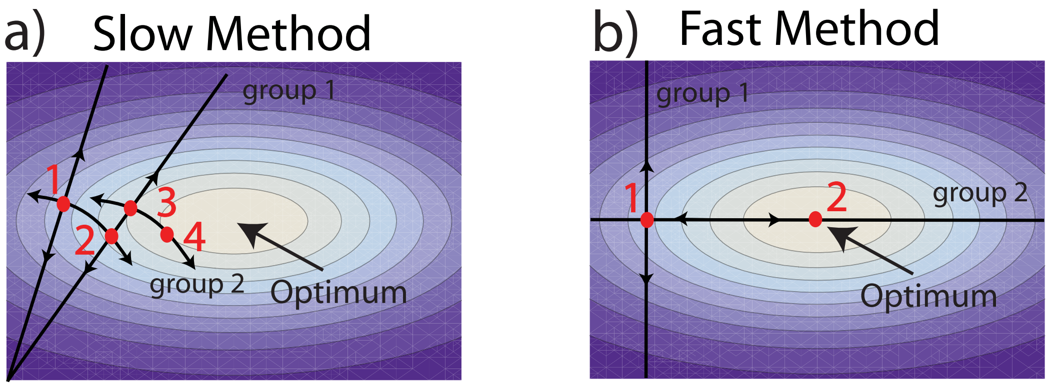

Figure 3.11: Comparison between a correlated grouping (a)) and an uncorrelated grouping (b)). The black lines indicate changes caused by optimized one group while holding the other constant. The optimum point lies in the middle and only two groups are considered here. Many iteration steps are necessary for a correlated grouping, while the optimization time is much faster in the uncorrelated case.

This idea can be illustrated in the case of a two-dimensional parameter-space. An example for a very correlated grouping is shown in Fig. 3.11a):

by varying the first group, the radius to the reference point in the bottom left corner is varied, while changes in the second group correspond to varying the angle. Therefore, when optimizing group by group, many iterations are necessary, because the optimum point of one group depends on the position of the other group (correlated grouping). In contrast, Fig. 3.11b) shows a situation, where the groups are uncorrelated, because the best position of each group is independent of the position of the other group. The amount of iteration steps is therefore much lower.

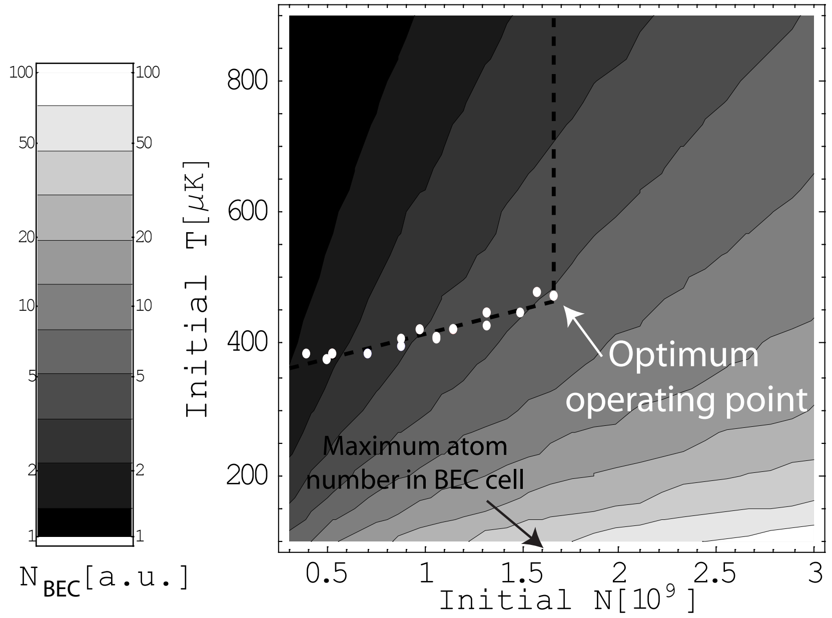

Figure 3.12: Determined edge of the machine working region with expected BEC atom number in relative units for various cloud parameters before evaporation. The dashed line serves as guide to the eye to indicate the working region. The maximum amount of atoms transferable into the BEC cell is 1.6×10^9.

The working region of the machine was determined by setting the two rough knobs (Oven open or closed and MOT loading time) to a certain value and then optimizing first the intermediate and then the fine screws. This was repeated for various positions of the rough knobs. Since the knobs within a group are still correlated, the optimization for the intermediate/fine screws is obtained by a manual random walk in the parameter space[6]. Aside from that,

---

[6] The most important knob in the intermediate group seems to be the molasses detuning ramp.

there is no further guideline. It was found that the optimum settings of the intermediate/fine screws are the same for a broad range of rough screw positions. The manual iteration time can therefore be even more decreased by shortening the MOT loading time to e.g. 1 s. With this method the temperature could be reduced by 50% (compared to the a priori optimization of the laser cooling sequence) in only ~ 30 min while keeping the atom number at 1.6×10^9.

The results for the edge of machine working region are shown in Fig. 3.12. In our case, the machine does not make it into the area where the temperature becomes more important (bottom right). The best operating point is thus given by atom number optimization with N$\sim 1.6 \cdot 10^9$ and T$\sim 450\mu$K. The machine region shows a cutoff in atom number at this point, because this is the maximum amount of atoms transferable into the BEC cell. The sequence for the optimized atom cloud production in the BEC cell is illustrated in Fig. 3.13, which forms the starting point of evaporative cooling. Note that there is no CMOT in this case, as the compression only caused significant heating.

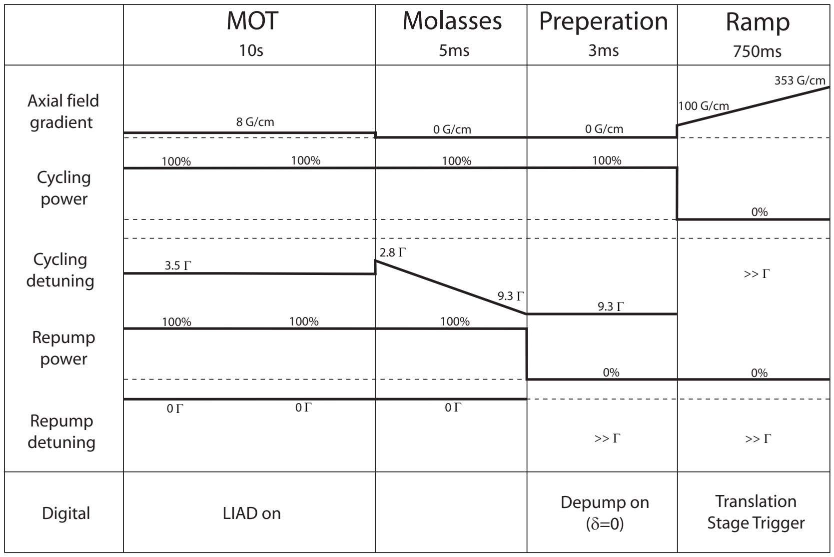

Figure 3.13: Summary of the optimized F=1 atom cloud production sequence. The given values are rough values and require tuning on a monthly basis due to mirror drifts or changing Rb background environment in the MOT cell. The absolute values for the beam intensities are given in Chapter 2.1.2.

3.3.2 Evaporation optimization

In this section the experimental optimization of the evaporation is discussed. The general guideline is to maximize the evaporation quality. It is crucial that the initial atom number (1.6×10^9) and temperature (450 μK) are reproducible during this procedure, since the best evaporation trajectory depends critically on these values. A mismatch of initial (N,T) in the BEC cell will cause falling off the narrow runaway path and condensation will not occur. The full sequence consists of evaporation in the quadrupole trap, loading of the TOP trap and final evaporation in the TOP trap. The details of the optimized evaporation sequence can be found in Fig. 3.14, while quantitative results are summarized in Fig. 3.15.

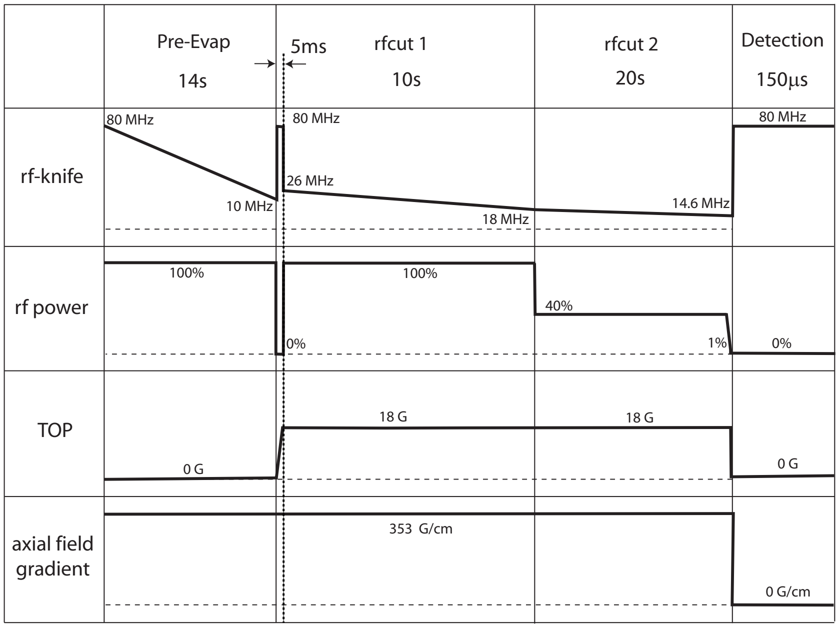

Figure 3.14: Optimized evaporation sequence for initially $\sim 1.6 \cdot 10^9$ F=1 atoms at ~ 450 μK. The Pre-evaporation starts in the quadrupole trap, while rfcut1 and rfcut2 are in a 18 G TOP trap. The TOP switch-on time is 5 ms with a linear ramp of the bias field. The trap bottom in this case is at 12.4 MHz. The critical point is at around 15.0 MHz, while almost pure condensates appear at 14.6 MHz. The two linear evaporation trajectories resemble the expected exponential from simulations, cf. Fig. 3.8

.

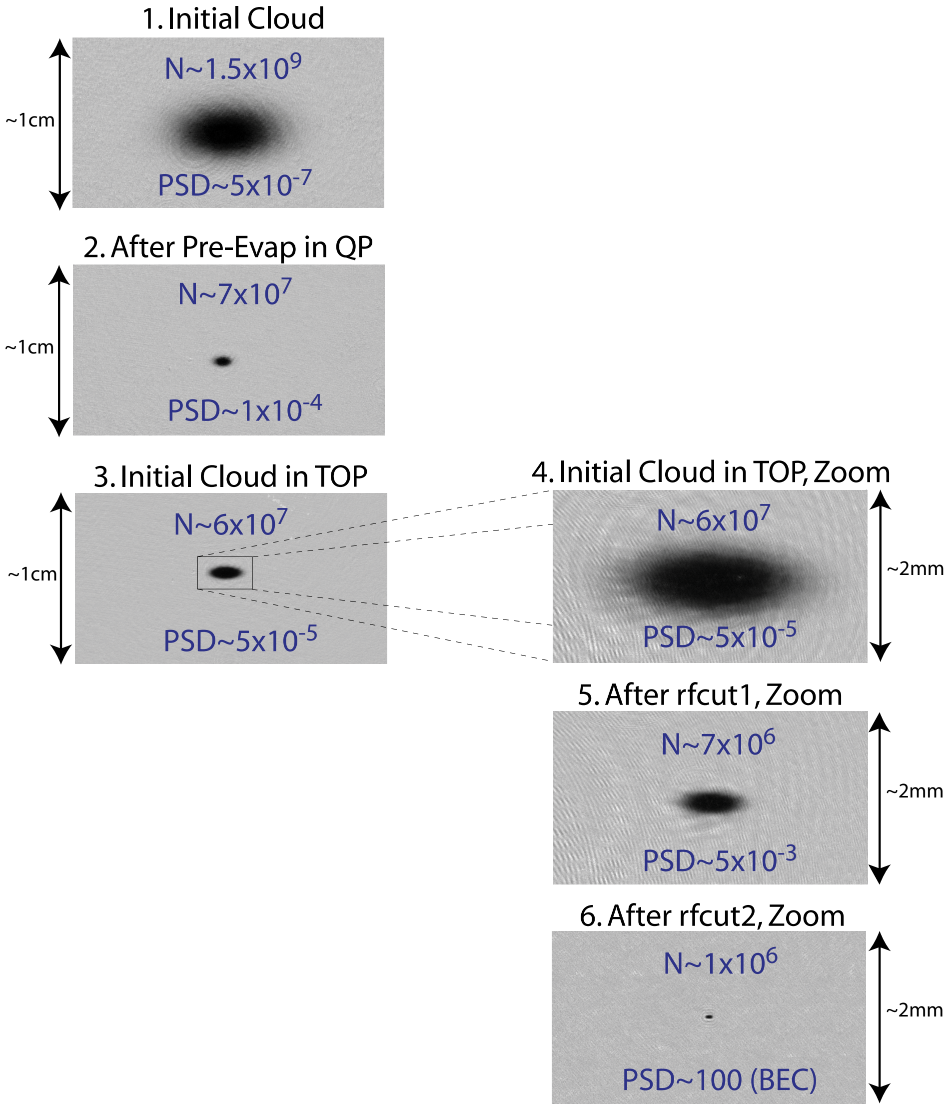

Figure 3.15: Absorption images of atom cloud at different points of the evaporation sequence. The first three pictures have a demagnification of ∼ 1:2, while the imaging system has a ∼ 5:1 zoom for the last three ones. The aspect-ratio in the quadrupole trap (images 1+2) is clearly lower than in the TOP trap (images 3-6). The cloud expands a little upon loading into the harmonic trap (2+3), since the confining potential is shallower. During this transfer, heating causes a loss of a factor of 2 in phase-space density, while almost no atoms are lost.

(A) Slope of evaporation in quadrupole trap

As motivated by the simulations, after some evaporation in the quadrupole trap, the TOP trap is switched on and the final evaporative cooling is performed there. The best trajectory for the linear trap is found by ramping the RF-knife with different slopes to a common reference temperature while noting the atom number. If the slope is too low, background losses become significant. On the other hand, too steep slopes cause chopping of cold atoms and the rethermalization is insufficient. The maximum occurs at a slope of roughly 5MHz/s, cf. Fig. 3.16.

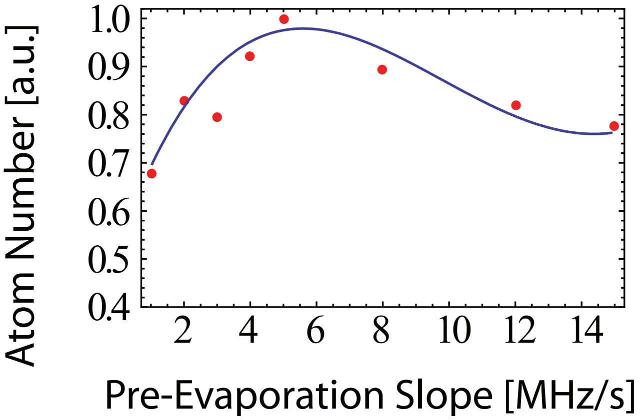

Figure 3.16: Pre-evaporation slope optimization in quadrupole trap. The RF-knife was ramped down with different slopes to a common reference temperature of 200μK, where Majorana losses are still rather low. The optimum slope of $\sim$ 5MHz/s is where the atom number is maximum. The starting cloud parameters before evaporation are $N = 1.6 \times 10^9$ at $T = 450\mu$K. The solid line is a guide to the eye (polynomial)

(B) Effect of Majorana losses

The incorporation of Majorana losses into the simulation requires the measurement of the quadrupole trap lifetime τ_{QP} versus the atom cloud temperature T. This can be estimated in a very crude model developed by Petrich et al. [41]: if an atom passes too close to the trap center, the Larmor precession time scale becomes comparable to the rate of the change of magnetic field direction. The total loss rate is determined by the product of the cloud density $n \propto T^{-3}$, the flux proportional to the atom velocity $v \propto \sqrt{T}$ and the surface of the loss ellipsoid $\propto v$. For large temperatures the lifetime is limited

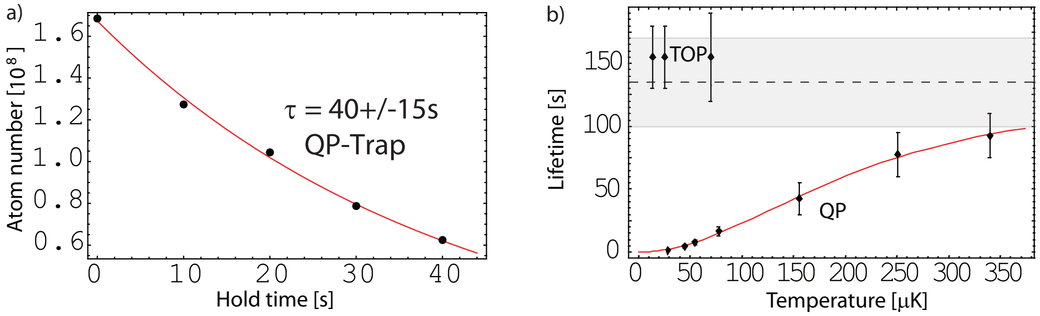

Figure 3.17: Atoms in the quadrupole trap. a) Typical data set for the determination of the lifetime at a certain temperature in the quadrupole trap via an exponential fit. b) Results of the quadrupole trap lifetime for multiple cloud temperatures. The error bars stem from the exponential fit to the atom number decay for different hold times. The red solid curve is the theory fit to the data from Eq. 3.8, while the gray region indicates the predicted range of the limiting background losses from the fit.

to τ_{bkg} by background collisions. The total loss rate is given by:

$$\frac{1}{\tau_{QP}(T)} = \frac{1}{\tau_{bkg}} + \frac{1}{\beta T^2} \tag{3.8}$$

Results of the trap lifetime measurements are shown in Fig.3.17a)+b). A fit of the theory to the data then yields:

$$\tau_{bkg} = (135 \pm 35)\ s \qquad \beta = (0.003 \pm 0.001)\ s/(\mu K)^2$$

For comparison, very cold clouds are loaded into the TOP trap and the lifetime is again determined, cf. Fig.3.17b). These lifetimes match the predicted QP background lifetime from the Majorana losses fit within the error bars.

(C) Evaporation duration in the quadrupole trap and TOP loading

The optimum evaporation time in the quadrupole trap is the most fragile parameter of the sequence, because it depends strongly on the cloud parameters. If the cloud is for instance too cold, Majorana losses can kill the cloud away, while the CoD can chop off many atoms if the temperature is too high. The longer the evaporation in the quadrupole trap is at a given slope, the lower the cloud temperature with which the TOP trap is loaded will be. The bias field at which the TOP trap is turned on should be so low that the cloud just barely fits in (mode matching). In essence, the minimum TOP bias field is a function of the cloud temperature in the quadrupole trap. To measure this, the initial cloud in the BEC cell is evaporated to a certain temperature (5 MHz/s) and then the TOP trap is turned on at various bias fields. The optimum bias field for a certain cloud temperature is then given by the point, where the relative number of atoms caught in the TOP trap saturates, cf. Fig. 3.18a)+b). A theoretical estimate of this dependence is possible by assuming that the CoD radius ($r_{CoD} = 2B_{TOP}/b$) should be at least twice the 1/e radius of the atom cloud after an adiabatic transfer into the TOP trap. Here b is the axial field gradient of the quadrupole trap. With the trap parameters $\alpha_{lin}(b)$ and $\alpha_{harm}(b, B_{TOP})$ defined in Appendix. A.2 one finds:

$$B_{TOP}(T_{QP}) = b^{4/3} \left(\frac{3}{2\pi}\right)^{4/9} \frac{\left[\alpha_{lin}(b)\alpha_{harm}\left(b, 60\ G\right)\right]^{2/9}}{(60\ G)^{1/3}} T_{QP} \tag{3.9}$$

After loading the TOP trap at a certain temperature of the atom cloud, a combined RF/CoD evaporation ($r_{rf} = r_{CoD}$) is performed. The optimum TOP loading point is found by comparing evaporation sequences with different evaporation times in the quadrupole trap to a common reference point chosen to be at a later point in the overall evaporation sequence. A 15G TOP trap is suitable as a reference point[7].

In the experiment we chose different durations for the evaporation in the quadrupole trap at constant slope, switched on the TOP at the corresponding optimum bias field and finally evaporated down linearly to the reference point. The parameter to maximize is then the evaporation quality ($\frac{\mathrm{Log}[PSD'/PSD]}{-\mathrm{Log}[N'/N]}$) by comparing the cloud at the reference point to the intial cloud before evaporation, cf. Fig. 3.18c). Over a long range of evaporation times in the quadrupole trap, the evaporation quality does not vary much. But at 14.5 s, the quality drops and kinks down at 15.5 s. Since the evaporation in the linear trap is much faster than in the harmonic trap, an evaporation time of 14 s in the quadrupole trap is used. After this time the temperature is $\sim 75\ \mu$K, which corresponds to an intitial TOP field of 18 G for mode matching, cf. Fig. 3.18b).

The optimum slope of 1 G/s for the employed evaporation of this measurement in the harmonic TOP trap is determined by maximizing the evaporation quality for different slopes in the TOP trap, cf. Fig.3.18d). The data does not exhibit the expected maximum, because the bias field cannot be ramped slower than 1 G/s (TOP coils get too hot).

To examine the time scale during which the offset field should be ramped up to minimize losses, the atom number in the harmonic trap is measured for

---

[7] As discussed later, lower values would lead to a decrease in the TOP lifetime.

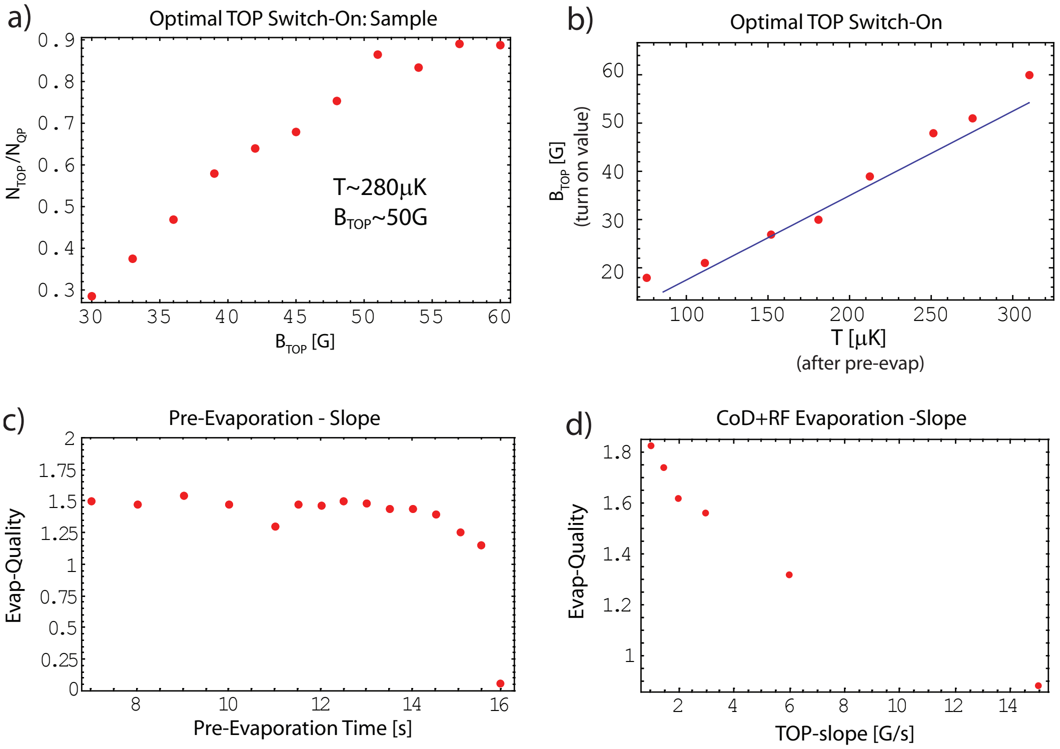

Figure 3.18: TOP loading optimization: a) Sample measurement of the relative amount of atoms transferrable into the TOP trap from a 280 μK atom cloud after evaporation in the quadrupole trap. The lowest bias field where the cloud barely fits into the harmonic trap in this case is ~ 50 G. b) Minimum offset field for different cloud temperatures in the quadrupole trap. The blue solid curve is the theoretical prediction from Eq. 3.9. c) Measurement defining the evaporation time in the quadrupole trap: for different TOP loading points the cloud is always evaporated further to a common reference point. The decrease for 14.5-16 s stems from Majorana losses, making 14 s the optimum value. d) Measurement to find the best slope for CoD+RF evaporation in the TOP trap. The evaporation quality of 1.8 matches roughly the prediction from the simulations in Fig. 3.9.

linear ramps from 1 ms to 20 ms. A dependence could not be observed. Since the coil current overshoot is negligible for at least 5 ms, this value is used in the experiment.

(D) RF/CoD evaporation in the TOP trap

With the atom cloud in the 18 G TOP trap, the further strategy is to simultaneously ramp the RF and CoD to a certain minimum offset field followed by a final RF evaporation step at a constant offset field. The final ramp-down bias field is determined by the lifetime of the TOP trap as a function of B_{TOP}. This can be measured by evaporating the atom cloud down to different bias fields and observing the lifetime after the ramp-down via different holding times and an exponential fit, cf. Fig. 3.19.
For bias fields above 18 G, a dependence of the TOP lifetime on the bias field cannot be observed and the lifetime matches the expected background lifetime from Fig. 3.17b). Below this value, the curve kinks down. Hence, it seems to be best not to decrease the bias field below 18 G[8]. Therefore, evaporative cooling with a following CoD is not necessary, since the TOP trap is already loaded at 18 G. The final evaporation is done at a constant TOP trap of 18 G with only the RF-knife.

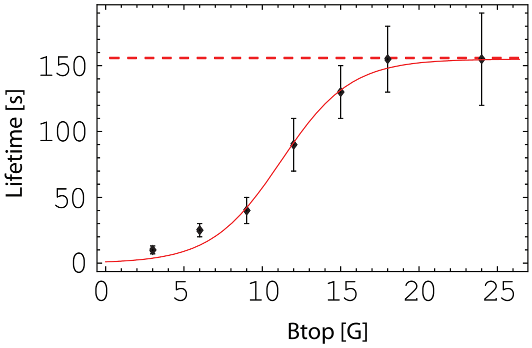

Figure 3.19: Losses in TOP trap. The data is obtained by cooling down to different bias fields and then measuring the lifetime. The lower the offset field, the lower the cloud temperature. The lifetime errors stem from the exponential fits. The red fit function (solid line) is taken from Eq. 3.10. A background lifetime of 155s (dashed line) was assumed, which gives a fit constant of $\alpha = 0.45$.

---

[8] However, a lower bias field might still be better, since two effects contribute when lowering the offset field: the lifetime decreases but the elastic collision rate increases due to the stiffer trap, such that BEC can be reached faster.

(E) Losses in the TOP trap

Losses at low bias-fields have been extensively investigated by Ensher et al. [44]. There are several possible loss mechanisms, such as three-body losses, CoD evaporation losses or even magnetic field noise in the kHz range inducing spin flips into untrapped states for very low bias fields. These effects can all be ruled out in our case, as discussed in [44].
Another possibility, which is also discussed in [44], are Landau-Zener transitions. If this is true, they might occur when the atom passes near the "avoided crossing" formed by the average potential of the trapped and untrapped state at the center. Neglecting the temperature dependence, the transition probability should scale exponentially with the offset energy $\Delta E_{off} = \mu B_{TOP}$ of the harmonic potential in the center according to Eq. 3.2. With a proportionality factor α, this leaves for the lifetime:

$$\tau_{loss}(B_{TOP}) = \left[e^{-\alpha B_{TOP}} + \frac{1}{\tau_{bkg}} \right]^{-1} \tag{3.10}$$

The fit in Fig. 3.19b) seems to confirm the presence of Landau-Zener losses. However, it is still necessary to look at absolute values to see if the energy scales match at all, because the fit only makes a statement about relative numbers: the energy gap between the trapped and untrapped state in the center should roughly match the Heisenberg energy uncertainty associated with the atom velocity v when passing near the center. This leaves the condition [44]:

$$B_{TOP}\mu \sim \frac{\hbar B_{rad} v}{B_{TOP}}$$

At $B_{TOP} \sim 10$ G the data indicates a considerable reduction of the lifetime. However, at this point the tunneling energy is about 6 orders of magnitude lower than the energy gap [9]. So it seems that Landau-Zener losses are not the dominant mechanism, although the fit seems to support this idea.

An extension of this model is offered here: not only is the loss rate prediction 6 orders of magnitude too low, it also seems inadequate to consider the average potential, because Landau-Zener transitions are a result of the potential a particle sees over time. An atom off the axial symmetry axis of the trap sees an oscillating instantaneous potential, Eq. 2.3. In that sense, the atom passes many times through an "avoided crossing" formed by the trapped and untrapped magnetic substates while the bias field rotates. Landau-Zener

---

[9] The time spent in the avoided crossing is approximately 10ms

transitions then might occur.
The energy separation of this "avoided crossing" is given by $\Delta E_{min} \sim \mu B_{min}$, where B_{min} is the minimum magnetic field amplitude seen by an atom at a certain position in the trap while the bias field is rotating. An illustration is shown in Fig. 3.20, which describes the situation for different atom positions in the x-y plane of the rotating field.

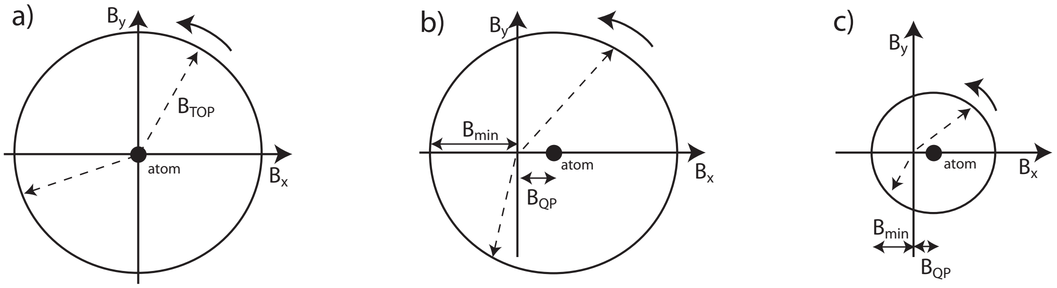

Figure 3.20: Magnetic field as seen by an atom at different positions in the x-y plane. a) Atom in the trap center. The bias field rotates around the atom in a circle of radius B_{TOP}. b)+c) Average distance r of atom to symmetry axis in units of the quadrupole field (B_{QP}) for large (b)) and small (c)) bias fields. Because the RF-knife is ramped simultaneously along the CoD in the experiment, $B_{QP}/B_{TOP} \approx$ const during evaporation (i.e. $r/r_{CoD} \approx$ const)

In general, the scaling of the losses with B_{TOP} depends on the different positions of the atoms in the trap all seeing different minimum energy separations ΔE. For simplification, the atoms are now assumed to be at a certain average relative distance r/r_{CoD} from the axial symmetry axis (z-direction) in the x-y plane. For the experimental data, this relative distance is approximately constant over the range of different bias fields, because the rf-knife was ramped simultaneously along the CoD radius and the truncation parameter η is roughly constant (η relates the average potential energy of the atoms to the trap depth) [10]. Under this condition, the average minimum magnetic field the atoms see is proportional to B_{TOP}, i.e. to the trap offset energy E_{off} in the center. The scaling of the trap lifetime is then given by Eq. 3.10.
The actual transition probability is higher than in the case of the average potential, because the time spent in the avoided crossing region is much shorter (0.01...0.1 ms depending on how large the amplitude of the oscillating potential seen by the atom is). This leaves for the transition probability roughly

---

[10] The relative distance is only constant if the trap stiffening is neglected. However, the modulation on the width of the cloud profile is negligible, cf. Appendix A.2.

$10^{-4}...10^{-3}$ per cycle ($\sim 10^{-6}$ for the average potential). Since the atom passes 10000/s through the "avoided crossing" ($\omega_{TOP} = 10$ kHz), the overall loss rate is approximately 1...10 s^{-1}. This corresponds to lifetimes of 0.1-1 s, which is much lower than the measured lifetime of 30 s at a bias field of 10 G. However, the predicted lifetime in this model is definitely longer due to the low amplitude of the oscillating potential seen by the atoms (compared to E_{off}) and the 3-dim. trajectories of the atoms (the atoms are mostly in the trap center, where the loss rate is lower).

Unlike the average potential, the instantaneous potential predicts a scale, which is much closer to the lifetime measurement in the TOP trap and gives an explanation for Eq. 3.10 as a good fit function. But further investigation is necessary to confirm this model. One example is to measure the lifetime in the TOP trap at a constant bias field at different temperatures. If the model is correct, the lifetime should increase for lower temperatures (limited by the background lifetime), because the atoms are closer to the axial symmetry axis, where the loss rate is smaller.

(F) RF evaporation in the TOP trap

The trajectory for the RF-evaporation in the 18 G TOP trap is determined by scanning different slopes, cf. Fig. 3.21. The initial RF evaporation surface and the CoD match for $\nu = 26$ MHz, Eq. 3.7. The steepest slope of 0.8 MHz/s was chosen, where the evaporation quality saturates at around 2-2.25. Since the evaporation trajectory simulations show a nearly exponential behavior for a stationary offset field (cf. Fig. 3.8), two linear ramps are used. After experimental determination of the RF value for the phase transition, the first linear ramp (rfcut1) is extended to a few MHz above this point. For the final evaporation step (rfcut2), both time and final RF value are varied while maximizing the condensate size with the inverted aspect-ratio at typical TOFs of 15 ms. Instead of evaluating the images, only the cloud darkness was observed. After rfcut1, the cloud temperature is ~ 10 μK. As demonstrated in Fig. 3.4, the RF-power needs to be decreased in the final evaporation step. This was optimized by trying different power values for rfcut2 and observing the condensate size. An additional rapid ramp-down at the onset of the phase-transition increased the atom number even more. This finally gives the optimized evaporation sequence from Fig. 3.14.

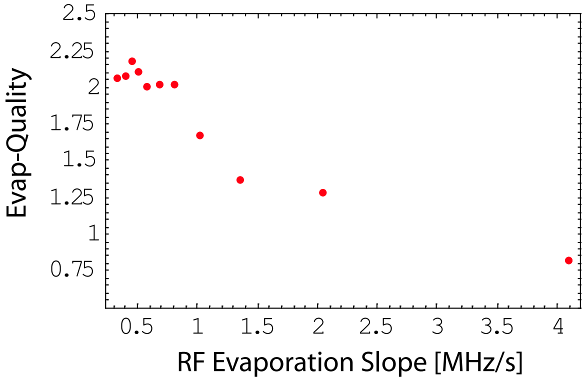

Figure 3.21: Optimization of RF-knife slope in rfcut1. The saturated evaporation quality of 2-2.25 is a little lower than the simulations, cf. Fig. 3.9, since the starting values are worse in the experiment. To minimize the production time, a slope of 0.8 MHz/s was chosen.

Chapter 4

Bose-Einstein Condensate characterization

A dilute gas Bose-Einstein Condensate displays remarkable experimental signatures, such as the thermal phase transition: as the phase-space density approaches one, the particle wave functions start to overlap and quantum mechanical effects have to be considered. The atom cloud then consists of two components: a condensate parabola (cf. Chapter 4.1) and a thermal Gaussian. As the temperature is decreased below T_c, this parabola appears and increases in height, while the Gaussian background decreases (more atoms in condensate fraction). For very low temperatures, the Gaussian background component is no longer visible and only the parabola remains indicating the presence of an almost pure condensate.
A second signature is the anisotropic condensate expansion: instead of a thermal expansion to a round shape for large TOFs after release of the cloud from the trap, a rapid expansion along the stiff axis occurs. This causes the initial aspect-ratio in the anisotropic trap to invert after large TOFs. This is caused by the hydrodynamic behavior of the condensate and the "quantum pressure" stored in the interaction energy before the trap is switched off.

The first condensate was achieved at 5:55am on 14th July, 2007 after a full week of non-stop operation of the machine. The data obtained on this day is shown in Fig. 4.1a) and Fig. 4.1b), clearly showing the phase transition and anisotropic expansion.

In the first section of this chapter the theory for the BEC characterization is explained as well as the extraction of the condensate parameters from the absorption images, while the second section briefly discusses the measurement of the trap frequencies of the TOP trap. This is then used in the next two parts to quantitatively compare the data from the experiment with the theory predictions of the anisotropic expansion and phase transition of the

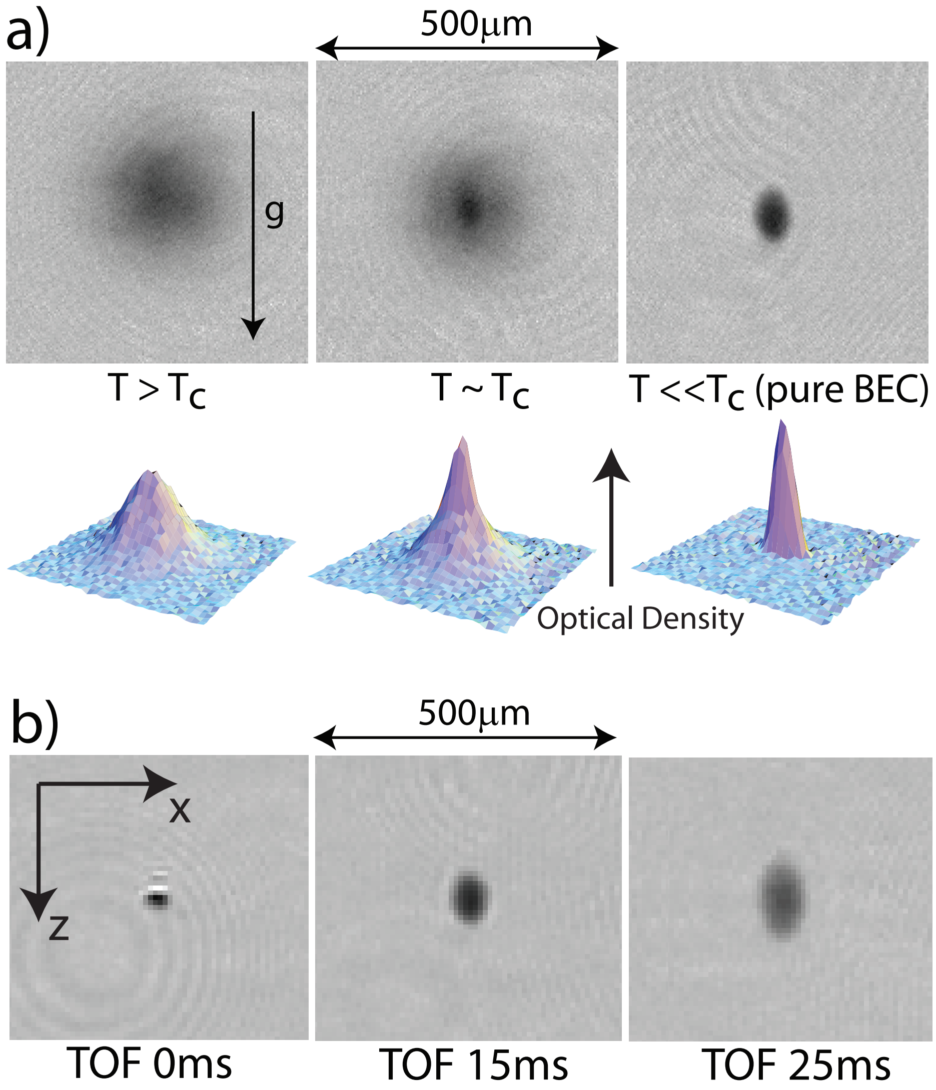

Figure 4.1: Images of first BEC. The imaging plane is in the x-z plane of the lab coordinates (gravity along z-axis). a) Observation of phase transition in the velocity distribution with a TOF of 15 ms after release from the trap. As the temperature is lowered (lower RF frequencies), the condensate emerges from the center of the thermal Gaussian distribution. Far below the critical temperature $T_c = 200$ nK, the thermal part has disappeared and an almost pure condensate of 1.5×10^5 atoms remains (after sequence optimization the condensate size could be increased to $\sim 1.0 \times 10^6$). b) Anisotropic expansion of almost pure condensate (with pixel-averaging of raw data). The inversion of the aspect-ratio is clearly visible. The trap frequencies are $\omega_{ax} = 2\pi \times (96.4 \pm 0.1)$ Hz and $\omega_{rad} = 2\pi \times (34.2 \pm 0.1)$ Hz in this case.

condensate. In the fourth section the details for the evaluation of the condensate atom number are discussed. The machine performance is characterized in the last section by measuring the reproducibility of the condensate atom number and the position stability.

4.1 Condensate theory

(A) Non-interacting model

For a non-interacting cloud of bosons in a harmonic trap, the Hamiltonian of the system can easily be diagonalized and yields for the eigenstates the usual energy ladder spectrum:

$$U(x,y,z) = \frac{1}{2}m\omega_x^2x^2 + \frac{1}{2}m\omega_y^2y^2 + \frac{1}{2}m\omega_z^2z^2, \qquad \epsilon_{\vec{k}} = \sum_{j=x,y,z} \hbar\omega_j(n_j + 1/2)$$

The occupation is governed by the Bose-Einstein statistics, where $\bar{n}_{\vec{k}}$ is the average probability of an atom to be in the energy state $\epsilon_{\vec{k}}$ and $\vec{k}$ is the quantum number for the different trap states.

$$\bar{n}_{\vec{k}} = \frac{1}{e^{(\epsilon_{\vec{k}}-\mu)/k_BT} - 1}$$

In the grand-canonical ensemble of constant temperature T and chemical potential μ, the other thermodynamic quantities, such as total energy E and atom number N, are given by a normalization condition. For non-interacting systems, the chemical potential is never larger than the ground-state energy ϵ_0. For decreasing temperature, the pole in the occupation statistics at $\epsilon = \mu$ shifts towards the ground-state energy. At the critical point where $\mu = \epsilon_0$, the number of atoms in the ground state N_0 suddenly increases on a macroscopic scale and a condensate forms, while the remaining atoms in the excited states form a thermal background[1].

Under this condition, the condensed fraction exhibits the typical scaling of a second order phase-transition, with $\frac{N_0}{N}$ as order parameter and a critical exponent of 3 ($\bar{\omega}^3 = \omega_x\omega_y\omega_z$)[91]:

$$\frac{N_0}{N} = 1 - \left(\frac{T}{T_c}\right)^3, \text{where} \quad T_c = \frac{\hbar\bar{\omega}}{k_B}\left(\frac{N}{\zeta_3(1)}\right)^{1/3} \text{and} \quad \zeta_n(z) = \sum_{j=1}^{\infty}\frac{z^j}{j^n} \tag{4.1}$$

---

[1] Instead of only the atoms in the ground state, the entire atom cloud is often said to be the condensate.

The condition of a macroscopic population of the ground state can be rewritten into the phase-space density criterion mentioned in the introduction:

$$n\lambda_{dB}^3 = \zeta_{3/2}(1) \sim 2.612$$

(B) Interaction effects

The experimentally observed density profile of the thermal background in an ultracold atomic gas is estimated correctly in this simple ideal gas model. But both size and shape of the condensate part are completely inadequate, as discussed in [92]. The reason is the shift of the ground-state energy due to atomic interactions, which become more significant the denser the cloud gets. For typical critical temperatures of ~ 100 nK, the atom-atom interactions are dominated by elastic s-wave scattering. Because of the diluteness of the weakly interacting system[2], the complicated many-body correlations can be replaced by scattering of two particles with a contact potential of $g\delta(x)$ with the coupling constant $g = \frac{4\pi\hbar^2}{m}a$. This leads to a "mean-field potential" seen by the atoms, so that the many particle wave function $\psi(x_1, ..., x_N)$ can be approximated by a direct product of single-particle functions as in the case of a non-interacting Bose gas. Since a macroscopic phase is present in a condensate allowing for coherence to build up on the length scale of the cloud, a macroscopic wave function $\psi(\vec{r})$ can be introduced. This leaves the celebrated time-independent Gross-Pitaevskii (GP) equation. The derivation details can be found for example in [91]:

$$\left[-\frac{\hbar^2}{2m}\Delta + V(\vec{r}) + gN|\psi(\vec{r})|^2\right]\psi(\vec{r}) = \mu\psi(\vec{r}) \tag{4.2}$$

(C) Thomas-Fermi approximation

The ground-state of this Hamiltonian for the condensate can be obtained analytically in the Thomas-Fermi (TF) approximation, [91]: the kinetic energy scale is given by the trap $E_{kin} \sim N_0\hbar\omega$. On the other hand, the interaction energy scale is dominated by the local density and interaction strength $E_{int} \sim gN_0n \approx \frac{4\pi\hbar^2}{m}N_0^2\frac{a}{a_{osc}^3}$, where the harmonic oscillator length $a_{osc} = \sqrt{\hbar/m\omega}$ defines the length scale of the ground state in the harmonic trap.

$$\frac{E_{kin}}{E_{int}} \sim \frac{4\pi a_{osc}}{Na} \tag{4.3}$$

---

[2] This means low quantum depletion into other states apart from the non-interacting ground state

Typical experimental values are $a = 10$ nm, $a_{osc} = 10$ μm and N$\sim 10^5 - 10^7$, so that the scales differ by 2-4 orders of magnitude. This allows to neglect the kinetic energy in the GP equation,. The chemical potential is then much larger than the energy scale of the trap ($\mu >> \hbar\omega$), and quantum pressure builds up in the trap. Under this condition, an analytical solution for the density distribution $n_{cond}(\vec{r})$ is available.

$$n_{cond}(\vec{r}) = \begin{cases} \frac{1}{g}\left(\mu - U(\vec{r})\right) & \text{if } U(\vec{r}) < \mu, \\ 0 & \text{else} \end{cases}$$

In the harmonic trap the distribution is a 3-dim. inverted "Thomas-Fermi parabola", which is chopped off on a discrete shell shaped as an ellipsoid characterized by the Thomas-Fermi radii $R_{x,y,z}$. For a given trap and condensate size, the other thermodynamic quantities can be calculated, cf. [92]:

$$\mu = \frac{1}{2}m\omega_j^2 R_j^2, \qquad N = \frac{\omega_j^5 R_j^5 m^2}{15\hbar^2\omega^2 a}, \qquad n_{cond}(0) = \frac{\mu m}{4\pi\hbar^2 a} \tag{4.4}$$

To obtain the full cloud profile at finite temperatures, the non-condensate fraction needs to be included, [93]. The GP equation cannot be used in this situation, as it assumes no excitations. However, the density distribution can be estimated by a sum of a thermal Gaussian and a 3-dim. TF parabola.

$$n(\vec{r}) = a_{gauss} e^{-\left(\frac{x^2}{2\sigma_x^2} + \frac{y^2}{2\sigma_y^2} + \frac{z^2}{2\sigma_z^2}\right)} + a_{TF}\left(1 - (\frac{x^2}{R_x^2} + \frac{y^2}{R_y^2} + \frac{z^2}{R_z^2})\right) \tag{4.5}$$

This approach breaks down directly at the critical point, where large scale phase fluctuations and quasi-condensates form [94, 95]. Since the interacting system still has the same order parameter and critical exponent as in the ideal gas case, the scaling at the critical point remains unchanged. But the critical temperature is shifted to lower values by the interactions and many body effects, which increases with condensate size. In addition, the finite atom number can also decrease T_c, if the condensates are very small. These two effects are given by [91, 92]:

$$\frac{\delta T_{c,int}}{T_c} = -1.33\frac{a}{a_{osc}}N^{1/6}, \qquad \frac{\delta T_{c,fin}}{T_c} = -0.73\frac{(\omega_x + \omega_y + \omega_z)/3}{\omega}N^{-1/3} \tag{4.6}$$

For typical trap frequencies of (10...100) × 2π Hz in the experiment and condensates of $N_0\sim 10^6$, the shift of the critical temperature due to interactions is about 5%, while the finite size effect is $< 1\%$.

(D) Anisotropic expansion

The TF approximation cannot be used directly to describe the anisotropic condensate expansion after release from the trap, because the "quantum pressure" immediately translates into kinetic energy and Eq. 4.3 is no longer valid. The solution to this problem is motivated by examining the expansion of a classical gas in the hydrodynamic regime for a time dependent trap, which can be written as a time-dependent transformation of the atom cloud diameter. This idea can then be used for the time dependent GP equation by applying both a unitary and a gauge transformation on the many body wave-function. The time dependence of the kinetic part of the Hamiltonian is then hidden in the potential energy and interaction energy term. Under this condition, a TF approximation is valid. For a harmonic trap that is switched off at t=0, this leads to an expansion of the TF parabola with $R_{TF,x,y,z}(t) = R_{TF,x,y,z}(0)\lambda_{x,y,z}(t)$, where the scaling parameters $\lambda_{x,y,z}$ evolve as [96–98]:

$$\ddot{\lambda}_j(t) = \frac{\omega_j^2}{\lambda_j(t)\lambda_x(t)\lambda_y(t)\lambda_z(t)}, \qquad \lambda_j(0) = 1 \quad \text{and} \quad \dot{\lambda}_j(0) = 0 \tag{4.7}$$

In the case of an anharmonic trap with two different frequencies ω_1 and ω_2, an expansion in ω_1/ω_2 leads to an analytic solution. For a TOP trap with $\omega_x = \omega_y = \omega_{rad}$ and $\omega_z = \omega_{ax}$, this leaves to lowest order [98]:

$$\begin{aligned} \lambda_{ax}(t) &= \sqrt{1 + (\omega_{ax}t)^2} \qquad (4.8) \\ \lambda_{rad}(t) &= 1 + 1/8\left(\omega_{ax}t\text{Arctan}(\omega_{ax}t) - \text{Log}\sqrt{1 - (\omega_{ax}t)^2}\right) \end{aligned}$$

While the analytic solution accurately describes the situation in Ioffe-Pritchard traps with $\omega_1 << \omega_2$, the aspect-ratio in a TOP trap is only $2\sqrt{2}$, which causes the analytic solution to be inaccurate for large enough TOFs. This problem can be overcome by transforming Eq. 4.7 into a first order system and performing a numerical integration. The algorithm is shown in Appendix B.1. The results are shown in Fig. 4.2a)+b)

(E) Extraction of cloud parameters from velocity distributions

The bimodal clouds are observed with typical TOFs of 15ms after release of the trap to increase the resolution. The thermal Gaussian and TF parabola from Eq. 4.5 are assumed to expand independently. Hence, the density distribution is still the same up to increased TF radii and Gaussian widths ($\sigma_x(t) \approx \frac{k_B T}{m}t$, cf. Chapter 2.5.2). Since the bimodal clouds are imaged along the y-axis (lab coordinates), the optical density profile is obtained after

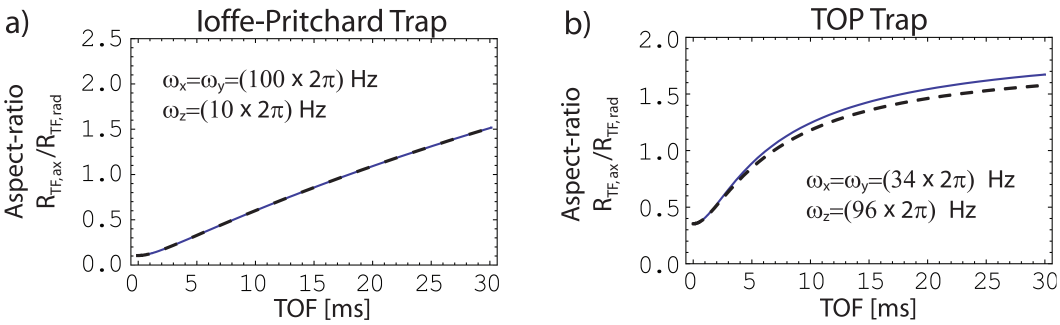

Figure 4.2: Comparison of exact numerical integration (solid line) and analytical solution (dashed line) of Eq. 4.7 for the anisotropic expansion of condensates in different traps. a) Ioffe-Pritchard trap with an initial aspect-ratio of 10 (cigar-shaped). b) TOP trap with a pancake-like condensate at the beginning. The aspect-ratio is $2\sqrt{2}$ in this case. The low aspect-ratio in the TOP case causes significant deviation of the analytic solution in the high TOF region, while both calculations match well in the strongly anisotropic Ioffe-Pritchard trap.

a one-dimensional integration of Eq. 4.5. Including a possible background offset, this leaves nine free parameters.

$$n_{2d}(\vec{r}) \quad = \quad a_0 + a_G e^{-\frac{(x-x_0)^2}{2\sigma_x(t)^2} - \frac{(y-y_0)^2}{2\sigma_y(t)^2}} + a_{TF}\sqrt{1 - \frac{(x-x_0)^2}{R_x(t)^2} + \frac{(y-y_0)^2}{R_y(t)^2}}^{3} \tag{4.9}$$

The cloud parameters are found by fitting this function to the optical density distribution of the experimental data. The atom number of the thermal background is obtained from integration of the Gaussian fit and the atom number calibration, cf. Chapter 2.5.2. In contrast, the condensate atom number and chemical potential are inferred from the expanded TF-radii: with the numerical integration of Eq. 4.7, the initial TF-radii can be calculated from the expanded radii. These are then used to extract the condensate atom number and chemical potential via Eq. 4.4. The temperature of the bimodal cloud is obtained from the expansion behavior of the Gaussian widths.

4.2 Trap frequencies

Quantitative characterization of the condensate requires the measurement of the trap frequencies in the TOP trap. The basic idea is to give the BEC a kick along one trap axis and to observe the motion. This can be realized by suddenly adding a magnetic offset field in one direction, which shifts the trap minimum. As very strong fields would be necessary to resolve the spatial oscillation directly (~ 1 G), the trap is switched off after some oscillation time and the cloud position is observed at a large TOF, which corresponds to a measurement of the velocity of the cloud.

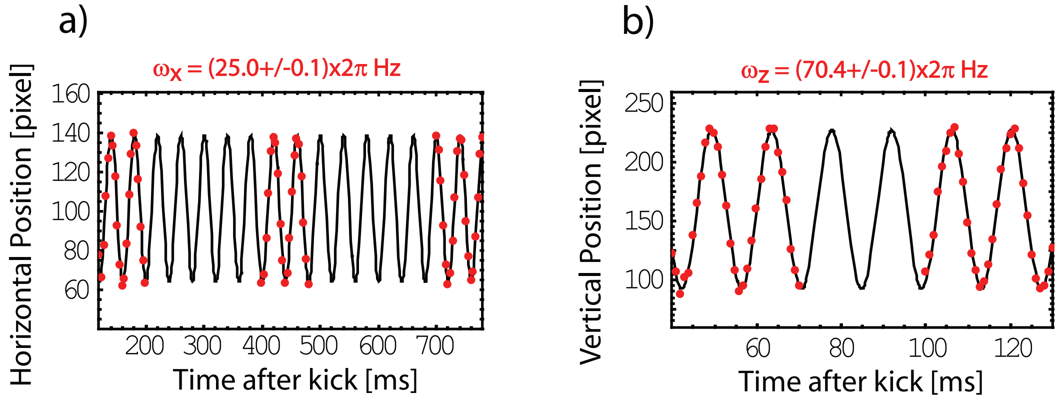

Figure 4.3: Measurement of trap frequencies in the radial direction (horizontal x) and the axial direction (vertical z). The trap bottom was shifted by an additional magnetic offset field of ~ 100 mG for 1 ms (switch-on time < 500 μs) causing the condensate to oscillate along the direction of the magnetic shift field. After a variable hold time, a TOF of 21 ms was used to observe the velocity oscillation after holding the cloud for a variable time in the trap. The aspect-ratio inferred from the trap frequencies $(2.81 \pm 0.01)$is slightly lower than $\sqrt{8}$, because the rotating bias field has an eccentricity of $3 - 5\%$.

A sinusoidal fit is applied to the data to extract the trap frequency. Two full oscillation periods are measured at different times to establish the long-term behavior. Since the imaging beam is along the x-axis, only the vertical trap frequency ω_z and horizontal trap frequency ω_x could be measured, cf. Fig. 4.3a)+b).

$$\omega_x = (25.0 \pm 0.1) \times 2\pi \text{ Hz}, \qquad \omega_z = (70.4 \pm 0.1) \times 2\pi \text{ Hz}$$

Simulations of the bias field profile (Chapter 2.3) predict trap frequencies of $\omega_{x,th} = 26.6 \times 2\pi$ Hz and $\omega_{z,th} = 75.3 \times 2\pi$ Hz at a current of 2.4 A. A possible reason for the deviation could be a possible eccentricity ϵ of the rotating bias field. This would lead to a shift of the trap aspect-ratio in the z-x direction [44]. A numerical calculation shows that our aspect-ratio corresponds to an eccentricity of ~ 1.03. This was roughly confirmed by directly measuring the currents flowing through the two pairs of Helmholtz coils, which differed by $\sim 5\%$.

4.3 Anisotropic expansion

To observe the anisotropic expansion, almost pure condensates are made, released from the trap and observed at different TOFs. A random order of TOFs was picked to prevent systematic errors of the TF radii. Since the imaging is from the side (horizontal), the condensate falls out of the field of view for TOFs larger than 20 ms, so that the objective lens height had to be adjusted. During this procedure, the atom number drifted to lower values, so that the data is divided into two groups (low TOFs: 1-20 ms and high TOFs: 20-27 ms). Every TOF is measured five times to estimate the statistical errors. The results of the aspect-ratio and absolute TF-radii of both axes (axial and radial) are shown in Fig. 4.4a)-c) along with the theoretical fits from Eq. 4.7.

The data for the aspect-ratio agrees very well with the prediction. The free parameter of the fit function is the intial aspect-ratio, which gives a value of $0.96\sqrt{8}$, where $\sqrt{8}$ is the theoretical aspect-ratio of the TOP trap for a perfectly round bias field rotation. There are two possible reasons for this deviation:

- Due to the eccentricity of the trap, the real aspect-ratio is decreased by about 0.5%, cf. Chapter 4.2
- Since the detection time is 150 μs, the vertical cloud profile smears out. This leads to an increased TF radius in the axial direction. Simulations show that this effect is $\sim 1\%$

The data for the absolute TF-radii also agree well with the prediction on both axes. In both data sets for the low TOF section there seems to be a slight systematic downwards trend with increasing TOF compared to the fit. This is not the case for the high TOF region. It is possible that there is still some blurring or diffraction occuring.

4.4 Phase Transition

To measure the critical behavior of the order parameter N_0/N of the phase transition (ratio of condensate fraction to total atom number of cloud), the final rf-knife value in rfcut2, cf. Fig. 3.14, is varied between 15.3 MHz (thermal) and 14.5 MHz (almost pure condensate). After the evaporation sequence the trap is immediatly switched off and the cloud is observed after 15 ms TOF. The theoretical prediction is given by Eq. 4.1. The atom number of the thermal background is obtained by integration of the Gaussian fit function

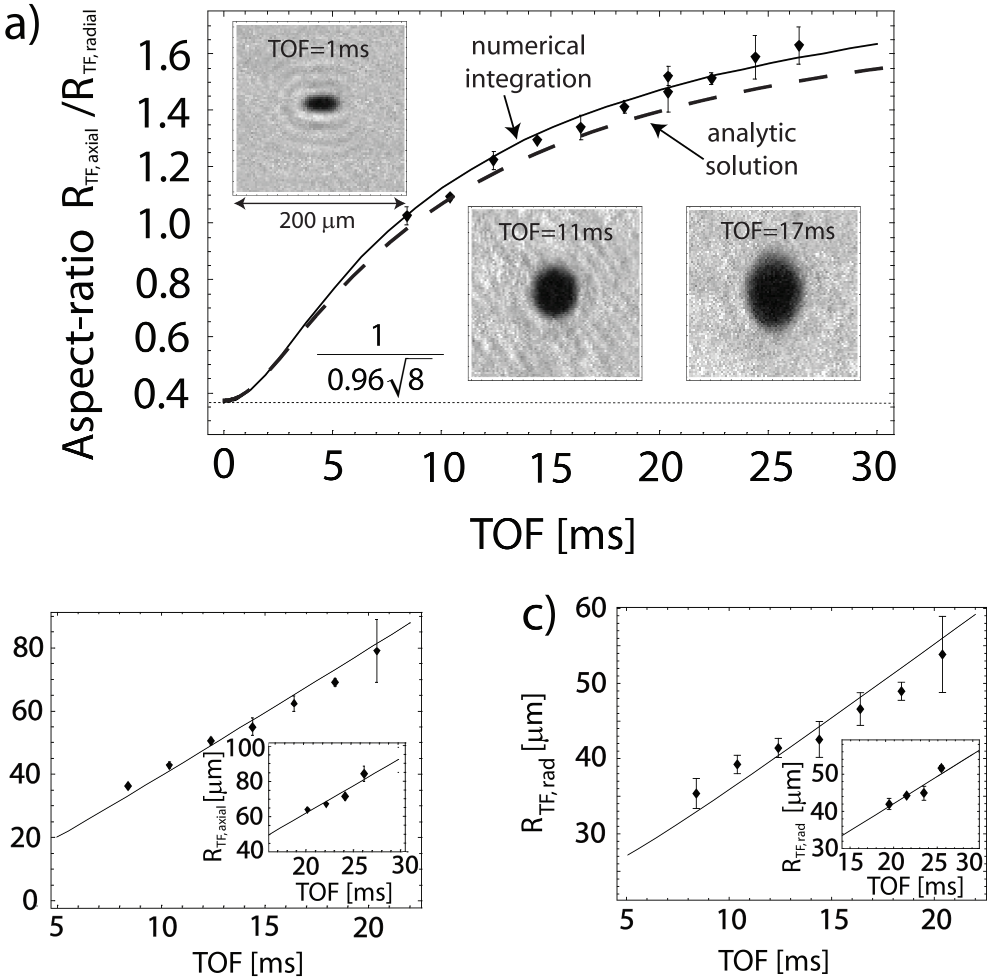

Figure 4.4: Anisotropic condensate expansion. a) shows the aspect-ratio, while b) and c) illustrate the absolute TF-radii on the vertical and horizontal axes. The error bars stem from multiple measurements in random order to prevent systematic errors. The TF-radii cannot be measured accurately for TOFs smaller than 10 ms because of diffraction around the condensate. This causes interference fringes in images. The data for the absolute TF radii are divided into a low and high TOF region, because the condensate atom number drifted to lower values while adjusting the objective lens position (imaging from the side). This separation is not necessary for the aspect-ratio, because they are atom number independent. The fit functions to the data are obtained from integration of Eq. 4.7. For comparison, the prediction obtained from the analytic functions of Eq. 4.8 are shown (dashed line). The fit parameter for the aspect-ratio data is the initial aspect-ratio, which gives $0.96\sqrt{8}$. For the absolute TF radii, the initial TF radius is the free fit parameter (atom number dependent).

to the bimodal distribution, while the condensate atom number number is extracted from the TF radii. To omit the atom number dependence of the critical temperature of each data point, the order parameter is not plotted versus T, but versus $T_{rel} = T/T_c(N)$, where $T_c(N)$ includes the finite size and interaction corrections to the critical temperature, Eq. 4.6. The fit function is then $1 - (\frac{T_{rel}}{T_{c,rel}})^3$, where $T_{c,rel}$ is 1 in theory, cf. Fig. 4.5b).

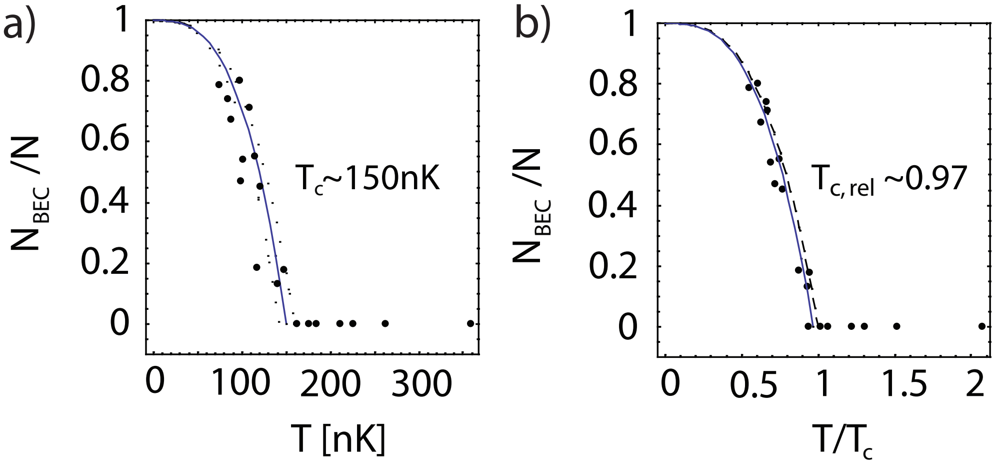

Figure 4.5: Phase transition from thermal cloud to a Bose-Einstein condensate. a) Critical behavior of order parameter N_0/N. The data is plotted versus $T/T_c(N)$ to omit the atom number dependence of each data point. The fit function is $1-(\frac{T_{rel}}{T_{c,rel}})^3$, which gives $T_{c,rel} = 0.97$ in this case (solid line). The dashed curve corresponds to the theoretical prediction of $T_{c,rel} = 0.97$. b) Raw data indicating $T_c\sim$ 150nK by fitting $1 - (\frac{T}{T_c})^3$.

The data agrees very well with the theory and the fit gives $T_{c,rel} = 0.97$. The statistical error is estimated to be $\sim 10\%$ from the data scattering. The temperature determination has an overall systematic error of $\sim 5 - 10\%$ (evaluation of both axes). Temperatures lower than 0.5 T_c could not be determined, because the thermal background is so much lower than the noise of the data in this case, that a Gaussian fit is not possible. The systematic uncertainty of the atom number evaluation is discussed in the next chapter. Fig. 4.5a) shows the condensate fraction as a function of the temperature with a fit function of $1 - (\frac{T}{T_c})^3$. The critical temperature is roughly 150nK.

4.5 Condensate atom number determination

The condensate atom number is determined by extracting the TF radius after TOF from the fit of Eq. 4.5 to the optical density distribution of the experimental data. The theoretical anisotropic expansion of the condensate obtained from the numerical integration of Eq. 4.7 is then used to calculate the inital TF radius in the trap, which gives the atom number according to Eq. 4.4. Note that the atom number cannot be extracted directly from integration of the parabola fit, because the optical density of the images is saturated in the center (typically at OD of 2-3). This means that the absorption in the center is so high, that all incident photons are absorbed and the transmission approaches 0. In this case, the height of the fit to the TF parabola is underestimated, while the TF radii are still accurate. Fig. 4.6 shows a typical condensate with $\sim 1.0 \times 10^6$ atoms in the F=1 Rb-87 ground state. The saturation of the condensate profile is clearly visible in this case.

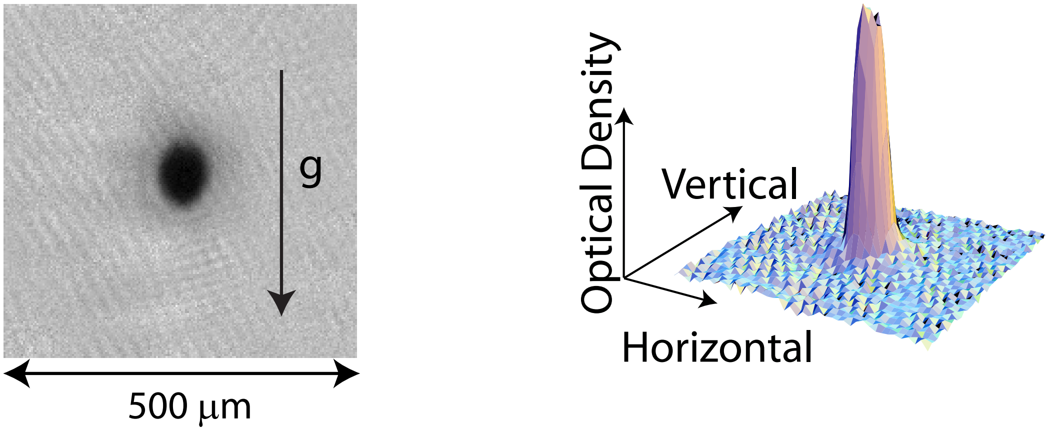

Figure 4.6: Typical data obtained after optimization. The TOF is 13 ms with trap frequencies $\omega_{ax} = 2\pi \times (70.4 \pm 0.1)$ Hz and $\omega_{rad} = 2\pi \times (25.0 \pm 0.1)$ Hz. As the image is saturated, the atom number can only be evaluated from the anisotropic expansion, yielding $\sim 1.0 \times 10^6$. The systematic error is estimated to be approximately $+10\%/-30\%$. Evaluation of the cloud at higher TOFs gives similar atom numbers.

Inspection of Eq. 4.4 reveals that N$\propto R_{TF}^5$, which causes an overall error of $\sim$ 50% for the condensate atom number determination (30% systematic error, 20% statistical error). In principle, three error sources contribute:

- In general the atom number from the expansion in axial direction is more reliable, because the relative change is much higher than on the radial axis. But $R_{TF,axial}$ is overestimated due to the motion of the cloud during the detection phase of 150 μs. This leaves a systematic error of $\sim 10\%$ after averaging the axial and radial atom numbers.

- The anisotropic expansion data from Fig. 4.4b)+c) suggests that blurring/diffraction causes systematic errors of $< 5\%$ for the TF radii. This translates into a systematic error of $\sim 20\%$ for the atom number.

- The TF radius determination from the image typically has an error of about 1 pixel, which results in an additional statistical uncertainty of $\sim 20\%$ in the atom number

To cross check the atom number evaluation, the condensate can be evaluated at large TOFs. As long as the condensate size does not exceed 2×10^5 atoms, the images are not saturated in the TOF region of 25 ms or higher. Under this condition, the height of the fit to the TF parabola can be trusted. Since the atom number is already known from the anisotropic expansion, an atom number calibration cal_{ae} can be extracted in this case. On the other hand, an atom number calibration cal_{fl} is already available, which was determined by fluorescence imaging in the MOT cell and estimating the amount of atoms in the BEC cell, cf. Chapter 2.5.
Alternatively, the phase-transition diagram can be used as another cross-check for the atom number determination by anisotropic expansion. The basic idea is to examine the influence of the atom number calibration on the fit to the theoretical prediction: by changing the atom number calibration, the condensate fraction and absolute temperature are still the same each data point, but $T_c(N)$ is shifted, as it depends on the absolute atom number. The quantity of interest is then how good $T_{c,rel}$ from the fit function $1 - (\frac{T_{rel}}{T_{c,rel}})^3$ to the phase diagram (Chapter 4.4) still matches the theoretical value of 1 for each possible atom number calibration, cf. Fig. 4.7. The lowest error is achieved for a calibration of 325 /pix. For comparison, the atom number calibrations from the anisotropic expansion and fluorescence imaging are also shown with their error bars. Assuming a 10% confidence interval for the fit of the phase transition curve to the data, a third calibration cal_{pt} can be extracted and compared with the other two calibrations.

$$
\begin{aligned}
\text{cal}_{fl} &= (310 \pm 60)\ /\text{pix} && (4.10)\\
\text{cal}_{ae} &= (360 \pm 140)\ /\text{pix} && (4.11)\\
\text{cal}_{pt} &= (325 - 80 + 120)\ /\text{pix} && (4.12)
\end{aligned}
$$

It is striking that the atom number calibrations match so well within their error bars, because three completely different types of physics were used to determine them (spontaneous emission of photons, condensate expansion of interacting bosons and phase transition diagram). According to the three calibrations, the systematic error of the atom number determination from the anisotropic expansion of the condensate seems to be about $+10\%/-30\%$, which is in the range of the a priori estimate for the systematic error from the beginning of this section.

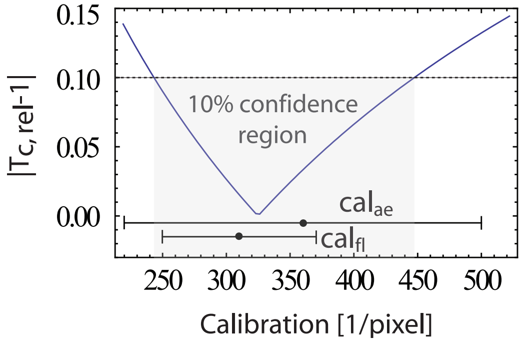

Figure 4.7: Dependence of the fit parameter $T_{c,rel}$ as a function of atom number calibration using $1-(\frac{T_{rel}}{T_{c,rel}})^3$ as fit function for the phase transition data. Ideally, $T_{c,rel}$ is 1. Assuming a 10% confidence interval, an atom number calibration cal_{pt} can be extracted (gray region).

4.6 Machine performance

For future experiments with condensates in optical lattices, it is very important that the cloud properties are reproducibile to be able to investigate physical effects. For example, a clear signature of the quantum phase transition from a Superfluid to a Mott-Insulator requires multiple images at different lattice depths. As the dipole trap was not yet fully operable to characterize the stability directly in that sense, condensates in the TOP trap were observed. The atom number reproducibility was found to be as good as the actual imaging stability (σ/mean $< 10\%$), while the position stability is better than 5 μm.

4.6.1 Position reproducibility

Since a mechanical transporter is used to transfer the laser cooled atom cloud from the MOT cell to the BEC cell, too large variations in the condensate position can result in significant modulations of the TOP trap bottom, which can cause the BEC to disappear. The stability is investigated by observing the condensate position for multiple runs for TOFs < 1 ms. A Gaussian is fit to every image to extract the cloud center, cf. Fig. 4.8. The runs were taken without any major pauses to observe the short-term drifts. The axial position shows a slow upwards drift with a $\sigma = 1$ μm and a range of 4 μm, while the horizontal direction has a larger drift and a $\sigma = 2$ μm with a range of 8 μm. The second horizontal axis cannot be observed, as it coincides with the imaging axis.
The slow systematic drift in the vertical data might be caused by the rise of the power cable temperature for the quadrupole trap. This can release stress on the coil holder increasing over run time. But even with cooldown pauses, the drift was still observable. An overall drift of the coil position due to the stress created by the scews holding them can also be excluded, as after very long pauses the cloud resumes its old position. The most probable cause is an external field: the optical lattice table exhibits a small magnetization resulting in a bias field of about ~ 4 G at the condensate position in axial direction. The reason is that the hole in the lattice table below the BEC cell breaks the magnetic shielding and allows magnetizations of $0.1 - 1\%$ stemming from the quadrupole field. For multiple runs this magentic field slowly saturates to ~ 4 G, while a remaining systematic drift and random variations of $1 - 10\%$ might still occur (~ 100 mG). In that sense, this might also be one of the major contributions to the scattering of the vertical data. Another reason for the scattering of the data might be the camera fan, which creates oscillations both of the CCD chip and on the imaging table. Since the evaporation takes 45 s, oscillations of the coil holder are already damped out when the image is taken. Finally, the spatial variations would correspond to drop time uncertainties of ~ 1 ms, so that unreproducible magnetic trap switch-offs cannot be the cause either.

The manufacturer gives an accuracy of the translation stage of ± 5 μm, which is probably one of the limiting factors to the scattering of the horizontal data. Another possibility is again the fan of the camera. Kicks of the condensate into the radial direction due to unreproducible switch-offs of the magnetic trap can be excluded as the cause for the scattering/drift. The kick velocity would have to be around 10 μm/ms, in order to be observable after

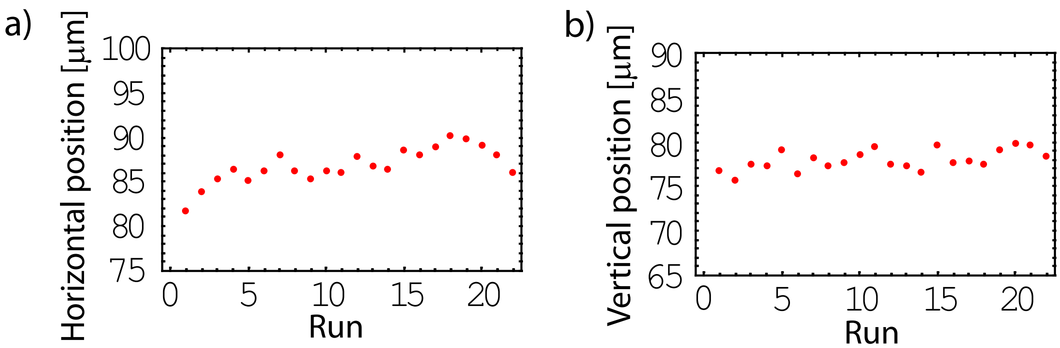

Figure 4.8: Condensate postition reproducibility in TOP trap. The position was determined with 0ms TOF by gaussian fits to the cloud profiles. a) is the radial variation, while b) is the axial direction. The third axis could not be observed for being parallel to the absorption imaging beam. For both data sets $\sigma < 5\mu$m, so that loading of a 1μK thermal cloud into a crossed dipole trap causes negligible heating.

$<$ 1 ms TOF. A cause for the drift in the horizontal data might be a small error in the position stabilization of the stage building up over several runs. Since the hole in the optical lattice table is not symmetric in x-direction (lab coordinates), the magnetic field from this table also has a component in the horizontal x-direction. Similar to the case of the vertical axis, this could results in both a drift and scattering of the horizontal position. But as the creep of the horizontal position disappears, if the stage settings are set to more stiffer values, this contribution can probably be neglected in this case.

4.6.2 Atom number stability

To measure the atom number stability, many almost pure condensates are made in the TOP trap and the atom number is observed, cf. Fig. 4.9. On a timescale of more than 100 minutes, the data shows very good stability with a scattering of σ/mean$\sim$ 6% and a range of 34%. The drift of the data is caused by the repump laser slowly shifting in frequency. This causes (N, T) not to be the ideal starting values in the BEC cell for the used evaporation sequence, so that the final BEC is smaller. After relocking, the atom number resumed the old value.

The scatter of the data is probably caused by the frequency jitter of the imaging laser (repumper), which is about $10 - 20\%$ of the natural linewidth of the F=1 imaging transition. To verify this, the integrated optical density of unevaporated clouds is measured in the BEC cell, inset of Fig. 4.9. From fluorescence measurements in the MOT cell before and after mechanical transport (which do not exhibit laser jitter problems due to the much longer exposure time), the atom number is determined to be very stable within 1% or less, while the scattering in the absorbtion images is 8% with a range of 30%. This means that the real condensate atom number is probably even more stable than indicated by the data. This also means that the rotating bias field of the TOP trap is so uniform over the length scale of the condensate position variations that an influence of trap bottom shifts on the condensate size are negligible.

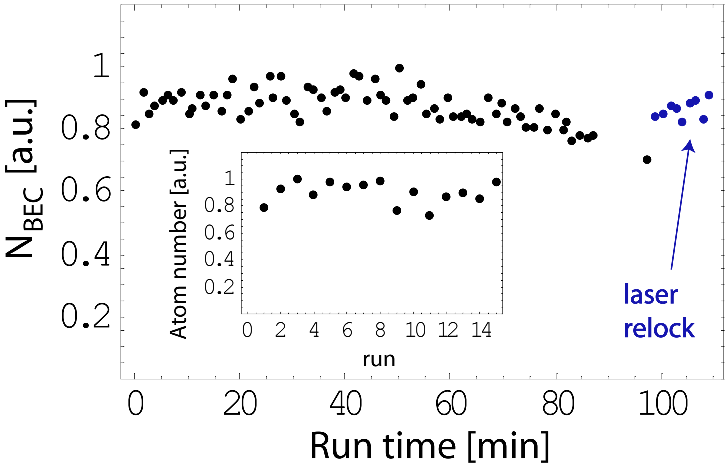

Figure 4.9: Condensate atom number stability. Over more than 100 minutes runtime, the scattering is only σ/mean = 6%. This is roughly the quality of the imaging due to frequency jitter of the imaging laser (σ/mean = 8%), which is shown in the inset by observing clouds of the same atom numbers. Therefore, the condensate atom number is probably even more stable than 6%. The overall drift is caused by the repump laser slowly falling out of lock.

Chapter 5

Conclusion

We have created the first Rb-87 Bose-Einstein Condensate in a moving coil TOP trap geometry. The condensates were made in the $|1,-1\rangle$ state. In our setup, the laser cooled atoms are transported along a curved path into a glass cell using a moving-coil quadrupole magnetic trap. RF-forced evaporative cooling is performed in a TOP trap, formed by the moving coil quadrupole field in conjunction with a rotating bias field. Evaporative cooling simulations were carried out to provide a guideline for the optimization in the experiment. This way, the initial condensate size of $\sim 1 \times 10^5$ could be increased to $\sim 1 \times 10^6$ atoms with a critical temperature of 150nK. Our data agrees well with the theoretical predictions of the phase transition and anisotropic expansion. A consistency check was performed for the atom number determination, which gives an estimated systematic uncertainty of $+10\%/-30\%$.
The condensate atom number is found to be stable within 6%, while the position stability is approximately 5 μm in the axial and 10 μm in the radial direction of the magnetic TOP trap. These numbers are very promising for condensation in a dipole trap and future experiments in optical lattices. The position uncertainty corresponds to heating of ~ 100 nK in an optical trap with a depth of 5 μK, which is negligible if the trap is loaded at a cloud temperature of 1 μK. The final evaporation can then be performed by lowering the laser power to reduce the trap depth.

Bibliography

[1] S. N. Bose, Plancks Gesetz und Lichtquantenhypothese, *Zeitschrift für Physik* **26**, 178 (1924).

[2] A. Einstein, Quantentheorie des einatomigen idealen Gases, *Sitzungsbericht der Preußischen Akademie der Wissenschaften* **XXII**, 261 (1924).

[3] A. Einstein, Quantentheorie des einatomigen idealen Gases. Zweite Abhandlung, *Sitzungsbericht der Preußischen Akademie der Wissenschaften* **II**, 3 (1925).

[4] A. Einstein, Zur Quantentheorie des idealen Gases, *Sitzungsbericht der Preußischen Akademie der Wissenschaften* **III**, 18 (1925).

[5] F. London, The λPhenomenon of Liquid Helium and the Bose-Einstein Degeneracy, *Nature* **141**, 643 (1938).

[6] H. J. Metcalf and P. van der Straten, *Laser Cooling and Trapping* (Springer, Berlin, 1999).

[7] H. F. Hess, Evaporative cooling of magnetically trapped and compressed spin-polarized hydrogen, *Phys. Rev. B* **34**, 3476 (1986).

[8] M. H. Anderson, J. R. Ensher, M. R. Matthews, C. E. Wieman, and E. A. Cornell, Observation of Bose-Einstein Condensation in a Dilute Atomic Vapor, *Science* **269**, 198 (1995).

[9] C. C. Bradley, C. A. Sackett, J. J. Tollet, and R. G. Hulet, Evidence of Bose-Einstein Condensation in an Atomic Gas with Attractive Interactions, *Phys. Rev. Lett.* **75**, 1688 (1995).

[10] C. C. Bradley, C. A. Sackett, and R. G. Hulet, Bose-Einstein Condensation of Lithium: Observation of Limited Condensate Number, *Phys. Rev. Lett.* **78**, 985 (1997).

[11] K. Davis, M. Mewes, M. Andrews, N. van Druten, D. Durfee, D. Kurn, and W. Ketterle, Bose-Einstein Condensation in a Gas of Sodium, *Phys. Rev. Lett.* **75** (1995).

[12] D. G. Fried, T. C. Killian, L. Willmann, D. Landhuis, S. C. Moss, D. Kleppner, and T. J. Greytak, Bose-Einstein Condensation of Atomic Hydrogen, *Phys. Rev. Lett.* **81**, 3811 (1998).

[13] S. L. Cornish, N. R. Claussen, J. L. Roberts, E. A. Cornell, and C. E. Wieman, Stable ^{85}Rb Bose-Einstein Condensates with Widely Tunable Interactions, *Phys. Rev. Lett.* **85**, 1795 (2000).

[14] G. Modugno, G. Ferrari, G. Roati, R. J. Brecha, A. Simoni, and M. Inguscio, Bose-Einstein Condensation of Potassium Atoms by Sympathetic Cooling, *Science* **294**, 1320 (2001).

[15] A. Robert, O. Sirjean, A. Browaeys, J. Poupard, S. Nowak, D. Boiron, C. I. Westbrook, and A. Aspect, A Bose-Einstein Condensate of Metastable Atoms, *Science* **292**, 461 (2001).

[16] F. P. D. Santos, J. Léonard, J. Wang, C. J. Barrelet, F. Perales, E. Rasel, C. S. Unnikrishnan, M. Leduc, and C. Cohen-Tannoudji, Bose-Einstein Condensation of Metastable Helium, *Phys. Rev. Lett.* **86**, 3459 (2001).

[17] T. Weber, J. Herbig, M. Mark, H.-C. Nägerl, and R. Grimm, Bose-Einstein Condensation of Cesium, *Science* **299**, 232 (2003).

[18] Y. Takasu, K. Maki, K. Komori, T. Takano, K. Honda, M. Kumakura, T. Yabuzaki, and Y. Takahashi, Spin-Singlet Bose-Einstein Condensation of Two-Electron Atoms, *Phys. Rev. Lett.* **91**, 0404041 (2003).

[19] A. Griesmaier, J. Werner, S. Hensler, J. Stuhler, and T. Pfau, Bose-Einstein Condensation of Chromium, *Phys. Rev. Lett.* **94**, 1604011 (2005).

[20] D. S. Jin, J. R. Ensher, M. R. Matthews, C. E. Wieman, and E. A. Cornell, Collective Excitations of a Bose-Einstein Condensate in a Dilute Gas, *Phys. Rev. Lett.* **77**, 420 (1996).

[21] M. R. Andrews, D. M. Kurn, H.-J. Miesner, D. S. Durfee, C. G. Townsend, S. Inouye, and W. Ketterle, Propagation of Sound in a Bose-Einstein Condensate, *Phys. Rev. Lett.* **79**, 553 (1997).

[22] M. R. Andrews, C. G. Townsend, H.-J. Miesner, D. S. Durfee, D. M. Kurn, and W. Ketterle, Observation of Interference Between Two Bose Condensates, *Science* **275**, 637 (1997).

[23] M.-O. Mewes, M. R. Andrews, D. M. Kurn, D. S. Durfee, C. G. Townsend, and W. Ketterle, Output Coupler for Bose-Einstein Condensed Atoms, *Phys. Rev. Lett.* **78**, 582 (1997).

[24] I. Bloch, T. W. Hänsch, and T. Esslinger, Atom Laser with a cw Output Coupler, *Phys. Rev. Lett.* **82**, 3008 (1999).

[25] L. Deng, E. W. Hagley, J. Wen, M. Trippenbach, Y. Band, P. Luienne, J. E. Simsarian, K. Helmerson, S. L. Rolston, and W. D. Phillips, Four-wave mixing with, *Nature* **198**, 218 (1999).

[26] J. Stenger, S. Inouye, A. P. Chikkatur, D. M. Stamper-Kurn, D. E. Pritchard, and W. Ketterle, Bragg Spectroscopy of a Bose-Einstein Condensate, *Phys. Rev. Lett.* **82**, 4569 (1999).

[27] M. R. Matthews, B. P. Anderson, P. C. Haljan, D. S. Hall, C. E. Wieman, and E. A. Cornell, Vortices in a Bose-Einstein Condensate, *Phys. Rev. Lett.* **83**, 2498 (1999).

[28] C. Raman, M. Köhl, R. Onofrio, D. S. Durfee, C. E. Kuklewicz, Z. Hadzibabic, and W. Ketterle, Evidence for a Critical Velocity in a Bose-Einstein Condensed Gas, *Phys. Rev. Lett.* **83**, 2502 (1999).

[29] M. Greiner, O. Mandel, T. Esslinger, T. W. Hänsch, and I. Bloch, Quantum phase transition from a superfluid to a Mott insulator in a gas of ultracold atoms, *Nature* **415**, 39 (2002).

[30] M. W. Zwierlein, C. A. Stan, C. H. Schunck, S. M. F. Raupach, S. Gupta, Z. Hadzibabic, and W. Ketterle, Observation of Bose-Einstein Condensation of Molecules, *Phys. Rev. Lett.* **91**, 250401 (2003).

[31] M. Greiner, C. A. Regal, and D. S. Jin, Emergence of a molecular Bose-Einstein condensate from a Fermi gas, *Nature* **426**, 537 (2003).

[32] S. Jochim, M. Bartenstein, A. Altmeyer, G. Hendl, S. Riedl, C. Chin, J. Hecker Denschlag, and R. Grimm, Bose-Einstein Condensation of Molecules, *Science* **302**, 2101 (2003).

[33] M. W. Zwierlein, C. A. Stan, C. H. Schunck, S. M. F. Raupach, A. J. Kerman, and W. Ketterle, Condensation of Pairs of Fermionic Atoms near a Feshbach Resonance, *Phys. Rev. Lett.* **92**, 120403 (2004).

[34] C. A. Regal, M. Greiner, and D. S. Jin, Observation of Resonance Condensation of Fermionic Atom Pairs, *Phys. Rev. Lett.* **92**, 040403 (2004).

[35] G. B. Partridge, W. Li, Y. A. Liao, R. G. Hulet, M. Haque, and H. T. C. Stoof, Deformation of a Trapped Fermi Gas with Unequal Spin Populations, *Physical Review Letters* **97**, 190407 (2006).

[36] M. W. Zwierlein, A. Schirotzek, C. H. Schunck, and W. Ketterle, Fermionic Superfluidity with Imbalanced Spin Populations, *Science* **311**, 492 (2006).

[37] D. A. Steck, *Rubidium 87 D Line Data*, http://steck.us/alkalidata 2003.

[38] Y. Yoshikawa, T. Umeki, T. Mukae, Y. Torii, and T. Kuga, Frequency stabilization of a laser diode with use of light-induced birefringence in an atomic vapor, *Appl. Opt.* **42**, 6645 (2003).

[39] D. E. Sproles, *in preparation*, Master's thesis, Stony Brook University, 2007.

[40] S. G. Albert, *Cooling, Trapping and Transport of Atom Clouds in a New BEC Apparatus*, Master's thesis, Stony Brook University, 2007.

[41] W. Petrich, M. H. Anderson, J. R. Ensher, and E. A. Cornell, Stable, Tightly Confining Magnetic Trap for Evaporative Cooling of Neutral Atoms, *Phys. Rev. Lett.* **74**, 3352 (1995).

[42] M. Mewes, M. Andrews, N. van Druten, D. Kurn, D. Durfee, and W. Ketterle, Bose-Einstein Condensation in a Tightly Confining dc Magnetic Trap, *Phys. Rev. Lett.* **77** (1996).

[43] D. Stamper-Kurn, M. Andrews, A. Chikkatur, S. Inouye, H. Miesner, J. Stenger, and W. Ketterle, Optical Confinement of a Bose-Einstein Condensate, *Phys. Rev. Lett.* **80** (1998).

[44] J. R. Ensher, *The First Experiments with Bose-Einstein Condensation of Rb87*, PhD thesis, University of Colorado at Boulder 1997.

[45] D. Pertot and D. Sproles, *(private communication).*

[46] A. Rich, Shielding and Guarding, *Analog Devices - Application Notes* **AN-347**.

[47] C. Cohen-Tannoudji, J. Dupont-Roc, and G. Grynberg, *Atom-Photon Interactions* (Wiley-VCH, Weinheim, 2004).

[48] W. Ketterle, D. S. Durfee, and D. M. Stamper-Kurn, *Making, probing and understanding Bose-Einstein condensates* 1999.

[49] C. Wieman, G. Flowers, and S. Gilbert, Inexpensive laser cooling and trapping experiment for undergraduate laboratories, *American Journal of Physics* **63**, 317 (1995).

[50] E. L. Raab, M. Prentiss, A. Cable, S. Chu, and D. E. Pritchard, Trapping of Neutral Sodium Atoms with Radiation Pressure, *Phys. Rev. Lett.* **59**, 2631 (1987).

[51] C. G. Townsend, N. H. Edwards, C. J. Cooper, K. P. Zetie, A. M. Steane, P. Szriftgiser, H. Perrin, and J. Dalibard, Phase-space density in the magneto-optical trap, *Phys. Rev. A* **52**, 1423 (1995).

[52] A. M. Steane, M. Chowdhury, and C. J. Foot, Radiation force in the magneto-optical trap, *J. Opt. Soc. Am. B* **9**, 2142 (1992).

[53] H. Ruf, *Progress report from the Schneble lab, unpublished*, 2006.

[54] W. Petrich, M. H. Anderson, J. R. Ensher, and E. A. Cornell, Behavior of atoms in a compressed magneto-optical trap, *Journal of the Optical Society of America B Optical Physics* **11**, 1332 (1994).

[55] S. Chu, L. Hollberg, J. E. Bjorkholm, A. Cable, and A. Ashkin, Three-Dimensional Viscous Confinement and Cooling of Atoms by Resonance Radiation Pressure, *Phys. Rev. Lett.* **55**, 48 (1985).

[56] P. D. Lett, R. N. Watts, C. I. Westbrook, W. D. Phillips, P. L. Gould, and H. J. Metcalf, Observation of Atoms Laser Cooled below the Doppler Limit, *Phys. Rev. Lett.* **61**, 169 (1988).

[57] J. Dalibard and C. Cohen-Tannoudji, Laser cooling below the Doppler limit by polarization gradients: simple theoretical models, *J. Opt. Soc. Am. B* **6**, 2023 (1989).

[58] T. Bergeman, G. Erez, and H. J. Metcalf, Magnetostatic trapping fields for neutral atoms, *Phys. Rev. A* **35**, 1535 (1987).

[59] C. Klempt, T. van Zoest, T. Henninger, O. Topic, E. Rasel, W. Ertmer, and J. Arlt, UV light-induced atom desorption for large rubidium and potassium magneto-optical traps, *Phys. Rev. A* **73**, 0134100 (2006).

[60] J. Dalibard and C. Cohen-Tannoudji, Dressed-atom approach to atomic motion in laser light - The dipole force revisited, *Journal of the Optical Society of America B Optical Physics* **2**, 1707 (1985).

[61] E. W. Streed, A. P. Chikkatur, T. L. Gustavson, M. Boyd, Y. Torii, D. Schneble, G. K. Campbell, D. E. Pritchard, and W. Ketterle, Large atom number Bose-Einstein condensate machines, *Review of Scientific Instruments* **77**, 023106 (2006).

[62] U. Ernst, A. Marte, F. Schreck, J. Schuster, and G. Rempe, Bose-Einstein condensation in a pure Ioffe-Pritchard field configuration, *EPL (Europhysics Letters)* **41**, 1 (1998).

[63] A. Marte, *Feshbach-Resonanzen bei Stoessen ultrakalter Rubidiumatome*, PhD thesis, Max-Planck Institut für Quantenoptik 2003.

[64] W. Ketterle and N. van Druten, Evaporative cooling of trapped atoms, *Adv. At. Mol. Opt. Phys.* **37**, 181 (1996).

[65] H. F. Hess, G. P. Kochanski, J. M. Doyle, N. Masuhara, D. Kleppner, and T. J. Greytak, Magnetic trapping of spin-polarized atomic hydrogen, *Phys. Rev. Lett.* **59**, 672 (1987).

[66] I. D. Setija, H. G. C. Werij, O. J. Luiten, M. W. Reynolds, T. W. Hijmans, and J. T. M. Walraven, Optical cooling of atomic hydrogen in a magnetic trap, *Phys. Rev. Lett.* **70**, 2257 (1993).

[67] C. L. Cesar, D. G. Fried, T. C. Killian, A. D. Polcyn, J. C. Sandberg, I. A. Yu, T. J. Greytak, D. Kleppner, and J. M. Doyle, Two-Photon Spectroscopy of Trapped Atomic Hydrogen, *Phys. Rev. Lett.* **77**, 255 (1996).

[68] M. D. Barrett, J. A. Sauer, and M. S. Chapman, All-Optical Formation of an Atomic Bose-Einstein Condensate, *Phys. Rev. Lett.* **87**, 010404 (2001).

[69] M. Hammes, D. Rychtarik, H.-C. Nägerl, and R. Grimm, Cold-atom gas at very high densities in an optical surface microtrap, *Phys. Rev. A* **66**, 051401 (2002).

[70] D. E. Pritchard, K. Helmerson, and G. A. Martin, Atom Traps, *Atomic Physics 11* **11**, 179 (1989).

[71] A. G. Martin, K. Helmerson, V. S. Bagnato, G. P. Lafyatis, and D. E. Pritchard, rf Spectroscopy of Trapped Neutral Atoms, *Phys. Rev. Lett.* **61**, 2431 (1988).

[72] O. J. Luiten, H. G. C. Werij, I. D. Setija, M. W. Reynolds, T. W. Hijmans, and J. T. M. Walraven, Lyman-alpha spectroscopy of magnetically trapped atomic hydrogen, *Phys. Rev. Lett.* **70**, 544 (1993).

[73] L. Landau, *Phys. Z. Sowjetunion* **2** (1932).

[74] C. Zener, *Proc. R. Soc. London A* **137**, 696 (1932).

[75] C. E. Carroll and F. T. Hioe, *J. Phys. A: Math. Gen.* **19**, 1151 (1986).

[76] E. T. Whittaker, *Bull. Am. Math. Soc.* **10** (1903).

[77] E. T. Whittaker and G. N. Watson, *A Course of Modern Analysis* (Cambridge University Press, Cambridge, 1927).

[78] H. Wu, E. Arimondo, and C. J. Foot, Dynamics of evaporative cooling for Bose-Einstein condensation, *Phys. Rev. A* **56**, 560 (1997).

[79] J. M. Doyle, J. C. Sandberg, I. A. Yu, C. L. Cesar, D. Kleppner, and T. J. Greytak, Evaporative cooling of atomic hydrogen: Theory of cooling and progress towards the Bose-Einstein transition, *Physica B Condensed Matter* **194**, 13 (1994).

[81] M. Yamashita, M. Koashi, T. Mukai, M. Mitsunaga, and N. Imoto, Dynamics of evaporative cooling in magnetically trapped atomic hydrogen, *Phys. Rev. A* **62**, 033602 (2000).

[82] M. Yamashita, M. Koashi, T. Mukai, M. Mitsunaga, N. Imoto, and T. Mukai, Optimization of evaporative cooling towards a large number of Bose-Einstein-condensed atoms, *Phys. Rev. A* **67**, 023601 (2003).

[83] T. Mukai and M. Yamashita, Efficient rapid production of a Bose-Einstein condensate by overcoming serious three-body loss, *Physical Review A (Atomic, Molecular, and Optical Physics)* **70**, 013615 (2004).

[80] M. Holland, J. Williams, K. Coakley, and J. Cooper, Trajectory simulation of kinetic equations for classical systems , *Quantum and Semiclassical Optics* **8**, 571 (1996).

[84] C. A. Sackett, C. C. Bradley, and R. G. Hulet, Optimization of evaporative cooling, *Phys. Rev. A* **55**, 3797 (1997).

[85] O. J. Luiten, M. W. Reynolds, and J. T. M. Walraven, Kinetic theory of the evaporative cooling of a trapped gas, *Phys. Rev. A* **53**, 381 (1996).

[86] D. W. Snoke and J. P. Wolfe, Population dynamics of a Bose gas near saturation, *Phys. Rev. B* **39**, 4030 (1989).

[87] K. B. Davis, M. O. Mewes, and W. Ketterle, An analytical model for evaporative cooling of atoms, *Applied Physics B* **60**, 155 (1995).

[88] C. J. Myatt, *Bose-Einstein Condensation experiments in a dilute vapor of Rubidium*, PhD thesis, University of Colorado, Boulder, Colorado 1997.

[89] D. Comparat, A. Fioretti, G. Stern, E. Dimova, B. L. Tolra, and P. Pillet, Optimized production of large Bose-Einstein condensates, *Adv. At. Mol. Opt. Phys.* **73**, 043410 (2006).

[90] E. L. Surkov, J. T. M. Walraven, and G. V. Shlyapnikov, Collisionless motion and evaporative cooling of atoms in magnetic traps, *Phys. Rev. A* **53**, 3403 (1996).

[91] C. Pethick and H. Smith, *Bose-Einstein condensates in dilute gases* (Cambridge University Press, Cambridge, UK, 2002).

[92] F. Dalfovo, S. Giorgini, L. P. Pitaevskii, and S. Stringari, Theory of Bose-Einstein condensation in trapped gases, *Rev. Mod. Phys.* **71**, 463 (1999).

[93] L. Pitaevskii and S. Stringari, *Bose-Einstein condensation* (Oxford University Press, Oxford, UK, 2003).

[94] M. Köhl, M. J. Davis, C. W. Gardiner, T. W. Hänsch, and T. Esslinger, Growth of Bose-Einstein Condensates from Thermal Vapor, *Phys. Rev. Lett.* **88**, 080402 (2002).

[95] S. Giorgini, L. P. Pitaevskii, and S. Stringari, Scaling and Thermodynamics of a Trapped Bose-Condensed Gas, *Phys. Rev. Lett.* **78**, 3987 (1997).

[96] J. R. Ensher, D. S. Jin, M. R. Matthews, C. E. Wieman, and E. A. Cornell, Bose-Einstein Condensation in a Dilute Gas: Measurement of Energy and Ground-State Occupation, *Phys. Rev. Lett.* **77**, 4984 (1996).

[97] M. Holland and J. Cooper, Expansion of a Bose-Einstein condensate in a harmonic potential, *Phys. Rev. A* **53**, R1954 (1996).

[98] Y. Castin and R. Dum, Bose-Einstein Condensates in Time Dependent Traps, *Phys. Rev. Lett.* **77**, 5315 (1996).

Appendix A

Evaporative cooling simulation details

A.1 Analytic solutions

The conditions for the three break-even curves of constant collision ratio, density and phase-space density can be found by using the scaling behaviour from Tab. 3.1 including the losses from the background:

- Constant PSD: $\left(\frac{\Gamma_{inc}(\xi+3/2,\eta)}{\Gamma(\xi+3/2)}\right)^{\xi+5/2} e^{-\frac{2.7\Gamma_{bkg}}{\Gamma_{el}}} = \left(\frac{\Gamma_{inc}(\xi+5/2,\eta)}{\Gamma(\xi+5/2)}\right)^{\xi+3/2}$
- Constant d: $\left(\frac{\Gamma_{inc}(\xi+3/2,\eta)}{\Gamma(\xi+3/2)}\right)^{\xi+1} e^{-\frac{2.7\Gamma_{bkg}}{\Gamma_{el}}} = \left(\frac{\Gamma_{inc}(\xi+5/2,\eta)}{\Gamma(\xi+5/2)}\right)^{\xi}$
- Constant Γ_{el}: $\left(\frac{\Gamma_{inc}(\xi+3/2,\eta)}{\Gamma(\xi+3/2)}\right)^{\xi+1/2} e^{-\frac{2.7\Gamma_{bkg}}{\Gamma_{el}}} = \left(\frac{\Gamma_{inc}(\xi+5/2,\eta)}{\Gamma(\xi+5/2)}\right)^{\xi-1/2}$

In the case of starting exactly on the break-even curve for the collision rate in a harmonic trap, the differential equations for the evaporation simulation Eq. 3.6 become analytically solvable. In the Taylor approximation of slowly changing parameters in a harmonic trap, the solutions read [**?**]:

$$\begin{aligned} N(t) &\propto Exp\left[-\left(\Gamma_{el}\frac{(1+\eta+\eta^2/2)e^{-\eta}}{4}+\Gamma_{bkg}\right)t\right] \\ T(t) &\propto Exp\left[-\Gamma_{el}\frac{\eta^3 e^{-\eta}}{24}t\right] \\ \nu_{rf}(t) &\propto Exp\left[-\Gamma_{el}\frac{\eta^3 e^{-\eta}}{24}t\right] \end{aligned}$$

The two relevant timescales τ_{el} and τ_{evap} are connected by $\tau_{evap}/\tau_{el} = 24e^{\eta}/\eta^3 \sim 30$. Typical elastic collision rates are 1s, which sets the evaporation timescale to $\sim$ 1min.

A.2 Additional formulas

In this section some additional relations for the evaporation simulation are discussed to complete the discussion from Chapter 3.2.2. Assuming an adiabatic loading from the quadrupole to the TOP trap, the new temperature is given by the condition of equal phase space densities and the relation between temperature T and volume V for both traps. This can be found by integration of the density function in the ergodic regime using the classical Boltzmann statistics. Even though the cloud distribution is not discrete, the density N/V corresponds to the maximal density in the center:

$$\begin{aligned}
V_{lin}(T) &= \alpha_{lin} T^3, \qquad \alpha_{lin} = \left(\frac{2k_B}{g_F m_F \mu_B B_{ax}}\right)^3 \int_{-\infty}^{\infty} e^{-\sqrt{x^2+y^2+4z^2}} dxdydz \\
V_{harm}(T) &= \alpha_{harm} T^{3/2}, \quad \alpha_{harm} = \left(\frac{2k_B}{m_{Rb87}\omega^2_{rad,TOP}}\right)^{3/2} \int_{-\infty}^{\infty} e^{-x^2-y^2-8z^2} dxdydz \\
\frac{1}{V_{lin} T_{lin}^{3/2}} &= \frac{1}{V_{harm} T_{harm}^{3/2}} \qquad \Rightarrow T_{harm} = \left(\frac{\alpha_{lin}}{\alpha_{harm}}\right)^{1/3} T_{lin}^{3/2}
\end{aligned}$$

In the case of the circle of death following the rf-knife the trap stiffening can be described again by the adiabatic assumption leading to a new cloud temperature T':

$$\frac{T'_{harm}}{T_{harm}} = \left(\frac{\alpha_{harm}(B_{TOP})}{\alpha_{harm}(B'_{TOP})}\right)^{1/3}, \quad \frac{V'_{harm}}{V_{harm}} = \sqrt{\frac{\alpha_{harm}(B'_{TOP})}{\alpha_{harm}(B_{TOP})}}, \quad \frac{\Gamma'_{el}}{\Gamma_{el}} = \left(\frac{\alpha_{harm}(B_{TOP})}{\alpha_{harm}(B'_{TOP})}\right)^{2/3}$$

A.3 Algorithm

▪ Scaling Functions

```
In[1]:= << C:\\BECIVTools\\PhysConst.m;
        Gammainc[a_, η_] := ∫_0^η x^(a-1) Exp[-x] ⅆx;
        Nfactor[η_, colratio_, ξ_] := Gammainc[ξ + 3 / 2, η] / Gamma[ξ + 3 / 2] * Exp[- 2.7 / colratio];
        Efactor[η_, colratio_, ξ_] := Gammainc[ξ + 5 / 2, η] / Gamma[ξ + 5 / 2] * Exp[- 2.7 / colratio];
        Tfactor[η_, colratio_, ξ_] := Efactor[η, colratio, ξ] / Nfactor[η, colratio, ξ];
        γnewtoγoldfactor[η_, colratio_, ξ_] := Nfactor[η, colratio, ξ] / Tfactor[η, colratio, ξ] ^ (ξ - 0.5);
        nnewtonoldfactor[η_, colratio_, ξ_] := Nfactor[η, colratio, ξ] / Tfactor[η, colratio, ξ] ^ (ξ);
        PSDnewtoPSDoldfactor[η_, colratio_, ξ_] := Nfactor[η, colratio, ξ] / Tfactor[η, colratio, ξ] ^ (ξ + 3 / 2);
```

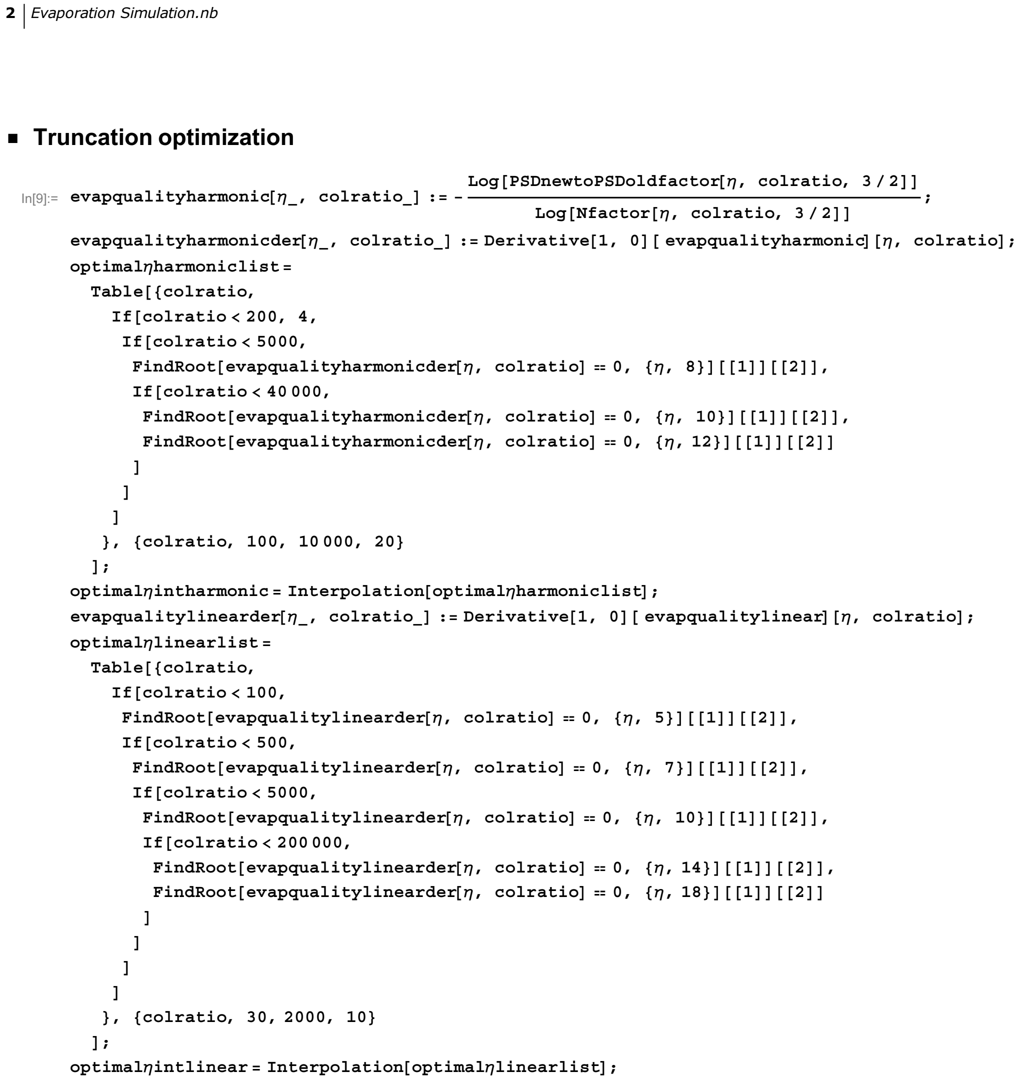

■ Truncation optimization

```
                                                      Log[PSDnewtoPSDoldfactor[η, colratio, 3 / 2]]
In[9]:= evapqualityharmonic[η_, colratio_] := - ─────────────────────────────────────────────;
                                                         Log[Nfactor[η, colratio, 3 / 2]]
        evapqualityharmonicder[η_, colratio_] := Derivative[1, 0][evapqualityharmonic][η, colratio];
        optimalηharmoniclist =
          Table[{colratio,
            If[colratio < 200, 4,
             If[colratio < 5000,
              FindRoot[evapqualityharmonicder[η, colratio] == 0, {η, 8}][[1]][[2]],
              If[colratio < 40 000,
               FindRoot[evapqualityharmonicder[η, colratio] == 0, {η, 10}][[1]][[2]],
               FindRoot[evapqualityharmonicder[η, colratio] == 0, {η, 12}][[1]][[2]]
              ]
             ]
            ]
           }, {colratio, 100, 10 000, 20}
          ];
        optimalηintharmonic = Interpolation[optimalηharmoniclist];
        evapqualitylinearder[η_, colratio_] := Derivative[1, 0][evapqualitylinear][η, colratio];
        optimalηlinearlist =
          Table[{colratio,
            If[colratio < 100,
             FindRoot[evapqualitylinearder[η, colratio] == 0, {η, 5}][[1]][[2]],
             If[colratio < 500,
              FindRoot[evapqualitylinearder[η, colratio] == 0, {η, 7}][[1]][[2]],
              If[colratio < 5000,
               FindRoot[evapqualitylinearder[η, colratio] == 0, {η, 10}][[1]][[2]],
               If[colratio < 200 000,
                FindRoot[evapqualitylinearder[η, colratio] == 0, {η, 14}][[1]][[2]],
                FindRoot[evapqualitylinearder[η, colratio] == 0, {η, 18}][[1]][[2]]
               ]
              ]
             ]
            ]
           }, {colratio, 30, 2000, 10}
          ];
        optimalηintlinear = Interpolation[optimalηlinearlist];
```

▪ Trap parameters

In[16]:=

```
gF = 0.5;
mF = 1;
b = 353.;(*G/cm*)
QP = b / 2;(*G/cm*)
α = 1; (*ration of CoD and rf-knife*)
```

$$\texttt{CircleofDeath[top\_] := } \frac{\texttt{top}}{\texttt{QP}} * \texttt{10\^{}(-2);(*m*)}$$

$$\omega\texttt{rad[top\_] := } \frac{\texttt{QP} * \texttt{10\^{}(-4)} * \texttt{100}}{\sqrt{\texttt{top}}} * \sqrt{\frac{\mu_B * m_F * g_F}{87 * m_u * 2}}\ ;$$

```
ωax[top_] := (Sqrt[8] * ωrad[top]);
frad[top_] := ωrad[top] / (2 * π);
fax[top_] := (Sqrt[8] * ωrad[top]) / (2 * π);
TOPOffset[top_] := μB * mF * gF * top;
```

$$\alpha\texttt{lin := N}\left[\int_{-\infty}^{\infty}\int_{-\infty}^{\infty}\int_{-\infty}^{\infty}\texttt{Exp[-Sqrt[x\^{}2 + y\^{}2 + 4 z\^{}2]]}\, dx\, dy\, dz\right] * \left(\frac{2 * k_B}{g_F * m_F * \mu_B * \texttt{(b * 10\^{}(-2))}}\right)\texttt{\^{}3;}$$

$$\texttt{helper := N}\left[\int_{-\infty}^{\infty}\int_{-\infty}^{\infty}\int_{-\infty}^{\infty}\texttt{Exp[-x\^{}2 - y\^{}2 - 8 * z\^{}2]}\, dx\, dy\, dz\right];$$

$$\alpha\texttt{harm[top\_] := helper} * \left(\sqrt{\frac{2 * k_B}{87 * m_u * \omega\texttt{ax[top]\^{}2}}}\right)\texttt{\^{}3;}$$

```
Vharm[T_, top_] := αharm[top] * T^(3 / 2);
Vlin[Tlin_] := αlin * Tlin^3;
```

$$\tau\texttt{b[T\_] := 1} \Big/ \left(\texttt{1 / 132 + 1} \Big/ \left(\texttt{0.00276277} * \left(10^6 * \texttt{T}\right)^2\right)\right);$$

■ Evaporation in linear Trap

```
PreEvaporation[{atomnumber_, temperature_, Tfinal_}] := Module[
  {AtNum, T, ξ, τth, τel, τbkg, t, η, Nthing, Tthing, databeginning, dataend, AtNuminitial,
   Tinitial, τthinitial, τbinitial, Tscale, Nscale, PSDinitial, PSD, Ecut, colratio, data},
  AtNuminitial = 1. * 10 ^ 9; Tinitial = 500. * 10 ^ (-6); τthinitial = 2.; τbinitial = τb[Tinitial];
                        ħ ^ 3 * (2 π) ^ 3              AtNuminitial
  PSDinitial = ---------------------------------- * --------------;
               (√(2 π * 87 * m_u * k_B * Tinitial)) ^ 3  Vlin[Tinitial]
  ξ = 3;
        (T / Tinitial) ^ (ξ - 0.5)
  τth = -------------------------- * τthinitial;
         AtNum / AtNuminitial
  τel = τth / 2.7;
  τbkg = τb[T];
             τbkg
  colratio = ----;
             τel
          AtNum / AtNuminitial
  PSD = ------------------------ * PSDinitial;
        (T / Tinitial) ^ (ξ + 3 / 2)
  t = 0;
  η = optimalηintlinear[colratio];
  AtNum = atomnumber;
  T = temperature;
  Ecut = k_B * T * η;
  data = {{t, AtNum, T, Ecut, colratio, τel, τbkg, PSD}};
  If[colratio < 20, data = Join[data, {{0, 0, 0, 0, 0, 0, 0, 0}}],
   While[T > Tfinal,
      t = t +   τbkg    * 2.7;
              --------
              colratio
      If[colratio < 30, η = 5, η = optimalηintlinear[colratio]];
      Nscale = Nfactor[η, colratio, ξ];
      Tscale = Tfactor[η, colratio, ξ];
      AtNum = Nscale * AtNum;
      T = Tscale * T;
            Tscale^ (ξ - 0.5)
      τel = ----------------- * τel;
                 Nscale
      τbkg = τb[T];
                 τbkg
      colratio = ----;
                 τel
                         Nscale
      PSD = PSD * -------------------;
                  Tscale^ (ξ + 3 / 2)
      Ecut = k_B * T * η;
      data = Join[data, {{t, AtNum, T, Ecut, colratio, τel, τbkg, PSD}}]
     ];
  ];
  {{atomnumber, temperature, Tfinal}, data}
 ];
```

Evaporation in TOP Trap

$$\texttt{TOPTemp[TQP\_, top\_] :=} \left(\frac{\alpha\texttt{lin}}{\alpha\texttt{harm[top]}}\right)\texttt{\^{}(1/3)*(TQP)\^{}(3/2);}$$

```
Evaporationstiffening[{atomnumber_, temperature_, topbeginning_}] := Module[
  {AtNumbeginning, Tbegninning, PSD, colratio, η, dataend, AtNuminitial, Tinitial,
   TOPfieldinitial, τbinitial, τthinitial, τelinitial, colratioinitial, PSDinitial,
   ξ, T, AtNum, τth, τel, τbkg, t, TOPfield, Ecut, data, Nscale, Tscale,
   TOPfieldold, TOPfieldnew,  Tscale2, Vscale2, τscale2, result , τscale, Vscale},



  AtNuminitial = 1. * 10 ^ 9;
  Tinitial = 100. * 10 ^ (-6);
  TOPfieldinitial = topbeginning;
  τbinitial = 132;
  τthinitial = 2;
  τelinitial = τthinitial / 2.7;
```

$$\texttt{colratioinitial =} \frac{\tau\texttt{binitial}}{\tau\texttt{elinitial}}\texttt{;}$$

$$\texttt{PSDinitial =} \frac{\hbar\texttt{\^{}3*(2}\pi\texttt{)\^{}3}}{\left(\sqrt{\texttt{2}\pi\texttt{*87*m}_\texttt{u}\texttt{*k}_\texttt{B}\texttt{*Tinitial}}\right)\texttt{\^{}3}}\texttt{*}\frac{\texttt{AtNuminitial}}{\texttt{Vharm[Tinitial, TOPfieldinitial]}}\texttt{;}$$

```
  ξ = 3 / 2;
  T = temperature;
  AtNum = atomnumber;
```

$$\texttt{PSD =} \frac{\texttt{AtNum / AtNuminitial}}{\texttt{(T / Tinitial) \^{} (}\xi\texttt{ + 3 / 2)}}\texttt{*PSDinitial;}$$

$$\texttt{Tscale =} \frac{\alpha\texttt{harm}\left[\texttt{60*10}^{-4}\right]}{\alpha\texttt{harm[topbeginning]}}\texttt{;}$$

$$\texttt{Vscale =} \sqrt{\frac{\alpha\texttt{harm[topbeginning]}}{\alpha\texttt{harm}\left[\texttt{60*10}^{-4}\right]}}\texttt{;}$$

$$\tau\texttt{scale =} \frac{\texttt{Vscale}}{\sqrt{\texttt{Tscale}}}\texttt{;}$$

$$\tau\texttt{th =} \frac{\texttt{(T / Tinitial) \^{} (}\xi\texttt{ - 0.5)}}{\texttt{AtNum / AtNuminitial}}\texttt{*}\tau\texttt{thinitial*}\tau\texttt{scale;}$$

```
  τel = τth / 2.7;
  τbkg = τbinitial;
```

$$\texttt{colratio =} \frac{\tau\texttt{bkg}}{\tau\texttt{el}}\texttt{;}$$

```
  t = 0;
  η = optimalηintharmonic[colratio] ;
  TOPfield = topbeginning;
```

```
Ecut = kB * T * η + TOPOffset[topbeginning];

data = {{t, AtNum, T, Ecut, colratio, τel, τbkg, PSD, TOPfield}};



If[colratio < 80, data = Join[data, {{0, 0, 0, 0, 0, 0, 0, 0}}],
 While[PSD < 2.614,
   t = t + τbkg / colratio * 2.7;
   η = optimalηintharmonic[colratio];
   Ecut = kB * T * η + TOPOffset[TOPfield];
   Nscale = Nfactor[η, colratio, ξ];
   Tscale = Tfactor[η, colratio, ξ];
   AtNum = Nscale * AtNum;
   T = Tscale * T;
   PSD = PSD * Nscale / (Tscale^(ξ + 3 / 2));
   τel = Tscale^(ξ - 0.5) / Nscale * τel;
   colratio = Nscale / (Tscale^(ξ - 0.5)) * colratio;


   TOPfieldold = TOPfield;
   TOPfieldnew = α / (1 + α) * 1 / (μB * mF * gF) Ecut;

   If[TOPfieldnew > 10 * 10^-4, TOPfield = TOPfieldnew, TOPfield = 10. * 10^-4];

   Tscale2 = (TOPfieldold / TOPfield)^(3/2);
   Vscale2 = Sqrt[(TOPfield / TOPfieldold)^(3/2)];
   τscale2 = Vscale2 / Sqrt[Tscale2];
   T = T * Tscale2;
   τel = τel * τscale2;
   colratio = τbkg / τel;
   data = Join[data, {{t, AtNum, T, Ecut, colratio, τel, τbkg, PSD, TOPfield}}]
  ];
];
result = {{atomnumber, temperature}, data}
];
```

Appendix B

Anisotropic expansion details

B.1 Algorithm

```
omRad = 2 π * 34.2;
omAx = 2 π * 96.4;
initialvector = {1., 1., 0., 0.};
vector = initialvector;
τ = 0;
t = 0;
Δτ = 0.01;
result = {{0, vector}};

While [t < 50 * 10^ (-3),
 τ = τ + Δτ;
 t = τ / omAx;
 $\lambda_{\text{senkrecht}}$ = vector [[1]];
 $\lambda_{\text{ax}}$ = vector [[2]];
 $\lambda_{\text{senkrecht, der}}$ = vector [[3]];
 $\lambda_{\text{ax, der}}$ = vector [[4]];

 $\lambda_{\text{senkrecht, der}}$ = $\lambda_{\text{senkrecht, der}}$ + $\frac{\text{(omRad / omAx) ^2}}{\lambda_{\text{senkrecht}}\ \text{^3} * \lambda_{\text{ax}}}$ * Δτ;
 $\lambda_{\text{senkrecht}}$ = $\lambda_{\text{senkrecht}}$ + $\lambda_{\text{senkrecht, der}}$ * Δτ;
 $\lambda_{\text{ax, der}}$ = $\lambda_{\text{ax, der}}$ + $\frac{1}{\lambda_{\text{senkrecht}}\ \text{^2} * \lambda_{\text{ax}}\ \text{^2}}$ * Δτ;
 $\lambda_{\text{ax}}$ = $\lambda_{\text{ax}}$ + $\lambda_{\text{ax, der}}$ * Δτ;


 vector = {$\lambda_{\text{senkrecht}}$, $\lambda_{\text{ax}}$, $\lambda_{\text{senkrecht, der}}$, $\lambda_{\text{ax, der}}$};

 result = Join [result, {{t, vector}}];
]
```